



EUROPEAN
COMMISSION

Community research

BELBaR

(Contract Number: **295487**)

Progress report of model validation results and model development

DELIVERABLE (D-N°:5.2)

For KAT-KTH

Authors: Ivars Neretnieks , Luis Moreno, Longcheng Liu

For KIT- INE

Authors: Florian Huber, Gopala Darbha, Thorsten Schäfer

For VTT

Authors: Veli-Matti Pulkkanen, Markus Olin

Reporting period: 01/03/12 – 28/02/14

Date of issue of this report: **28/02/14**

Start date of project: **01/03/12**
Months

Duration: 48

BELBaR



DISTRIBUTION LIST

Name	Number of copies	Comments
Christophe Davies (EC) BELBaR Participants		

Project co-funded by the European Commission under the Seventh Euratom Framework Programme for Nuclear Research & Training Activities (2007-2011)

Dissemination Level

PU	Public	X
RE	Restricted to a group specified by the partners of the BELBaR project	
CO	Confidential, only for partners of the BELBaR project	

About this report

This progress report consists of contributions from three organisations.

For KAT-KTH

Ivars Neretnieks, Luis Moreno, Longcheng Liu

Modelling smectite erosion- Development of a two-stage model

Pages 4-60

For KIT- INE

Florian Huber, Gopala Darbha, Thorsten Schäfer

Progress report of model validation and model development

Pages 61-78

For VTT

Veli-Matti Pulkkanen, Markus Olin

Progress report of model validation results and model development.

Pages 79-85

Modelling smectite erosion- Development of a two-stage model

Ivars Neretnieks, Luis Moreno, Longcheng Liu

February 2014

Abstract

Erosion of smectite in a fracture intersecting a deposition hole for spent nuclear fuel with a clay buffer has been modelled with the dynamic clay expansion model using some simplifications compared to the previously used fully coupled model. A two-stage model, which avoids some problems in earlier work was developed and tested. The model divides the region of the expanding clay in the fracture in one where the clay behaves like a Bingham solid/fluid that cannot flow and another the rim region surrounding the former where the gel/sol, although highly viscous in some locations, can flow and carry away the smectite particles that diffuse into this region. Some simplifying assumptions result in a model that is much less complex but gives results that are more accurate in some important regions compared with those obtained earlier by the fully coupled model.

Summary

In our previous modelling of smectite erosion in a fracture intersecting a deposition hole containing a nuclear waste canister the smectite clay was allowed to expand radially by a diffusion like process into a fracture where it encountered seeping water into which the smectite particles diffuse and are carried away. The diffusivity and viscosity of the gel/sol as function of the volume fraction of smectite particles was accounted for as well as the impact of ion concentration in the pore water. The two coupled parabolic partial differential equations were solved using finite element techniques. Sometimes numerical problems were encountered caused by considerable non-linearities in the equations. However, it was found that the diffusion of the ions had a very small impact and that the results practically only depended on the ion concentration in the approaching groundwater. This, the uncertain results, the numerical difficulties and the long computing times led us to develop an alternative way of solving the model equations. To do this the complex interplay between the different intertwined processes was explored. This gave insights that were valuable when developing an alternative method to solve the model equations.

A two-stage model was developed and tested. It divides the gel/sol region in two parts. The gel/sol is modelled as a Bingham solid/fluid. In the inner part the gel has a higher viscosity and does not flow by the shear forces exerted by the water. Nevertheless the gel expands by the internal forces as described by the dynamic gel expansion model developed earlier. At the locus where the gel/sol can just be mobilised the second region commences. In this region the smectite particles diffuse out into the rim zone where the gel/sol flows, first slowly where the viscosity is high but with increasing velocity when the viscosity gradually drops to that of water as the smectite concentration decreases. In the rim zone also the diffusivity changes with the smectite concentration. At the border of the rim zone where flow just starts the smectite concentration is higher than further from the border. The smectite flux in the rim depends on both viscosity and diffusivity, which in turn depend on smectite concentration. They also depend on the ion concentration in the pore water in a complex way.

If one, to begin with, neglects the loss in the rim zone the expansion in the inner zone can be modelled by the instationary diffusion equation in radial coordinates with standard techniques. This gives information on the rate of intrusion of gel into the fracture and thus loss of bentonite from the deposition hole at early times when the length of the rim zone on either side of the hole is small. As the rim zone grows the loss in the rim zone increases while the rate of intrusion of smectite into the fracture decreases. When these rates are equal, steady state is reached, and the loss in the rim matches the intrusion into the fracture. The loss in the thin rim is calculated by solving the equation that describes the smectite diffusion into the rim coupled to the equation that describes how the flow carries these particles downstream. This was also done in the earlier modelling using the finite element method but there numerical difficulties were sometimes encountered because of the strong non-linearities in the rim zone and also the results using this technique overestimate the loss at the rim as well as to underestimate the extent of intrusion into the fracture.

One specific innovation in the present approach is that the two-dimensional space needed to describe the rim zone is transformed to one dimension by neglecting the velocity component perpendicular to the main flow direction. Tests showed that the errors introduced were fairly small. This makes it possible to convert the partial differential equation to an ordinary differential equation formulated as a boundary value problem BVP. Using the shooting

method to solve the BVP extremely rapid changes of gel properties and flowrate in the rim zone can be accurately followed.

The other part of the two-stage model is that describing the expansion of the gel. This was shown to be fairly accurately modelled using a pseudo steady state, PSS, approximation. This avoids the detailed solution of the partial differential equation subject to the boundary condition at the rim. The simple, essentially analytical, PSS based model was used to, in combination with the rim model in a set of examples.

It was found that the loss at the rim was considerably less than the earlier used complex fully coupled modelling showed over a wide range of water velocities and water compositions. Most importantly it was found that at low water flowrates the rate of loss of bentonite from the deposition hole is not governed by the loss at the rim but by the accumulation of smectite in the expanding gel. The expansion and accumulation of smectite in the fracture is practically independent of the water salinity in the range of interest. This implies that a loss of on the order of 1000 kg in 10 000 years can be expected in a 1 mm fracture independent of water flow and water salinity. There is no need for dilute melt water to intrude the repository for the loss to occur and it will start as soon as the repository becomes water saturated.

To ensure that the derived models accurately capture the processes involved numerous and detailed tests of the various mechanisms underlying the two-stage approach were performed. This gave valuable insights into the complex interplay of different processes and of the sensitivity to the parameter values used as input for the modelling.

Table of contents

1	Introduction and background	9
1.1	General.....	9
1.2	Structure of report.....	9
2	Aims and Scope	11
3	Conceptualisation and modelling of a two-stage model	12
3.1	Diffusivity of a gel/sol	12
3.2	Conceptual model.....	12
3.3	Mathematical formulation of the two-stage model.....	14
4	Modelling instationary gel expansion	15
4.1	Instationary expansion	16
4.1.1	Examples with no loss at the rim, only expansion in fracture	16
5	Modelling loss at the rim by an equivalent flowrate	21
5.1	Some comments on the results presented in this chapter.	29
6	Gel/sol viscosity	30
6.1	Introduction.....	30
6.2	Theory and sol viscosity models.....	30
7	Exploration of details in the rim	34
7.1	Mathematical description of the processes in the rim zone.....	34
7.2	Examples using the 2D rim model	36
7.3	Transform of model from 2D to 1D	37
7.4	Examples using the 1D rim model	38
7.5	Comparison with “exact” solution in rim where advection perpendicular to the rim is not neglected.	42
7.6	Comparison with earlier result.....	43
7.7	Some comments on the model and the results presented in this chapter.....	43
8	Analytical approximations of the expansion of the smectite front	45
8.1	Introduction.....	45
8.1.1	The case of constant concentration in the source.....	45
8.1.2	Linear diffusion for PSS	46
8.1.3	Radial diffusion for cylindrical coordinates.....	49
8.2	Including a changing source term concentration $\phi_i(t)$	50
8.3	Some illustrative examples	51
8.3.1	Cylindrical expansion	51
8.4	Some comments on the PSS model	54
9	Discussion	56
9.1	General.....	56
9.2	Implications for long term stability of buffer and impact on solute transport to and from canister	57
10	Conclusions and outlook	58
11	References	59

1 Introduction and background

1.1 General

The bentonite erosion model was developed to estimate the loss of smectite from bentonite used as buffer and backfill in the Swedish KBS-3 repository concept. It was used in SR-Site calculations by SKB and in the modelling of the performance of the Finnish repository at Onkalo. The model is based on the dynamic force balance model and gel/sol viscosity models summarised in Neretnieks et al. (2009) and described in more detail in a number of publications (Liu, 2010, 2011 and 2013, Liu et al. 2009a,b, 2011, Moreno et al. 2010, 2011) The swelling of the smectite in the bentonite clay into the fractures with seeping water and the further transport as gel/sol with the water is influenced by the pore water concentration of primarily mono- and divalent cations. The swelling and erosion can be quantitatively described by a set of equations.

The system of partial differential equations to solve is quite nonlinear and sometimes difficult to solve numerically because of the mutual influence of the evolving chemistry in the gel/sol, the forces acting on the smectite particles and on the viscosity of the gel/sol¹, which determines when and how it can flow. The numerical difficulties and complex interaction between the various mechanisms involved have led us to explore which mechanisms have a dominating impact on the erosion and how simplifications could be made that will lead to more transparent, faster and stable calculations.

It is found that the water chemistry has the largest influence in the outer regions of the gel/sol and that the water composition in the approaching groundwater essentially determines the smectite properties in the region where the gel/sol flows with the water. This allows the chemical transport model to be decoupled from the smectite expansion model, which eliminates the need for continuous coupling of the migration of ions in the expanding gel between the seeping water and interior of bentonite bulk.

It was also found that the flow of the gel/sol occurs in a thin rim where the smectite volume fraction changes from a few percent by volume to essentially smectite free water. This has led us to explore if it is possible to decouple the swelling of the gel/sol in the region where it expands by the swelling forces from the thin rim where the gel/sol both swells and flows.

1.2 Structure of report

After aims and scope the concept of a two-stage model is introduced followed by its mathematical formulation. In the next section the expansion of the stiff gel is described in mathematical terms and an example is presented of the rate of gel intrusion into a fracture. The loss of smectite in the rim zone is presented next, using a very simple model to illustrate how the loss by expansion and the loss in the rim zone can be coupled to obtain the steady state loss of smectite. Examples are used to illustrate how water velocity and ion concentration in the pore water influence the loss of smectite from a deposition hole. Some illustrations of the errors that may be caused by the simplifications are presented. Next, the very simple rim model is extended by accounting for the effects of the strongly variable diffusivity and viscosity in the very narrow rim. The processes in the rim, which are described in two dimensions, the flow direction and the perpendicular diffusion direction, are

¹The term gel/sol is used because in the region of interest in this report there is a gradual transition from gel to sol. When it is clearly a gel or a sol these terms are used.

transformed to one dimension by introducing an approximation, which is shown to give acceptable errors. The results using the two-stage model are compared with those obtained by the fully coupled model. Finally for the two-stage model a solution procedure is presented which essentially is analytical using the pseudo steady state approximation, PSS. It can be used to calculate the rate of loss from the deposition hole over time accounting for the loss at the rim and the mass that accumulates in the facture. The report ends with discussion and conclusions.

2 Aims and Scope

One aim of this study is to gain better insights into the complex and intertwined mechanisms that cause the swelling and erosion of the smectite clay. A further aim is to generate transparent, fast and stable calculation procedures suited for calculations of bentonite loss from a deposition hole. The study addresses smectite clays dominated by monovalent ion chemistry over a wide range of salinity.

3 Conceptualisation and modelling of a two-stage model

3.1 Diffusivity of a gel/sol

Expansion of a smectite gel can be modelled as a diffusion process analogous to diffusion of a solute in water. The concentration of the solute in this case is the concentration of the smectite particles and it is convenient to express it as volume fraction.

Figure 3-1 shows the diffusion coefficient $D(\phi)$ for the smectite particles in water as function of the volume fraction ϕ for different concentrations of monovalent ions for smectite particle diameter 300 nm and thickness 1 nm, (Neretnieks et al. 2009).

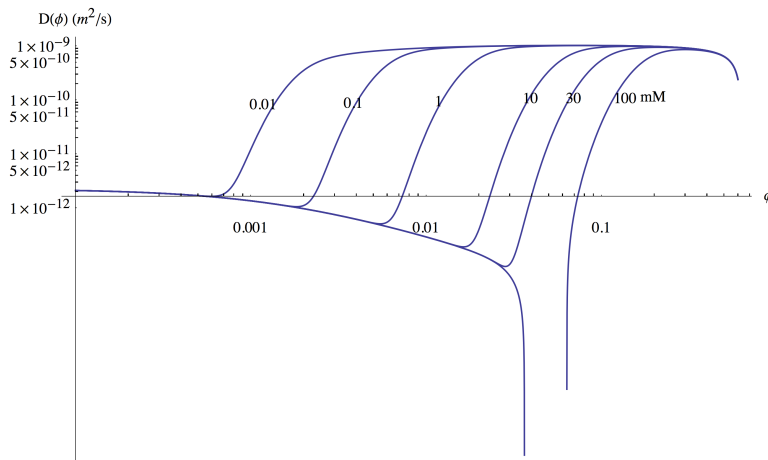


Figure 3-1. Diffusion coefficient $D(\phi)$ for the gel/sol as function of the volume fraction ϕ for different concentrations of monovalent ion, 300 nm particle diameter.

It is seen that for ion concentrations below 1 mM the diffusion coefficient is nearly constant in the volume fraction range $0.02 < \phi < 0.5$ and is about $0.5 \times 10^{-9} \text{ m}^2/\text{s}$. At even lower ion concentrations the volume fraction range is extended to ϕ down to 0.002 or less. Then the diffusion coefficient drops by two to three orders of magnitude. The viscosity of the gel/sol also changes very strongly in the region around $\phi=0.01$.

3.2 Conceptual model

It was found by Moreno et al. (2010 and 2011) that the escape and flow of the smectite takes place in a very narrow region, called the rim, where the smectite volume fraction ϕ very rapidly drops from some value ϕ_R at the rim to zero. Below ϕ_R , roughly in the region $0.01 < \phi < 0.02$, the viscosity of the gel/sol decreases very strongly with decreasing ϕ . The gel/sol velocity where $\phi > \phi_R$ becomes negligible compared to that in the rim and further out. This is supported by the experiments presented in Schatz et al. (2012) where it was found that the gel was rigid and did not deform by the seeping water. When the volume fraction $\phi \ll \phi_R$ the velocity of the water seeping in the fracture is equal to that of the water outside u_o . The rim makes up only a small fraction of the whole region that contains smectite. It seems reasonable to assume that an acceptable error will be introduced if one neglects the

slight increase of the length of the inside and outside borders of the curved rim and other effects caused by the curvature.

In this way the rim around a nearly circular region can be placed at the radius of the circle where $\phi = \phi_R$. An extension to this idea is that as long as the curvature of the rim is small compared to the rim thickness the rim could follow the locus r_R of the gel where $\phi = \phi_R$. See Figures 3-2 and 3-3. Under these conditions the expansion of the gel in the rim is modelled in Cartesian coordinates with ϕ_R located at $y=0$ along the x-axis. The gel expands in the y-direction and flows in the x-direction. Gel that has penetrated some distance y at location x is carried downstream by a velocity that is influenced by the local velocity of the gel/sol. At a location x_o downstream the flowing gel/sol leaves the contact with the gel. The flowrate of smectite particles at this location is N_{rim} .

Consider a fracture that intersects a circular hole of radius r_i filled with smectite where the smectite concentration is ϕ_i from which the gel expands radially outward to a radius r_R where the concentration is ϕ_R , i.e. the same as at the inside of the rim at $y = 0$.

At *steady state* the flowrate of clay that flows downstream at x_o must be the same as that which is transported from the inner radius r_i to the outer radius r_R . The travel length around one side of the outer circle is πr_R . This is the same as x_o . The outward radial rate of transport in the fracture N_{rad} depends on the two radii r_i and r_R . N_{rim} will increase with the radius r_R as the contact area between gel and water increases and N_{rad} will decrease the further away the rim is. Setting the two flowrates equal, the radius and the travel length can be determined by solving for r_R provided r_i is known.

$$2N_{rim}(\pi r_R) = N_{rad}(r_R) \quad (3-1)$$

Figures 3-2 and 3-3 illustrate how the gel expands into the flowing water, which sweeps it downstream. At the distance x_o the flowrate of the smectite in the gel is N_{rim} . In the left part of the figure the concentration ϕ and velocity u as function of y is shown. To the right the product, ϕu which is a measure of the local flux of smectite as function of y , is shown. At $y=0$ the gel has a high concentration giving rise to high viscosity and therefore low gel/sol velocity. Note that at $y=0$ where the smectite volume fraction is ϕ_R the velocity has increased abruptly from zero to u_R , due to the properties of the Bingham fluid/solid. At larger distances y the concentration drops and viscosity becomes lower and the flux can increase. The integral of ϕu over y gives the flowrate of smectite per fracture aperture.

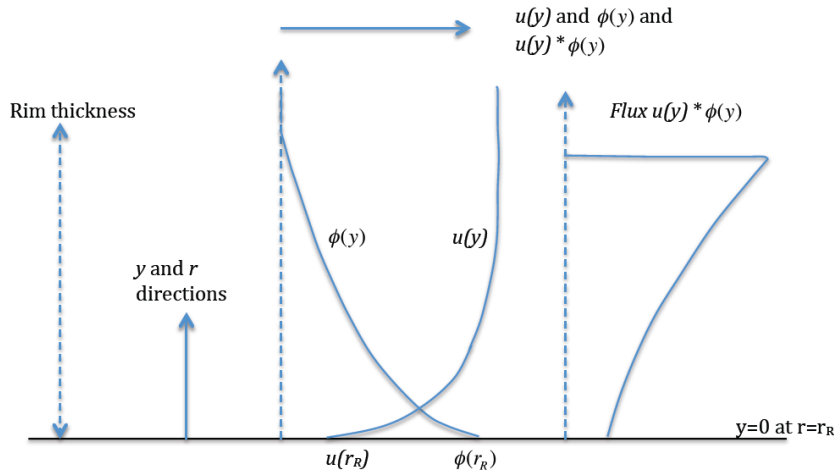


Figure 3-2. Gel expanding in y -direction and flowing in x -direction. Velocity, volume fraction and flux profiles in rim at given x_0 .

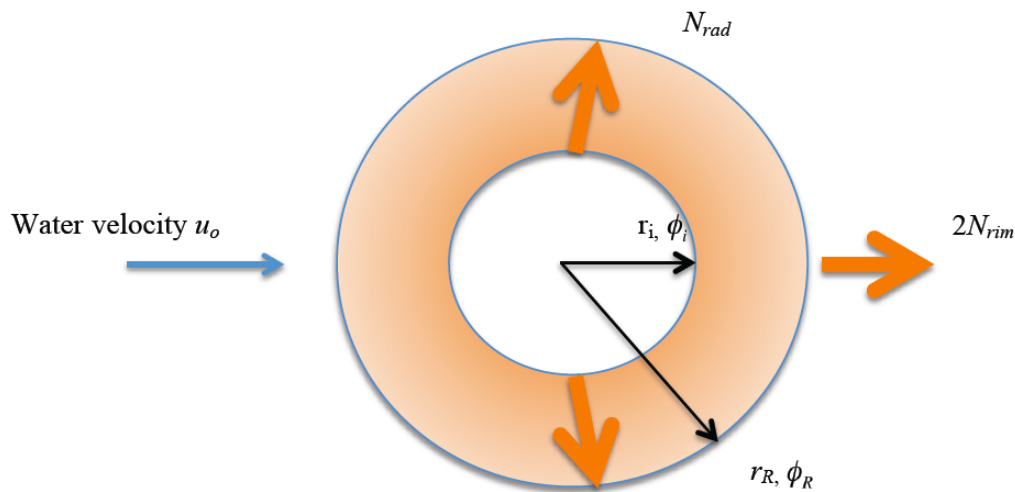


Figure 3-3. Radial expansion of gel in fracture.

It remains to determine how the flowrates N_{rim} and N_{rad} depend on geometry, water velocity, fracture aperture, gel viscosity and gel expansion properties. This will be done in the following sections.

3.3 Mathematical formulation of the two-stage model

In this section a mathematical model for the steady state radial diffusion $N_{rad}(r_R)$ in the fracture is developed. This is then used to determine the distance $x_0 = \pi r_R$ at which $2N_{rim}(\pi r_R) = N_{rad}(r_R)$. The factor 2 enters because the flow is around both sides of the cylindrical hole.

Referring to Figure 3-3 the smectite flowrate in the whole region between the concentric circles for steady state conditions is derived as follows.

$$N_{rad} = -2\pi r \delta_{frac} D(\phi) \frac{d\phi}{dr} \quad (3-2)$$

N_{rad} is the outward expansion rate of smectite at any radius r where the gradient $\frac{d\phi}{dr}$ is known, δ_{frac} is fracture aperture.

This is rearranged to

$$\frac{dr}{r} = -D(\phi) \frac{2\pi\delta_{frac}}{N_{rad}} d\phi \quad (3-3)$$

To find the *steady state* rate of smectite transport in the fracture when the outer radius has stopped expanding this expression can be integrated between r_i and r_R to give

$$\ln\left(\frac{r_R}{r_i}\right) = -\frac{2\pi\delta_{frac}}{N_{rad}} \int_{\phi_i}^{\phi_R} D(\phi) d\phi \quad (3-4)$$

This is rearranged to

$$N_{rad} = -\frac{2\pi\delta_{frac}}{\ln(r_R / r_i)} \int_{\phi_i}^{\phi_R} D(\phi) d\phi \quad (3-5)$$

When D is constant

$$N_{rad} = -\frac{2\pi\delta_{frac}}{\ln(r_R / r_i)} D(\phi_R - \phi_i) \quad (3-6)$$

Equation (3-5) or (3-6) give the desired expression for $N_{rad}(r_R)$

The concentration profile in the fracture when D is constant is

$$\phi(r) = \phi_i + \frac{\ln(r / r_i)}{\ln(r_R / r_i)} (\phi_R - \phi_i) \quad (3-7)$$

The mass of smectite residing in the fracture M_{frac} at a given outer radius for constant diffusion coefficient is obtained by integration of the profile, it is

$$M_{frac} = \delta_{frac} \rho_{smec} 2\pi \int_{r_i}^{r_R} \phi(r) r dr \quad (3-8)$$

At steady state the rate of loss by the flow in the rim is equal to the rate at which the expanding gel reaches the rim.

$$2N_{rim}(\pi r_R) = N_{rad}(r_R) \quad (3-9)$$

4 Modelling instationary gel expansion

4.1 Instationary expansion

Moreno et al. (2010) formulated and solved fully coupled equations for the instationary case when the water flows around the hole with swelling smectite clay and the smectite expands out into the fracture. In the entire region the gel/sol movement is accounted for simultaneously. With the assumption in the present report the influence of the curvature of the rim can be neglected and the gel is immobile at $\phi > \phi_R$.

At low water velocity, which implies low erosion rates, the instationary phase of gel penetration into the fracture is of considerable interest as large amounts of smectite can be lost from the deposition hole long before stationary conditions are established. Below we explore the rate and mass of loss during the instationary period.

When the loss at the rim is so small during the early expansion period that the rate of feeding the fracture is much larger, i.e. before stationary conditions are reached one can neglect the loss at the rim. Then the equations can be considerably simplified as there is then no need to account for the loss and the outer boundary can be set at a very large distance where $\phi=0$.

Solving the radial diffusion equation is then considerably simplified. We later also include the impact of the loss at the rim on the rate of expansion of the gel. However, the simpler approach gives some valuable insights and helps understanding the conditions during early times.

For these conditions the instationary diffusion for cylindrical radial diffusion is

$$\frac{\partial \phi}{\partial t} = \frac{1}{r} \frac{\partial}{\partial r} (rD(\phi) \frac{\partial \phi}{\partial r}) \quad (4-1)$$

The inner boundary conditions is

$$\text{BC1: } \phi(r_i, t) = \phi_{ri} \quad (4-2)$$

The outer boundary condition

$$\text{BC2: } \phi(r \rightarrow \infty, t) = 0 \quad (4-3)$$

The initial condition is

$$\text{IC: } \phi(r > r_i, 0) = 0 \quad (4-4)$$

Analytical solutions to (4-1) with these initial and boundary conditions are known when D is constant and when the concentration ϕ_i is constant at r_i , (Carslaw and Jaeger 1959). The equations can also be solved with very high accuracy using numerical techniques.

When D depends on ϕ numerical techniques must be used. However, when D changes very rapidly in one or more locations as is the case for smectite, the demand on commonly used numerical methods increases considerably and if the change in D is very large and rapid, computation times and errors tend to grow, or the methods may even fail entirely. Care must be used to ensure that errors are recognised and possibly quantified. The modelling is further complicated when the loss of smectite into the seeping water must be accounted for.

4.1.1 Examples with no loss at the rim, only expansion in fracture

In the first example the chemical conditions are chosen such that the smectite diffusion coefficient is essentially constant down to very low volume fractions. This would be the case for monovalent ions and very low ionic strengths such as are expected for glacial meltwater. Table 4.1 shows the data used.

Table 4.1. Data used in examples.

Parameter	Value	Comment
r_i	0.875 m	Radius of deposition hole
ϕ_i	0.5	Volume fraction at r_i
ϕ_R	0.01	Volume fraction at rim r_R , value used for illustration
$D(\phi)$	$10^{-9} \text{ m}^2/\text{s}$	Diffusion coefficient for smectite gel for all $\phi > \phi_R$
$D(\phi_R)$	$10^{-9} \text{ m}^2/\text{s}$ $10^{-11} \text{ m}^2/\text{s}$	Diffusion coefficient for smectite sol in rim, $r > r_R$, values used for illustration
δ_{frac}	1 mm	Fracture aperture

Example 4.1. Constant smectite diffusion coefficient in gel/sol

First we present a case with a constant diffusion coefficient because there is an analytical solution available (Carslaw and Jaeger 1959, p 335 Eq. (6)), which can be used to check the numerical solution, which was obtained by the method of lines.

Figure 4-1 shows a comparison of the numerical solution with the analytical solution for a case with a monovalent cation with concentration 1 mol/m^3 . The agreement is excellent down to very low volume fractions.

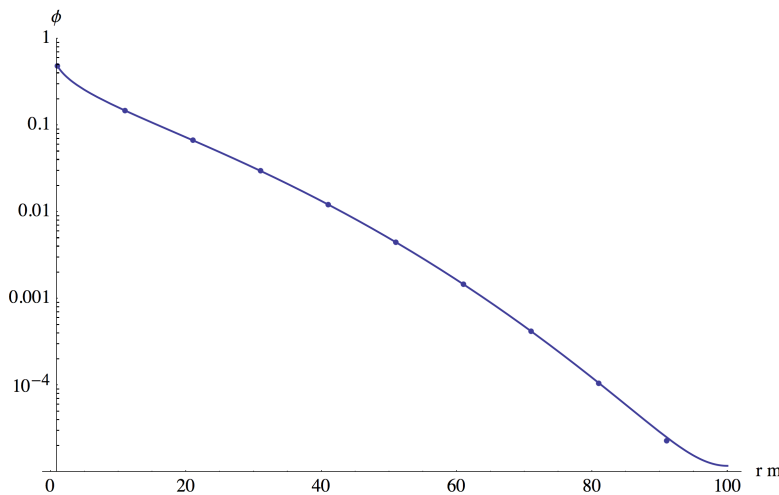


Figure 4-1. Comparison of numeric and analytical solution (points). Constant diffusion coefficient $10^{-9} \text{ m}^2/\text{s}$. $t=10\,000$ years.

The numerical results obtained by “Method of lines” in Mathematica[®] are practically indistinguishable from those obtained using the analytical solution (Carslaw and Jaeger 1959).

Figure 4-2 illustrates the location of the locus of a volume fraction exemplified by $\phi_R = 0.01$ at the rim at different times. In the two-stage model ϕ_R is chosen such that above this value

the gel is taken to be immobile due its very high viscosity. This will be discussed in a later section but the value in the example is quite realistic.

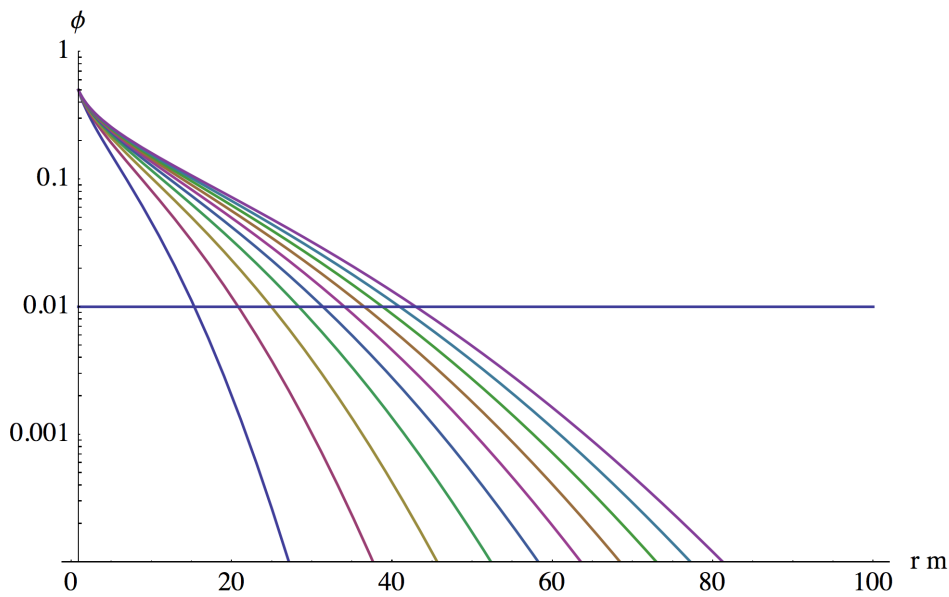


Figure 4-2. Smectite concentration profile in fracture for constant diffusion coefficient at times 1000 (1000) to 10 000 years. Horizontal solid line shows $\phi_R = 0.01$. Constant diffusion coefficient $10^{-9} \text{ m}^2/\text{s}$.

There will be loss of smectite from the deposition hole even if none is carried away at the rim because of the amount that resides in the fracture at any given time.

Figure 4-3 shows the rate of intrusion of smectite into the fracture over time.

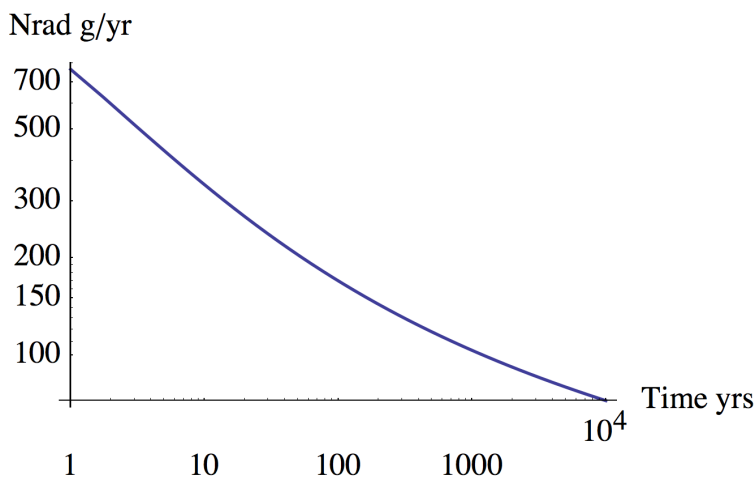


Figure 4-3. Rate of intrusion of smectite into the fracture over time. Constant diffusion coefficient $10^{-9} \text{ m}^2/\text{s}$. Fracture aperture 1mm.

One of the tests used to see that the numerical results are reasonable is to compare the mass of smectite that resides in the fracture by integrating the volume fraction in it, Equation (3-7), with the mass obtained by integrating over time how much smectite entered the fracture

Equation (3-5). The difference was less than 3 % with standard settings of the space discretisation in the numerical code. It could be improved with higher discretisation. This test turned out to be quite sensitive for cases when the smectite diffusion coefficient varied strongly in later examples. Sometimes the results could seem reasonable in other respects but could differ very much in this test and must be discarded.

Figure 4-4 shows the mass M_{rad} of smectite in the fracture increasing with time. It could be fitted well by a simple equation

$$M_{rad} = 2358\sqrt{t} + 63.0 t \quad (4-5)$$

M_{rad} is in g and t is in years

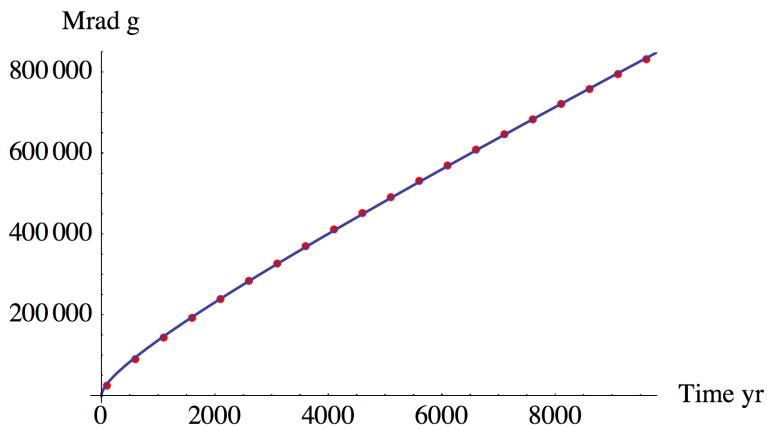


Figure 4-4. Mass of smectite in the fracture as function of time. Constant diffusion coefficient $10^{-9} \text{ m}^2/\text{s}$ and fracture aperture 1mm.

Figure 4-5 shows how the radius to the rim r_R ($\phi_R = 0.01$), increases with time.

This could also be fitted to a simple equation

$$r_R = 1.48 + 0.446\sqrt{t} - 0.00032 t \quad (4-6)$$

It may be noted that, as expected, the \sqrt{t} term much dominates in the equation.

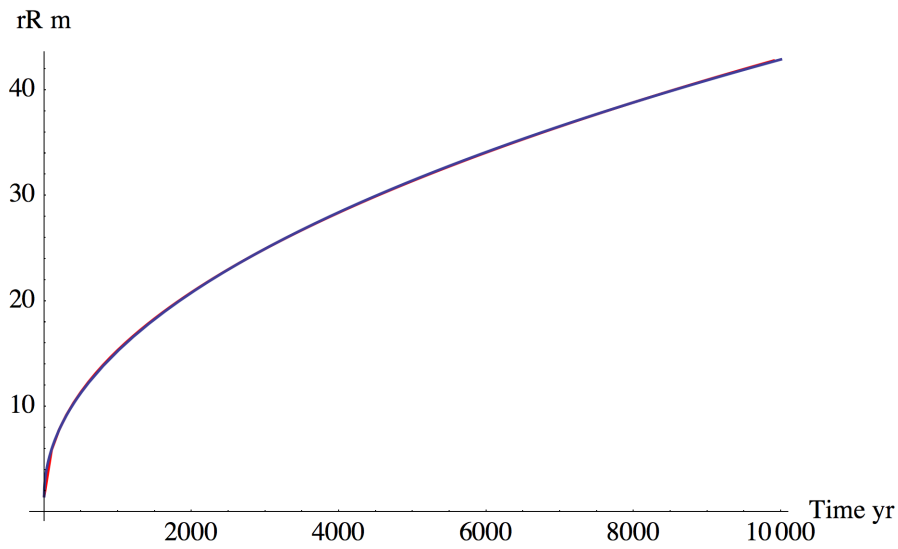


Figure 4-5. Radius to the rim for $r_R(\phi_R = 0.01)$ as function of time. Constant diffusion coefficient $10^{-9} \text{ m}^2/\text{s}$. Fracture aperture 1 mm.

The above results suggest that considerable amount of smectite can be lost from the deposition hole just by the intrusion of clay into the fracture without any additional loss to seeping water for a fracture aperture of 1 mm. It will later be shown that for such intrusion into a fracture there is no need for dilute water to be present.

5 Modelling loss at the rim by an equivalent flowrate

In section 4 the expansion of the gel/sol into the fracture when there was no loss at the rim was described. When there is loss at the rim where the smectite volume fraction is ϕ_R this will increase the rate of intrusion into the fracture from the hole because this loss must be accounted for when solving the equation. In this section the impact on the expansion by loss at the rim is explored in order to gain some insight into how sensitive the rate of intrusion and the loss at the rim are to water velocity and ion concentration. This is done using simplifying assumptions that avoid some of the complexities of the intertwined processes. More detailed analyses are presented in sections 6 and 7.

The flowrate of smectite at a given flow distance x can be determined by integrating the product of velocity and smectite concentration from the border of the rim $y=0$ to infinity. See the right-most profile in Figure 3-2.

$$N = \delta_{frac} \int_0^{\infty} u(y)\phi(y)dy = \delta_{frac}u_o \int_0^{\infty} \frac{\phi(y)}{\eta_{rel}(\phi(y))} dy \quad (5-1)$$

Assuming that the local velocity is inversely proportional to the local viscosity the right-most term in Equation (5-1) is obtained. $\eta_{rel} = \eta_{\phi}/\eta_w$, η_w is the viscosity of the water without smectite, η_{ϕ} the viscosity of the gel/sol with smectite volume fraction ϕ and u_o is the water velocity of the approaching water.

Equation (5-1) has previously been used to describe cases where a diffusing solute does not influence the viscosity of the fluid, Neretnieks et al. (2010). A very simple solution is then obtained.

$$N = \frac{2}{\sqrt{\pi}} \delta_{frac} \phi_R \sqrt{D_w u_o x_o} = 2\delta_{frac} \phi_R \sqrt{D_w u_o r_R} \quad (5-2)$$

D_w is the diffusion coefficient of the solute in water. The right-most term is obtained by substituting $x_o = \pi r_R$. The loss when water flows around the “up- side” and the “down- side” of the cylinder in Figure 3-2 will be $2N$. Introduce now the concept of the equivalent flowrate Q_{eq} , which is the flowrate that carries a concentration equal to that at the border of the rim ϕ_R for $\eta_{rel} = 1$.

$$N_{Q_{eq}} = \phi_R Q_{eq} = \phi_R 4\delta_{frac} \sqrt{D_w u_o r_R} \quad (5-3)$$

The above equations were obtained for linear flow conditions. The exact solution for flow around a cylinder accounting also for the curvature of the flow field changes the constant from 4 to 4.51, Chambré et al. (1982).

It can be expected from equation (5-3) that Q_{eq} will increase the larger the circumference of the rim is because contact area with the gel at the rim is larger. Q_{eq} will depend in a complex manner on the diffusion and flow velocity distribution in the rim zone.

The integral $\int_0^{\infty} \frac{\phi(y)}{\eta_{rel}(\phi(y))} dy$ in Equation (5-1) will depend on how the smectite concentration and relative viscosity which in turn depends on the smectite concentration change in the rim zone. In the present section we assume that it can be expected that (shown later in section 7) Q_{eq} will depend on velocity and radius in the same way as it does for a solute that does not influence the viscosity. The constant $k_{Q_{eq}}$ (4 or 4.51) will be different and depend on what values are chosen for the velocity and diffusivity. One possible choice would be to chose the values at the border of the rim, u_R and $D(\phi_R)$ respectively. Other choices are also possible.

$$Q_{eq} = k_{Q_{eq}} \delta_{frac} \sqrt{D(\phi_R) r_R} u_R \quad (5-4)$$

$D(\phi_R)$ is the diffusion coefficient in water of the smectite particles at the rim border and u_R the water velocity at the rim border where the higher viscosity of the gel/sol has slowed down the undisturbed water velocity. Depending on the ionic strength of the water $D(\phi_R)$ can range from 10^{-12} to 10^{-9} m²/s, the lower value applies for higher ionic strengths. The viscosity at the rim can rise by an order of magnitude or more above that of water at the rim border. The proportionality constant k_{Qeq} will depend on the conditions in the rim zone.

It will be explored in section 7 if Equation (5-4) with appropriate choice of diffusivity and velocity could be used to make, at least, first estimates of Q_{eq} without having to solve the coupled PDE flow and diffusion equations needed to integrate $\int_0^\infty \frac{\phi(y)}{\eta_{rel}(\phi(y))} dy$ in Equation (5-1).

The present section is therefore used to illustrate the very simple concept of the two-stage model before embarking on the more complex analysis of the details in the rim zone.

The radius of the rim r_R , grows with time and the intrusion rate into the fracture decreases with time. We would wish to solve the expansion Equation (4-1) with the boundary condition that as r_R is changing with time the loss of smectite at the rim is equal to the uptake by the water. This can be expressed as

$$N_{rad}(r_R) = -(D(\phi_R) \times \frac{\partial \phi}{\partial r})_{r_R} \times 2\pi r_R \delta_{frac} = Q_{eq}(r_R) \times \phi_R \quad (5-5)$$

This condition is not easily used in conjunction with Equation (4-1) because the location of r_R is changing with time as is the gradient $\frac{\partial \phi}{\partial r}$.

Instead the method outlined in Section 3.2 is used to find r_R , the radius at which the concentration is ϕ_R and the rate at which smectite intrudes the fracture $N_{rad}(r_i)$ as a function of the radius r_R . $N_{rad}(r_i)$ is thus the rate of loss of smectite from the deposition hole if there were no loss by Q_{eq} at the rim. This is the smallest loss possible. Should there be any smectite carried away by the seeping water, r_R would not advance as rapidly; the gradient would be steeper and the intrusion into the fracture would be more rapid. Thus the rate of loss from the deposition hole would be larger. At some distance r_R steady state is reached when the rate of intrusion just balances the rate of loss by Q_{eq} . Solving Equation (3-1) for this distance also gives an estimate of the time for this to take place. At early times the loss is governed by the expanding smectite in the fracture, at longer times r_R has stopped moving and steady state loss results.

Example 5.1. Low ionic strength.

In this case the ion concentration is taken to be so low that the diffusion coefficient is the same over the whole range of smectite volume fraction. This means that at the edge of the rim from which the particles diffuse into the seeping water is rapid compared to what it would be at higher ion concentrations where the diffusion coefficient has dropped by 2-3 orders of magnitude. The data in Example 4.1 are used. Figure 5-1 shows the rate of intrusion of smectite into the fracture, N_{rad} , on the one hand (without any loss at the rim) and the loss at the rim by the equivalent flowrate N_{Qeq} on the other hand as function of time. $N_{Qeq}(t)$ as function of time is obtained from $N_{Qeq}(r)$ using the relation $r_R(t)$, Equation (4-6). $N_{Qeq}(t)$ is plotted for four different water velocities.

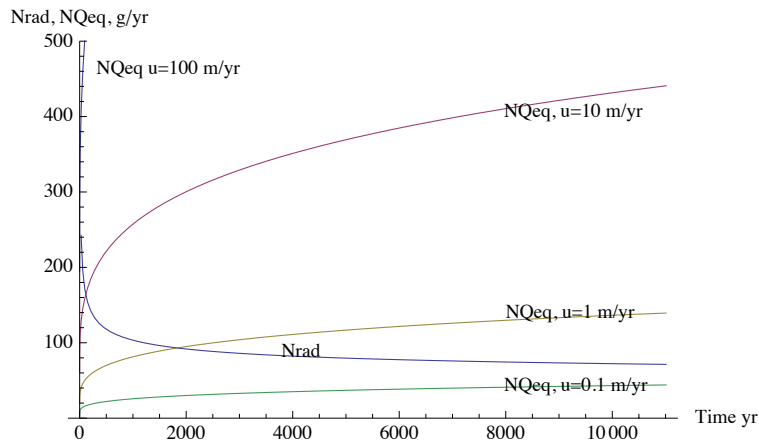


Figure 5-1. N_{rad} and N_{Qeq} vs. time for different water velocities. Constant diffusion coefficient $10^{-9} \text{ m}^2/\text{s}$. Fracture aperture 1 mm .

Considering the case for $u=1 \text{ m/year}$ the figure shows that at early times, less than, about 1000 years, the loss of smectite is governed by N_{rad} . The loss at the rim, N_{Qeq} , is so small that that the concentration profile is only little influenced by it. At around 2000 years this is no longer true and the use of N_{rad} obtained from Equation (4-1) is no longer correct. At longer times the intrusion into the fracture stabilises at a rate that just compensates the loss at the rim and r_R becomes stationary. The described approach gives no exact information about at which distance this occurs, or at what time the front has essentially stabilised because the approach is asymptotic. Nevertheless it may be informative to explore at about what time the stabilisation could be approached and what rate of loss one thereafter could expect. This is shown in Figure 5-2 in which N_{rad} is plotted up to the time of intersection with N_{Qeq} after which the latter takes over from the now stationary r_R . The line for the lowest water velocity does not intersect the N_{rad} curve in 10 000 years and is not shown in the figure.

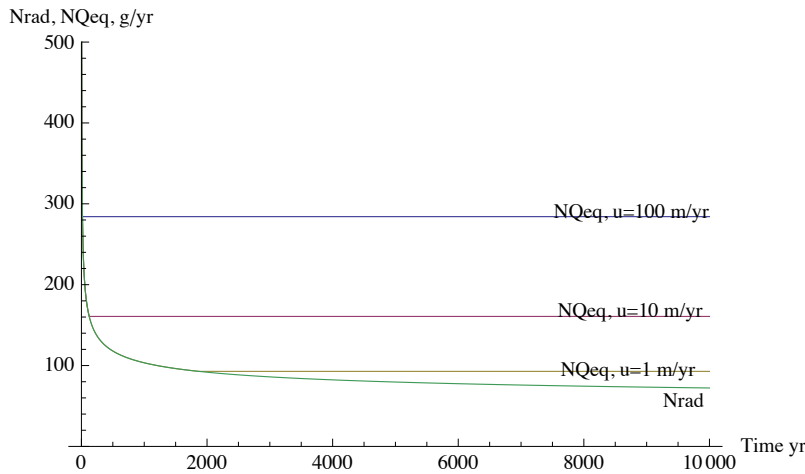


Figure 5-2. N_{rad} and N_{Qeq} vs. time for different water velocities. Before and after (horizontal lines) the distance to the rim has stabilised. Constant diffusion coefficient $10^{-9} \text{ m}^2/\text{s}$. Fracture aperture of 1mm.

Figure 5-3 shows the rate of loss after 10 000 years as function of water velocity in a double logarithmic plot. A fit to the plot is given by Equation (5-6).

$$N = 94 \times u^{0.24} \quad (5-6)$$

N is in g/yr and u in m/yr.

A tenfold increase in velocity would give an increase of erosion by about a factor of 1.7

It is seen in Figures 5-1 and 5-2 that at earlier times this would also be a fair approximation for the higher velocities but not for the lowest, 0.1 m/year where the loss at the rim N_{Qeq} has not yet started to influence the process.

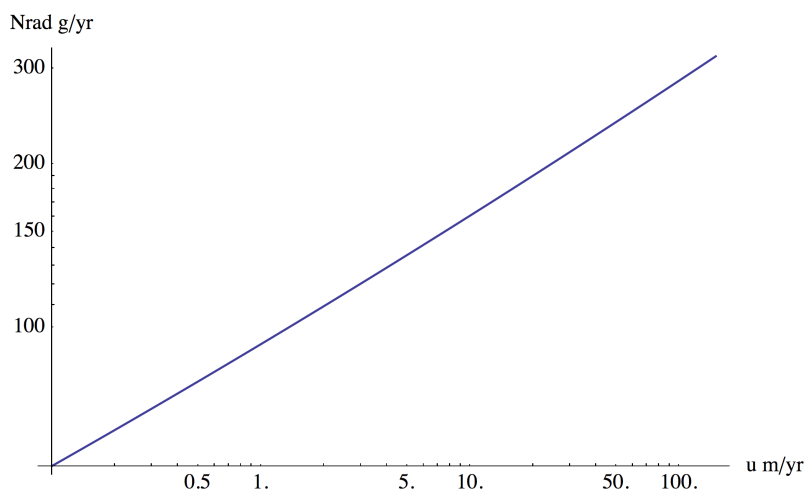


Figure 5-3. Rate of loss after 10 000 years as function of water velocity.

The region of cross over from one mechanism to the other is not captured by the above approach. When the loss at the rim starts to influence the expansion the solution of Equation (4-1) underlying N_{rad} is no longer valid. The smectite concentration profile is influenced by

the loss at r_R in a way that is not given by the two-stage model. One would expect that if the concentration ϕ_R is small and the location of the rim is far from the deposition hole the concentration profile should not be much influenced and the error would be small.

A simple exploration of the error introduced by the above procedure can be made by comparing the rate of loss obtained from N_{rad} for the instationary expansion (section 4.1) with that determined from the solution for the steady state profile, Equations (3-6) and (3-5).

Figure 5-4 shows the instationary and the steady state concentration profiles for the four water velocities u , 100, 10, 1 and 0.1 m/yr, The impact on the rate of loss is directly proportional to the slope of the profile at $r=r_i$. The differences decrease with decreasing velocity as the ratio r_R/r_i grows.

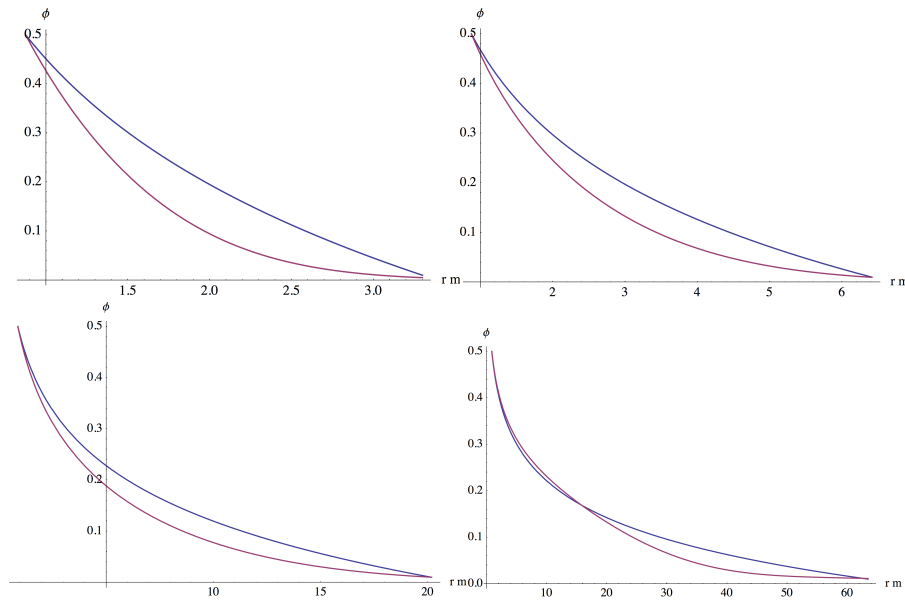


Figure 5-4. Comparison between instationary (lower, red) and steady state (upper, blue) concentration profiles for four different water velocities. Constant diffusion coefficient $10^{-9} \text{ m}^2/\text{s}$. Water velocities u , 100, 10, upper two figures from left, 1 and 0.1 m/yr, lower two figures from left.

Table 5-1 shows the comparison between the loss calculated by the expansion into the fracture without accounting for the loss to the rim as described in section 4.1 and the steady state loss. The differences are not very large. We remind the reader that Equation 5-4 has been used to calculate the rim loss based on the data in Table 4.1. With these data Equation (5-4) may not give realistic values of loss or radius and the example serves only to demonstrate that if $\phi_R \ll \phi_i$ the errors might be acceptable.

Table 5.1. Comparison between the instationary and steady state loss of smectite for four different water velocities.

Water velocity m/year	N_{ss} g/year Eq 3-6	N_{rad} g/year No loss at rim at time for SS, Eqs 4.1-4	Radius to rim at SS m Eq 3-1	Approximate time to reach SS, years, Eqs 4.1-4 and 3-1
100	284	190	3.5	25
10	161	127	6.6	140
1	93	80	21	2200
0.1	55	59	65	>10 000

It is seen in Table 5.1 that there are differences in the SS release rates if one uses the steady state profile or the profile obtained from the instationary solution of the diffusion equation. The differences are not excessively large and the results suggest that even the very simple SS expression could be used for first estimates and exploratory calculations. In chapter 7 a more accurate approach to estimate the loss in the rim is derived than that given by Equation (5-3).

Example 5.2. High ion concentration

In this case the diffusion coefficient down to ϕ_R is constant but is 100 times smaller for $\phi < \phi_R$. This case illustrates when the ionic strength is so high that at the rim where the gel just becomes less viscous and can flow the smectite particle diffusivity has dropped by a factor of 100. This occurs at larger ionic strength in excess of around 1 mM, see Figure 3-1. The uptake for a given r_R into the passing water will be slower by a factor of 10, the square root of 100, according to Equation (5-2). The gel therefore expands further out before the circumference becomes large enough for the water to carry it away in appreciable amounts.

As expected, the loss is dominated by expansion into the fracture and the impact of erosion at the rim is practically negligible except at the highest water velocities. This is shown in Figure 5-5 where no N_{Qeq} curves with $u < 10$ m/yr intersect the N_{rad} curve (lowest slightly curved) in 10 000 years.

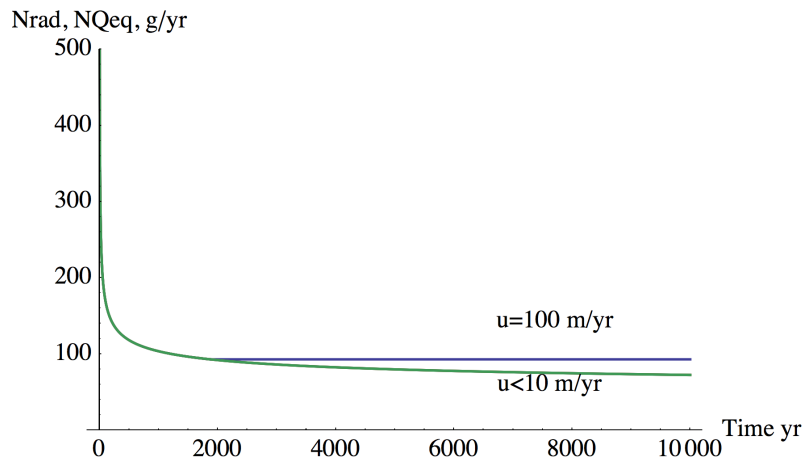


Figure 5-5. N_{rad} and N_{Qeq} vs. time for different water velocities. Before and after the distance to the rim has stabilised. Constant diffusion coefficient $10^{-9} \text{ m}^2/\text{s}$ for the expanding gel but $10^{-11} \text{ m}^2/\text{s}$ at the border of the rim. Fracture aperture 1mm.

As expected the rate of loss from the deposition hole becomes increasingly dominated by the accumulation in the fracture and the loss at the rim becomes less important during times up to the 10 000 years in the example. It may be noted that steady state conditions are only reached at for highest water velocity 100 m/yr within this time period. For 10 m/yr it would take around 50 000 years to reach steady state. This is because the diffusivity at the border of the rim is low which causes the loss by to the seeping water to be ten times lower than in example 5.1. It may further be noted that the time to reach steady state and the radius at which this occurs is very sensitive to the loss in the rim as the N_{rad} and N_{Qeq} curves become increasing parallel.

Example 5.3. Variable smectite diffusion coefficient in gel/sol

In two preceding examples the smectite concentration profile in the expanding gel was based on the solution of the diffusion equation with the outer boundary where the concentration drops to zero taken to be at infinity and that there was no loss at the rim. This introduces some error because at the loss at the rim will cause the profile to be modified somewhat during the instationary phase. It was found by comparison with the profile at steady state, which gives the correct profile that the errors were not very large. However, the profiles were derived using a constant diffusion coefficient for the instationary calculations. In this example the concentration profile in the expanding gel is solved accounting for the variable diffusion coefficient, assuming as before that the boundary condition does not account for the loss in the rim.

Figure 5-6 shows the concentration profile at 10 000 years for a case where the monovalent ion concentration $c = 1 \text{ mM}$ and where the diffusion coefficient depends on volume fraction as in the dynamic force balance model, Liu et al. (2009a). See Figure 3-1.

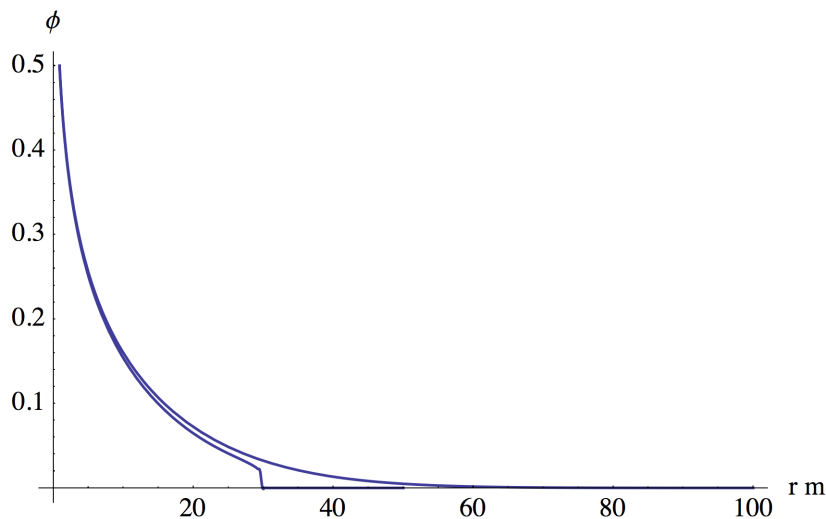


Figure 5-6. concentration profile at 10 000 years for a case where the monovalent ion concentration $c = 1 \text{ mM}$ for constant D and for $D(\phi)$.

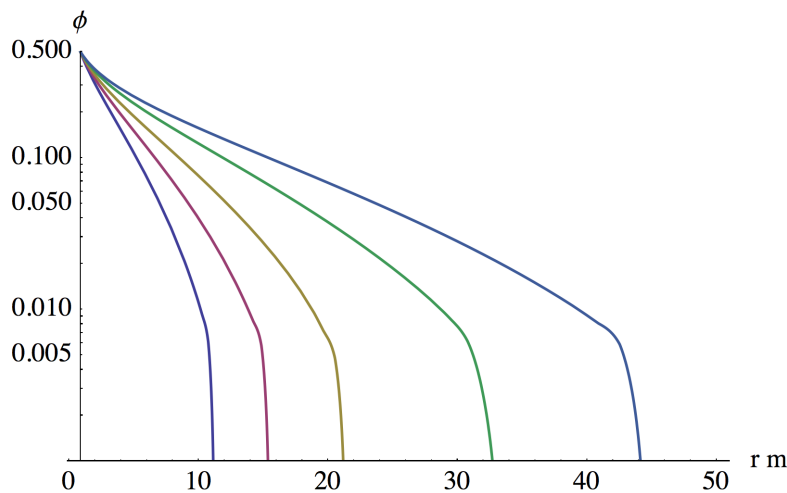


Figure 5-7. concentration profile in a logarithmic scale for times 500, 1000, 2000, 5000 and 10 000 years.

Figures 5-6 and 5-7 show that at around $\phi = 0.008$ the volume fraction starts to drop very sharply. This is expected because the expanding smectite compresses that with a lower diffusivity, which cannot diffuse away as the gel expands. The “method of lines” in Mathematica[®] was used with “MaxStepFraction”=1/500 to generate the curves for the nonlinear case.

The sharp drop in the concentration profile starts at ϕ around 0.008, which is about the same value as where the gel/sol does not flow as will be shown in a later section. This implies that the concentration profile would deviate less from the correct profile than in the constant diffusion coefficient case.

From the above examples it may be concluded that when the drop in D occurs at $\phi < \phi_R$, i.e. at low c 's where D is still large the *loss at the rim* can be expected to be as illustrated in Example 5.1. When on the other hand the drop in D occurs at $\phi > \phi_R$ the loss will be smaller as shown in example 5-2. However, the loss due to *intrusion into and accumulation in the*

fracture may not differ much over the longer times because most of the intruded smectite remains in the fracture. This is shown in Figure 5-8 where the mass of smectite in the fracture at different times is presented for the case of low and high D at $\phi < \phi_R$ from previous examples.

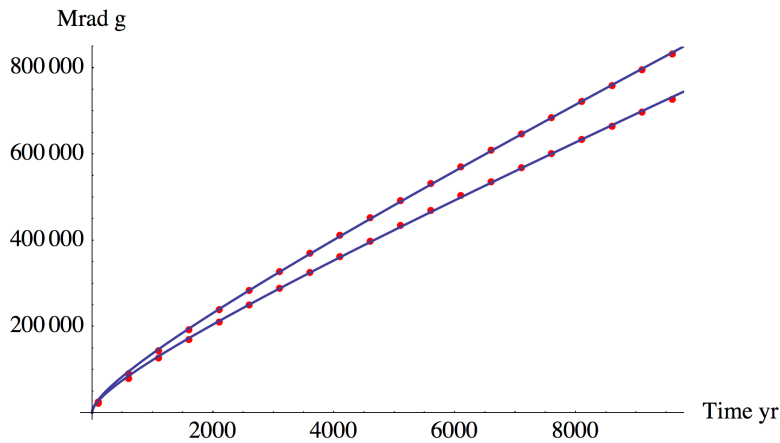


Figure 5-8. Mass of smectite in the fracture at different times for the case of low and high D , at $\phi < \phi_R$, upper curve, from examples 5.1 and 5.2. Dots are from the solution and lines are fitted curves.

5.1 Some comments on the results presented in this chapter.

It was also found that the error in using the steady state solution of concentration profile as a proxy for the instationary is on the order of a factor 2 during the instationary phase and decreases to zero at steady state. It was also seen that the sharp drop in diffusion coefficient at low volume fractions only slightly slows down the expansion of the gel into the fracture. The omission the effect of this drop gives a small error in the rate of intrusion of the gel into the fracture.

6 Gel/sol viscosity

6.1 Introduction

The underlying assumption for the simple Q_{eq} model, Equation (5-3), is that u and D are constant. This is not the case when there are smectite particles in the water. The gel/sol viscosity increases with increasing ϕ . It also changes with ion concentration and particle dimensions as does D . Very dilute sols will have a viscosity that approaches that of water. With increasing volume fraction of smectite the viscosity increases and at higher volume fractions the gel viscosity becomes increasingly more non-Newtonian. This means that the shear force is no longer proportional to shear rate. In a narrow region of volume fractions the gel starts to behave like a Bingham fluid/body. This means that a minimum shear force is needed to make the gel flow. However, an expanding gel will expand unimpeded by the gel viscosity because in the expansion there is no *net flow of gel*. The smectite particles that move are replaced by the same volume of water and there is thus no net movement of the smectite-water mixture making up the gel.

If the shear force is less than that needed to mobilise the gel a sharp front will develop between the expanding gel and the seeping water. The smectite particles at the front can be released from the front by the repulsive double layer forces and diffuse out into the water. Then they can be carried away by seeping water as described in earlier sections. In this section we explore how the gel/sol viscosity depends on volume fraction and chemical composition of water to find a way to determine the volume fraction ϕ_R at which the gel/sol suddenly becomes immobile.

6.2 Theory and sol viscosity models

Here only a brief summary of the theory is presented. More details and specific data on smectite suspensions can be found in (Liu 2011 and Neretnieks et al. 2009). The viscosity of a fluid with dilute suspended spherical particles will increase in viscosity as

$$\eta = \eta_w \left(1 + \frac{5}{2} \phi\right) \quad (6-1)$$

η is the viscosity of the suspension, η_w that of the water. Smectite particles can be described as coin-like thin sheets and the notion of co-volume is used to obtain the impact of such particles on the viscosity. The underlying idea is that the coin-like particles jitter and can rotate due to the impact of water molecules that move randomly caused by thermal forces in the fluid. The particles can come in contact with each other more frequently than if the solid particle volume were concentrated in a small sphere. The volume of a sphere in which the coin can rotate is called the co-volume. The co-volume fraction ϕ_{cov} is used in equation (6-1) instead but the constant, which is 2.5 for solid spheres, must be determined by experiments. For the charged smectite particles, which develop a diffuse double layer of a cloud of surrounding cations this also must be taken into account. The extent of the diffuse layer increases with decreasing ionic strength in the water. One can visualize that a large diffuse double layer at the edges of the coin-like particle also will influence the co-volume. Some measure of the “size” of the double layer could then be added to the radius of the coin to account for this.

In a suspension where the co-volume is larger than one the particles will not be able to rotate unimpeded by its neighbours. In gel with $\phi_{cov} \gg 1$ the coin-like particles must be aligned in parallel in stacks with narrow distances. Such a gel will strongly resist deformation because the stacks must be deformed when the sheets slide in relation to other sheets in a stack and the

deforming stacks will stress and strain the neighbours. It is envisaged that the rheological properties of a gel with ϕ_{cov} fraction around one can become strongly nonlinear.

Liu's model (2011) is based on available experimental data. However, the largest experimental volume fraction is 0.009 and the largest co-volume fraction is about 1.6. The largest increase in the viscosity is nearly 10 for this value. The viscosity model is

$$\eta_{rel} = \frac{\eta}{\eta_w} = 1 + 1.022\phi_{cov} + 1.358(\phi_{cov})^3 \quad (6-2)$$

η is the gel viscosity, η_w that of water and η_{rel} is the relative viscosity.

ϕ_{cov} depends on the particle dimensions, the charge of the cations and their concentration. These relations are not shown here. For details see Liu (2011) or Neretnieks et al. (2009).

A number of rheological experiments are reported in Birgersson et al. (2009). They found that for the natural bentonite MX-80 and for homoionic Na-smectite, WyNa, the viscosity of the gel/sol starts to deviate from Newtonian at volume fractions ϕ between 0.005 and 0.007 for both materials in distilled water. For increasing salinity, up to 100 mM NaCl the volume fraction at which the Newtonian behaviour becomes noticeable is larger but still below about 0.01. Very strong non-Newtonian behaviour is found when $\phi > 0.01$ in both distilled water and saline waters but is most prominent at salinities below 5 mM. In the region $0.005 < \phi < 0.007$ for MX-80 the shear stress increases rapidly with shear rates of around 1/s and at larger shear rates level off to approach a linear behaviour with a viscosity not very different from the dilute suspension predicted by Equation (6-2). This is typical of a Bingham fluid.

Extrapolating the Newtonian part to zero shear rate suggests that a minimum shear stress of about 0.1 N/m^2 is needed to set the gel moving. The shear stress in a fracture is about 0.001 N/m^2 for a fracture with an aperture of 0.2 mm subject to a hydraulic gradient of 0.001 m/m. Such shear stress would not mobilise the gel. The velocity in such a smooth slit would be on the order of 10^5 m/yr . Bird et al. (2002 p 63). This is very much larger than expected velocities around deposition holes.

This supports the earlier assumption that at $r < r_R$ the gel does not flow but forms a rigid, albeit, expanding interface where the volume fraction is in the range 0.005 to 0.01. It is seen in Figure 6-1 that for an ionic strength of 0.01 mM the diffusion coefficient of the gel/sol is still high at lower volume fractions. This implies that the smectite particles will "rapidly" diffuse out into any mobile water and be carried away. For ionic strengths larger than 1 mM the diffusion coefficient drops by two to three orders of magnitude and the release of smectite to water will be much lower.

ϕ_R , $D(\phi_R)$ and η_{rel} all depend on ion concentration c in a complex way. ϕ_R is influenced by the co-volume fraction, which increases for a given ϕ when c decreases because the diffuse double layer increases in size when c decreases. A lower c will move ϕ_R to lower values of ϕ in the shaded area in Figure 6-1. The diffusion coefficient curve will also move to the left.

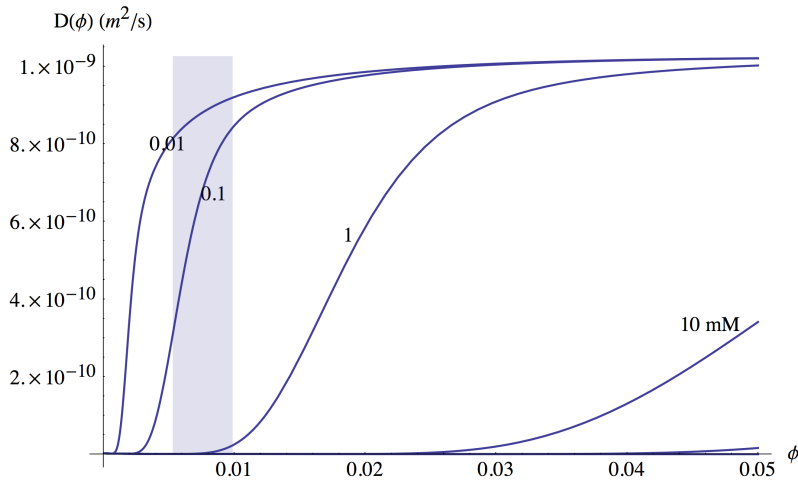


Figure 6-1. Diffusion coefficient $D(\phi)$ for the gel/sol as function of the volume fraction ϕ for different concentrations of monovalent ions.

Below we explore how this influences the diffusion coefficient at the rim, i.e. when the gel/sol just becomes mobile. The diffusion coefficient in this region will directly impact how fast the particles can diffuse into and in the mobile gel/sol. If the gel/sol can start to flow when the co-volume fraction at the rim $\phi_{cov}=1$ the relative viscosity jumps from infinity at the inner border of the rim to 3.4 and then decreases gradually to 1 at lower ϕ . If the jump occurs at $\phi_{cov}=2$ the relative viscosity at the rim border jumps at a value of 13.9. At the largest measured relative viscosity the relative viscosity is 10 and the co-volume fraction $\phi_{cov}=1.6$. The discontinuity in the viscosity directly impacts the velocity at the rim. The velocity will be 3.4 to 13.9 times lower than in smectite free water.

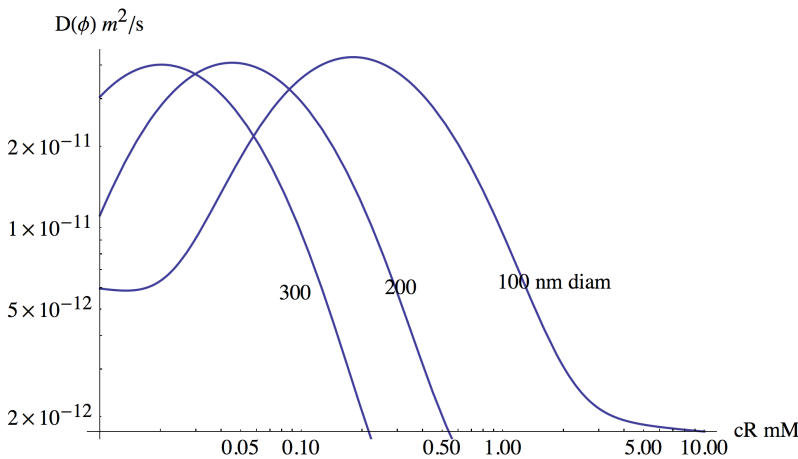


Figure 6-2. Diffusion coefficient at the rim as function of ion concentration at rim for different size colloidal particles for $\phi_{cov}=1.6$.

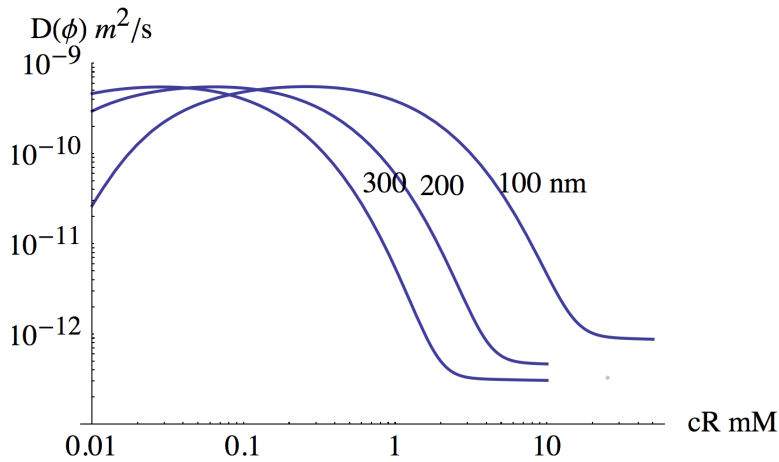


Figure 6-3. Diffusion coefficient at the rim as function of ion concentration at rim for different size colloidal particles for $\phi_{cov}=2.0$.

Figures 6-1 and 6-2 show the diffusion coefficient of the particles at the rim where the gel turns from a Newtonian fluid to an immobile Bingham fluid/solid. It is seen that the results are very sensitive to at what ϕ_{cov} the gel becomes rigid. At a value 1.6 the diffusivity at the rim border is at most $3 \times 10^{-11} \text{ m}^2/\text{s}$ for a wide range of particle sizes. For a ϕ_{cov} value of 2.0 the largest diffusivity is $6 \times 10^{-10} \text{ m}^2/\text{s}$, which is 20 times larger and close to the maximum value of diffusivity over the whole range of volume fractions of interest. The loss of smectite particles will therefore be very sensitive to the non-Newtonian behaviour of the gel in the region where it becomes rigid. There is at present not sufficient experimental data on gel behaviour at very low shear strengths to remedy this uncertainty. This uncertainty will have a large impact on the release rate as it would increase proportionally to the square root of increase in D , i.e. a factor up to 4 to 5, if the gel becomes rigid at ϕ_{cov} 2 instead of 1.6, all other conditions being the same.

The figures also show that the smectite particle diameter can have a strong impact on how they may be mobilised in the rim zone. As the smectite particles have a distribution of sizes this adds to the uncertainties of using the simple model discussed here as it will for other models unless it would be specifically addressed. The impact of some other important factors is explored in the next section.

7 Exploration of details in the rim

The discussion so far has to some extent been qualitative supported by some simplified quantitative examples. It was found that the conditions in the rim zone and especially at the interface between the rigid gel and the flowing gel/sol will influence the release rate at the rim. In this section the impact of the changing viscosity, diffusivity and the volume fraction within the rim zone is explored.

7.1 Mathematical description of the processes in the rim zone

The expansion of the gel can be modelled as a diffusion process with a diffusivity that is strongly influenced by the smectite concentration and the water composition (Liu et al. 2009a, Neretnieks et al. 2009). In the simplified model presented below we assume that the water ion composition in the rim is constant and known. In earlier modelling the simultaneous diffusion of cations was also included (Moreno et al. 2010 and 2011). In these references the full set of equations are presented. It was there found that the change in ion concentration in the rim was limited and was not very different from that in the approaching water. Excluding the changes in water ion concentration in the rim considerably simplifies the problem.

The following equations describe the situation. In the Cartesian coordinates used to model the rim the approaching water has a constant velocity u_x in the x-direction driven by a pressure gradient in that direction. It is further assumed that the pressure gradient is maintained in the entire thin rim. However, as the gel in the rim is viscous the velocity in x-direction slows down. This generates some flow in the perpendicular direction y.

The flow velocity in the x-direction is influenced by the local viscosity η , which is strongly influenced by the volume fraction ϕ of the smectite in the gel.

$$u_x = -\frac{\tau_o}{\delta_{frac}} \frac{\eta_w}{\eta(\phi)} \frac{dP}{dx} \frac{1}{\rho_w g} \quad (7-1)$$

The change in velocity in x-direction generates a movement in the y-direction to maintain the mass balance. The equation of continuity describes this.

$$\frac{\partial u_x}{\partial x} + \frac{\partial u_y}{\partial y} = 0 \quad (7-2)$$

The equation that describes the evolution of the smectite concentration in the gel is

$$\frac{\partial \phi}{\partial t} = \frac{\partial}{\partial x} \left(D(\phi) \frac{\partial \phi}{\partial x} \right) + \frac{\partial}{\partial y} \left(D(\phi) \frac{\partial \phi}{\partial y} \right) - u_x \frac{\partial \phi}{\partial x} - u_y \frac{\partial \phi}{\partial y} \quad (7-3)$$

In the thin rim the rate of diffusion in the x direction is $\frac{\partial}{\partial x} D(\phi) \frac{\partial \phi}{\partial x} \ll \frac{\partial}{\partial y} D(\phi) \frac{\partial \phi}{\partial y}$ and can be neglected. The velocity in the y-direction is much smaller than in the x-direction $u_y \ll u_x$, but

$u_y \frac{\partial \phi}{\partial y}$ can be of the same order of magnitude as $u_x \frac{\partial \phi}{\partial x}$ because the concentration gradient in the y-direction is much larger than in the x-direction. A further simplifying assumption is then used by setting $u_y \frac{\partial \phi}{\partial y} + u_x \frac{\partial \phi}{\partial x} = \alpha u_x \frac{\partial \phi}{\partial x}$ where α is expected to be on the order of 1. It is seen

that α has the same influence as the velocity. The impact of this simplification will be tested by comparing the release rate with this approximation with that from the simple Q_{eq} model and by comparison with numerical solutions where this approximation is not made.

At steady state a mass balance for the smectite concentration can be written for the situation depicted in Figure 3-2, setting α to 1, as follows

$$\frac{\partial}{\partial y} D(\phi) \frac{\partial \phi}{\partial y} = \frac{u_o}{\eta(\phi)} \frac{\partial \phi}{\partial x} \quad (7-4)$$

with boundary conditions

$$\text{for } x \leq 0 \quad \phi = 0 \quad (7-5)$$

$$\text{at } y=0 \quad \phi = \phi_R \quad (7-6)$$

$$\text{for } y \rightarrow \infty \quad \phi \rightarrow 0 \quad (7-7)$$

The model of Liu (2009) and Liu et al. (2009a) for smectite diffusion coefficient is used for $D(\phi)$. It is lengthy and is not reproduced here. The behaviour of the diffusivity was illustrated in Figure 3-1 for pure sodium smectite.

The gel viscosity $\eta(\phi)$ is strongly influenced by smectite concentration and water composition. Figure 7-1 shows the relative viscosity as function of smectite concentration for three different ion concentrations. The relation is valid up to around $\phi = 0.01$. The shaded vertical line indicates the region where the relation is not valid at the shear rates expected. It may be noted that there only is experimental data up to a volume fraction about 0.01 to support this. In our simplified model we assume that above some volume fraction ϕ_R the viscosity increases beyond bounds and gel velocity becomes zero.

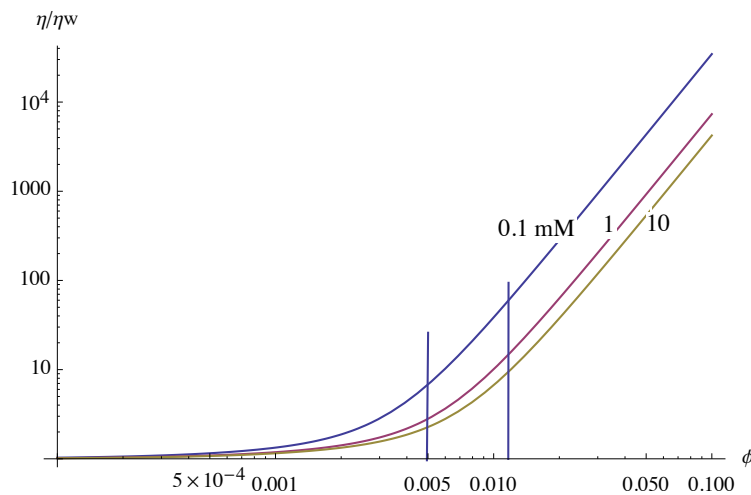


Figure 7-1. Relative viscosity as function of volume fraction of smectite for monovalent cation concentrations 0.1, 1 and 10 mol/m³ from top down. The two vertical lines indicate the region where the gel may become rigid.

The equations to solve can be expected to be strongly non-linear and will have to be solved with high resolution around the sharp front at the rim. When the diffusivity and viscosity is constant, or do not vary very much, ordinary finite difference, finite element methods or the method of lines give rapid and accurate solutions. For more non-linear conditions errors increase and strong non-linearities cause the methods can break down.

7.2 Examples using the 2D rim model

The solutions to equations (7-4 to 7-7) presented are obtained by the “method of lines” in Mathematica[®]. Figures 7-2a and b show the volume fraction ϕ and flux $u\phi$ for a case with *constant diffusivity* but varying viscosity for a boundary concentration $\phi_R = 0.04$ and monovalent ion concentration of 1 mol/m^3 . A value ϕ_R higher than the expected is used in the simulations below. This will cause the viscosity to rise sharply in the rim. The results show smooth curves and the solver behaves well with the quite steep viscosity profile at the boundary where the relative viscosity is 92 at the inner border of the rim.

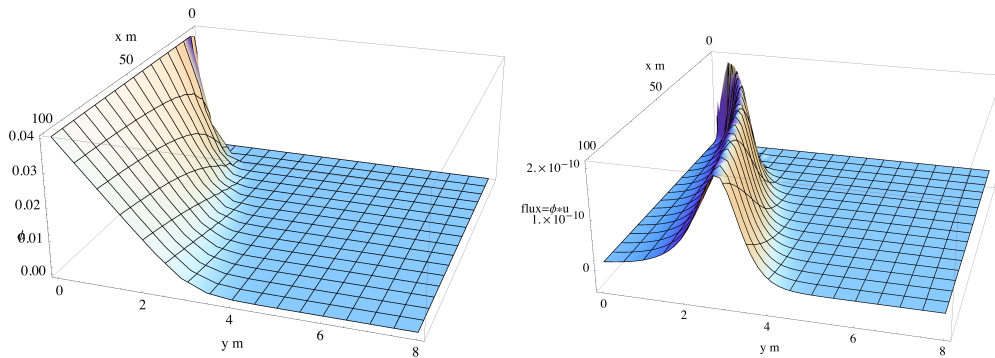


Figure 7-2a (left) volume fraction ϕ and 7-2b (right) flux ϕu . Ion concentration is 1 mol/m^3 and velocity is 10^{-7} m/s . Constant diffusivity and variable viscosity is used.

Including also variable diffusivity gives the results shown in Figure 7-3.

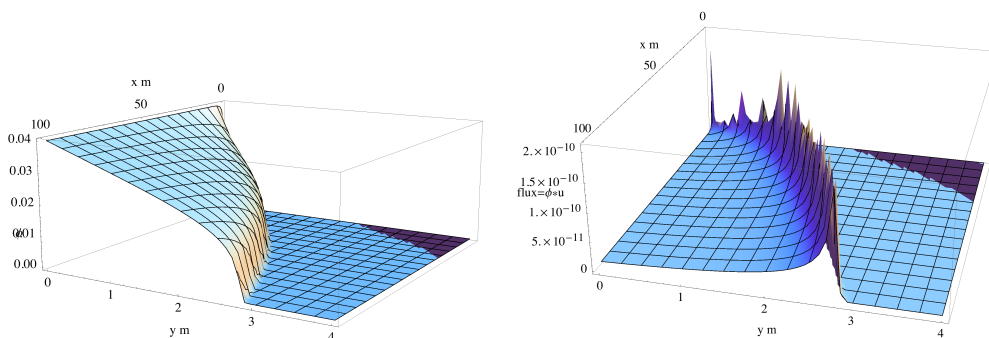


Figure 7-3a (left) volume fraction ϕ and 7-3b (right) flux ϕu . Ion concentration is 1 mol/m^3 and velocity is 10^{-7} m/s . Variable diffusivity and viscosity.

The front is very steep and the rim sharp and thin. The discretisation in this case was minimum 200 lines in the method of lines using 4th order finite differences. Five times as many lines or smaller or larger order of finite differences did not much improve the details at the front and the release rates of smectite changed only little.

The variable diffusion coefficient evaluation using the “exact” model (Liu et al. 2010) gave rise to very long computation times and sometimes caused numerical breakdowns for some combinations of parameters. To remedy this the diffusion function was fitted to simpler expressions. One such approximation was the Error function *Erf*. An example of this given in Figure 7-4. One drawback of using the error function approximation is that it does not account for the dip. Two variants were tested. In the first, which is shown in Figure 7-5 the *Erf*-curve was forced to drop to the values for the smallest volume fraction, essentially zero. In the other variant it was forced to drop the minimum value in the “dip” and remain there also at lower volume fractions. Test showed that the smectite loss was practically the same for the two

variants. The other approximation was to use interpolation of tabulated values of the diffusion function. This gave results that differ by less than 5×10^{-9} in relative values of the “exact” diffusivity function over the whole range of ϕ . Interpolation was used in most calculations.

Computation times can easily become minutes and more if finer discretisation is used in the method of lines. In practice the extent of the y-region must be selected manually to span a good range of the studied region because the extent of the rim is quite different for different water velocities and ion concentrations.

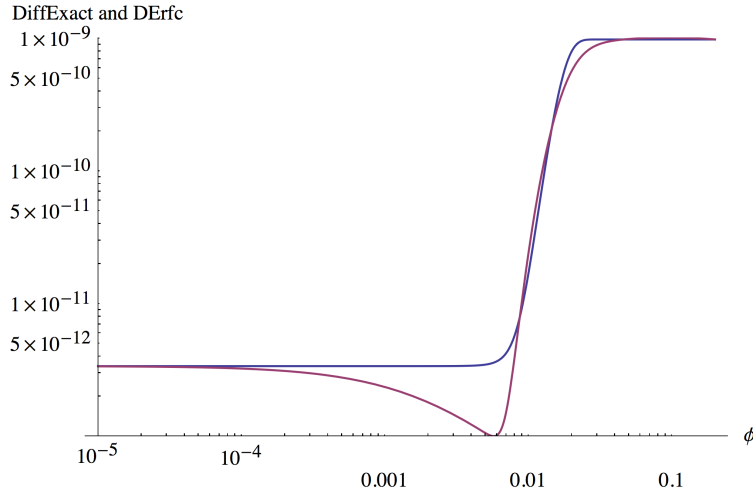


Figure 7-4. “Exact” and Erf fitted diffusivity function for $c=1 \text{ mol/m}^3$.

In all calculations it was found that the location of the smectite front as well as the smectite flowrate, i.e. the loss of smectite N_{rim} obtained by the integral of ϕu over all y very closely followed \sqrt{x} . This is typical for instationary diffusion in unbounded regions. For nonlinear coefficient also the \sqrt{x} dependence of the propagation of the front can be expected (Crank 1975).

It has not been possible to make global error estimates of the numerical solutions but it is suspected that they can be considerable when the fronts become very sharp. We therefore explore another method also. We approach the problem by utilising the property that y is not bounded. This is described in the following section.

7.3 Transform of model from 2D to 1D

Equation 7-4 can be transformed to an ordinary differential equation (Bird et al. 2002, p 116).

Differentiating (7-4) gives

$$D(\phi) \frac{\partial^2 \phi}{\partial y^2} + \frac{dD(\phi)}{d\phi} \left(\frac{\partial \phi}{\partial y} \right)^2 = \frac{u_o}{\eta(\phi)} \frac{\partial \phi}{\partial x} \quad (7-8)$$

(7-8) is rearranged to

$$\frac{\eta(\phi)D(\phi)}{u_o} \frac{\partial^2 \phi}{\partial y^2} + \frac{\eta(\phi)}{u_o} \frac{dD(\phi)}{d\phi} \left(\frac{\partial \phi}{\partial y} \right)^2 = \frac{\partial \phi}{\partial x} \quad (7-9)$$

and to

$$f1(\phi) \frac{\partial^2 \phi}{\partial y^2} + f2(\phi) \left(\frac{\partial \phi}{\partial y} \right)^2 = \frac{\partial \phi}{\partial x} \quad (7-10)$$

with

$$f1(\phi) = \frac{\eta(\phi)D(\phi)}{u_o} \quad (7-11)$$

$$\text{and } f2(\phi) = \frac{\eta(\phi)}{u_o} \frac{dD(\phi)}{d\phi} \quad (7-12)$$

With a dimensionless diffusion coefficient $D_{DL} = D/D_o$ and the transform

$$z = \frac{y}{\sqrt{4 D_o t}} = \frac{y}{\sqrt{4 D_o x / u_o}} \quad (7-13)$$

D_o can conveniently be set to the maximum value in the range of interest.

(7-10) becomes an ordinary differential equation, ODE, of only one variable, z

$$f1(\phi) \frac{d^2 \phi}{dz^2} + f2(\phi) \left(\frac{d\phi}{dz} \right)^2 = -2z \frac{d\phi}{dz} \frac{D_o}{u_o} \quad (7-14)$$

The transform applied to the boundary conditions gives

at

$$z = 0 \quad \phi = \phi_o \quad (7-15)$$

and for

$$z \rightarrow \infty \quad \phi = 0 \quad (7-16)$$

Attempts to solve this boundary value problem by a finite difference method did not result in sufficiently good resolution because of the very sharp front that gives a very stiff problem. The problem is therefore solved by the shooting method. In the shooting method the problem is redefined from a boundary value problem to an initial value problem. The second boundary condition (7-16) is changed to

$$z = 0 \quad \frac{d\phi}{dz} = k \quad (7-17)$$

The value of k is not known so the problem is solved iteratively. Equation (7-14) is solved for different k 's in a systematic way until (7-16) is satisfied. This is called the shooting method and is automated. Some reasonable starting value for k must be supplied. This method of solving boundary value problems has the advantage that the step-length (discretization) easily can be adapted locally so that the step-length can be decreased to extremely short steps where the front is very steep. Also special stiffness handling methods are available in many commercial solvers for initial value problems.

7.4 Examples using the 1D rim model

The rim model makes it possible to account for varying viscosity as well as diffusivity in the rim. The co-volume ϕ_{Cov} at the rim where the gel becomes rigid has a large influence on the conditions in the rim. It will set the viscosity of the gel/sol at the rigid gel interface as well as the volume fraction there. ϕ_{Cov} is expected to be about 1.6 but it may be larger and no adequate experimental measurement have been found to determine it more accurately. Therefore a range $1.6 < \phi_{Cov} < 4$ is used to explore its impact.

Figure 7.5 shows the concentration profile in the rim zone for $\phi_{Cov} = 1.6$, $u=10^{-5}$ m/s and $c=0.1$ mM monovalent ions.

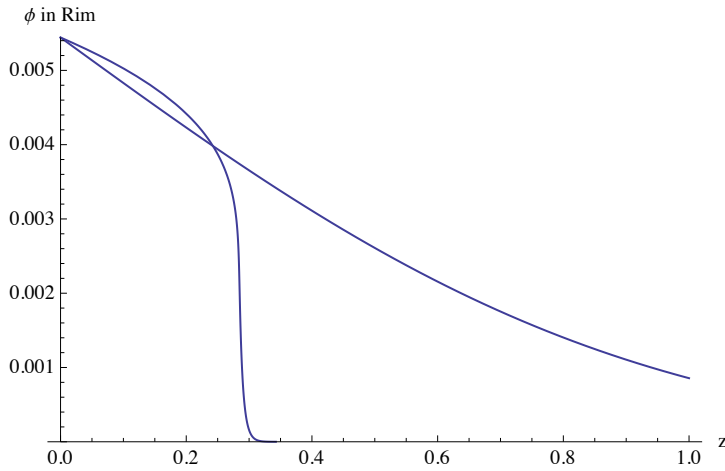


Figure 7.5. concentration profile in the rim zone, $\phi_{cov} = 1.6$, $u=10^{-5}$ m/s and $c=0.1$ mM monovalent ions. The upper curve is for constant D and viscosity.

The upper curve shows the profile for constant D and viscosity. The volume fraction at the border of the rigid gel is 0.0054 for $\phi_{cov} = 1.6$. The lower curve shows that the concentration profile drops sharply to zero at z around 0.25. For illustration it may be noted that in this example at a rim length of 25 m the rim thickness is 0.25 m, i.e. only 1 % of the travel distance. It is quite thin compared to the flow length, which would result from the flow around one side of a cylinder with 8 m radius. This also illustrates that if one wants to use a finite element code to solve the simultaneous radial expansion of the gel in a fracture and the flow and diffusion in the rim a very fine discretisation of the 2 D region is needed to capture the details of the rim zone. A remedy may be to use adaptive grid methods that readapt the mesh sizes continuously. This has not been tried.

Figure 7.6 shows a relative measure of the flux ϕu defined as $\int_0^\infty \frac{\phi(y)}{\eta_{rel}} dy$ from Equation 5-1 in the rim zone. For illustration it is shown that the flux in the front becomes even sharper when ϕ_{cov} increases from 1.6 to 2.0.

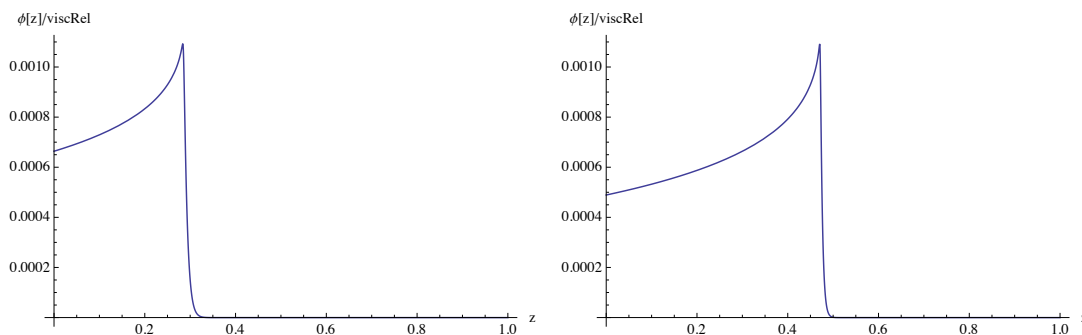


Figure 7-6. Relative measure of the flux ϕu in the rim zone, $u=10^{-5}$ m/s and $c=0.1$ mM. Left figure is for $\phi_{cov} = 1.6$. The right is for $\phi_{cov} = 2.0$.

Figures 7.7 and 7.8 show the same curves for $c=1$ mM for otherwise the same conditions.

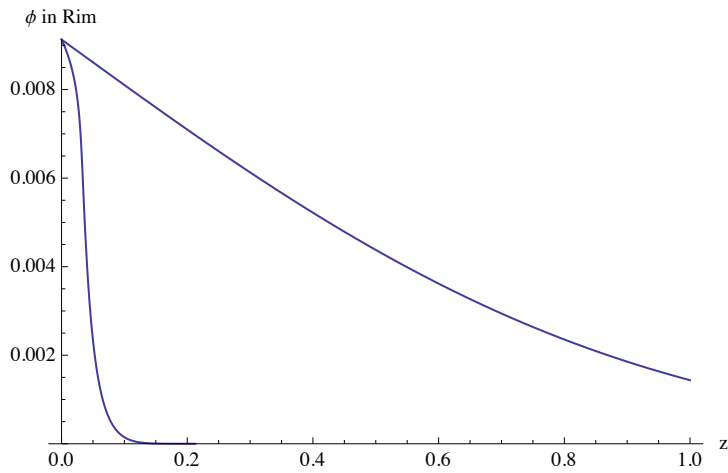


Figure 7-7. concentration profile in the rim zone, $\phi_{cov} = 1.6$, $u=10^{-5}$ m/s and $c=1$ mM monovalent ions. Right hand curve is for constant D and viscosity.

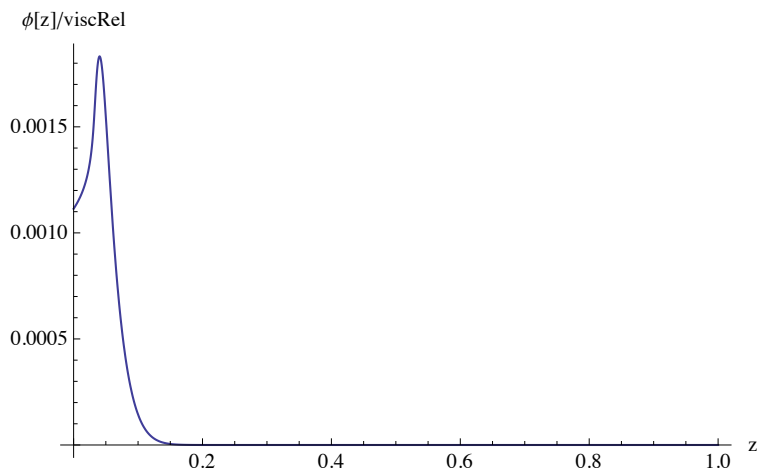


Figure 7-8. Relative measure of the flux ϕu in the rim zone, $u=10^{-5}$ m/s and $c=1$ mM.

Both the diffusivity D_R and ϕ_R change at the rim boundary as the ion concentrations change. For a given co-volume the relative viscosity is the same as shown in Table 7.1. It is also seen that Q_{eq} is largest at the lowest ion concentration. This is because D has not started to decrease yet at volume fractions lower than ϕ_R at the rim border and the smectite particles can more easily diffuse into the seeping water.

Table 7.1. Volume fraction, diffusivity, relative viscosity at the rim border and Q_{eq} as well as radius of rim at steady state, SS, at three different ion concentrations for $\phi_{ri} = 0.4$ and $\phi_{Cov} = 1.6$. Water velocity is 10^{-5} m/s or 315 m/yr.

c mM	D_R m ² /s	ϕ_R	η_{rel}	Q_{eq}/δ_{frac} $/\sqrt{r_R u_o}$ m s ^{0.5}	r_R at SS m	N_{SS} g/year	$Q_{eq}DRVR/Q_{eq}ODE$
0.1	3.1×10^{-10}	0.0054	8.2	8.74×10^{-6}	18.8	53.1	3.2
1	1.2×10^{-11}	0.0091	8.2	2.36×10^{-6}	50.8	39.9	2.3
10	5.7×10^{-13}	0.011	8.2	1.97×10^{-6}	49.8	39.8	0.60

The data have been obtained by firstly choosing D for the gel at high compaction using the dynamic model (Ch 3) for use in Equation (3-6). A value of $D = 8 \times 10^{-9}$ m²/s was chosen in this example for the three ion concentration in table 7-1. This is just below the maximum value in the interval $0.1 < \phi < 0.5$. ϕ_R and η_{rel} are obtained from the gel viscosity model (Ch 6) for $\phi_{Cov} = 1.6$. Q_{eq} is then obtained by solving the ODE, Equations (7-14 to 7-17), which gives the relation in column 5. The steady state radius r_{SS} and loss N_{SS} is then found by solving Equation (3-1).

For comparison the simple $Q_{eq,DRVR}$ model Equation (5-3) with the diffusion coefficient at the rim D_R (column 2) and velocity u_o reduced by a factor equal to the relative viscosity η_{rel} (column 4). The last column give the ratio between $Q_{eq,DRVR}$ and the Q_{eq} obtained by the ODE model. The simple $Q_{eq,DRVR}$ model overestimates the loss to the seeping water at low ion concentrations but underestimates it for higher ion concentrations.

The radius of the rim at steady state increases considerably with decreasing velocity. At $u_o = 10^{-6}$ m/s r_R is 84, 259, and 253 m at steady state for $c = 0.1, 1$ and 10 mM respectively. These distances in the intruded fracture would contain more smectite than there is in a deposition hole and those radii would be reached after much longer times than 10 000 years.

If $\phi_{Cov} = 2.0$ is used to assess when the gel becomes rigid instead the relative viscosity at the rim increase to 13.9 and the values of Q_{eq} and r_R in Table 7.1 change to those in Table 7.2.

Table 7.2. Volume fraction, diffusivity, relative viscosity at the rim border and Q_{eq} as well as radius of rim at steady state at three different ion concentrations for $\phi_{Cov} = 2.0$. Water velocity is 10^{-5} m/s or 315 m/yr.

c mM	D_R m ² /s	ϕ_R	η_{rel}	Q_{eq}/δ_{frac} $/\sqrt{r_R u_o}$ m s ^{0.5}	r_R at SS m	N_{SS} g/year	$Q_{eq}DRVR/Q_{eq}ODE$
0.1	5.3×10^{-10}	0.0068	13.9	9.30×10^{-6}	13.2	59.8	3.0
1	5.9×10^{-11}	0.011	13.9	2.46×10^{-6}	37.2	42.9	3.8
10	4.7×10^{-13}	0.014	13.9	1.59×10^{-6}	45.6	39.9	0.5

Q_{eq} is not overly sensitive to the choice of the value of ϕ_{Cov} in the interval deemed to be realistic.

7.5 Comparison with “exact” solution in rim where advection perpendicular to the rim is not neglected.

In the previously described rim model the equation of continuity was neglected in order to obtain a model that could be solved as an ordinary differential equations, ODE. This can be used to handle very sharp fronts. In this section the approximation is not made in order to assess the errors the approximation gives rise to. Equations (7-2 and 7-3) are solved by a finite element code in Comsol Multiphysics[®]. This code was used in an earlier study to solve the coupled equation for smectite expansion and ion migration for the radial expansion of smectite gel and loss of smectite at the rim by uptake in the seeping water that carries away the particles, Moreno et al. (2009, 2010). Some problems of stability of the solutions were encountered as well as some concerns that the accuracy of results were difficult to validate. Also the need for very fine discretisation of the model area resulted in uncomfortably long computation times. For the present simulations the task is simpler because the transport of the chemical species is not included and a linear rim is modelled where the boundary of the rim is stationary.

A comparison is made between the results when the simplification is not made and when it is. In the figures below water flows from left to right. The smectite is located in the region $0.8 < x < 3.2$ m. The volume fraction is 0.4 at $y=0$ and the gel expands upward. Because of its extremely high viscosity it cannot flow until it is diluted due to it being carried away by the flowing gel/sol at some distance from $y=0$. The smectite is allowed to expand up-streams. As the water velocity in the x-direction slows down the rim is forced to move upward by the velocity in the y-direction generated by slowing down of the velocity in the x-direction. The rim zone becomes curved as shown in Figure 7-9.

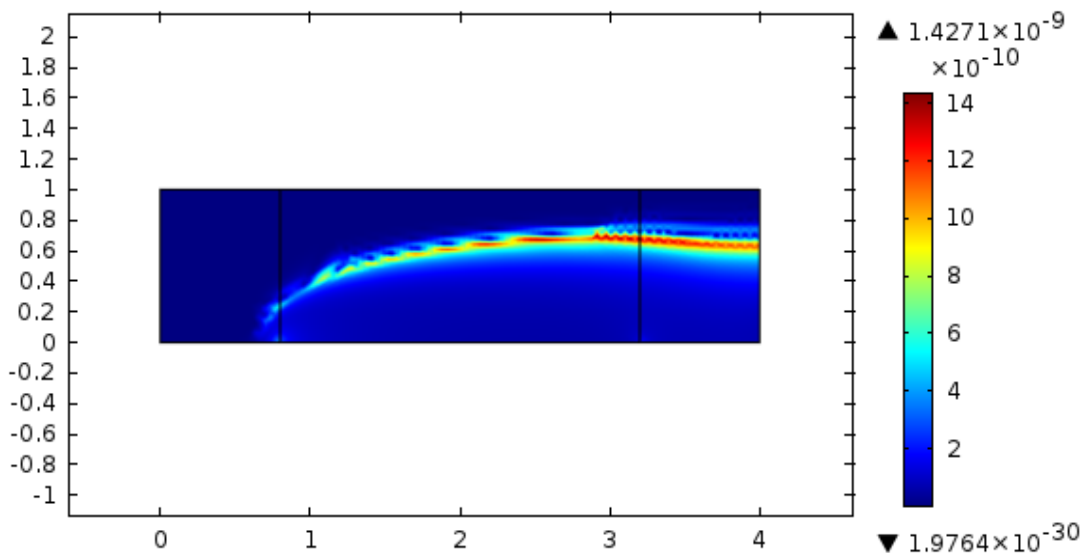


Figure 7-9. Flowrate in rim past a 2.4 m long flat border $u_o=32$ m/year, aperture=1 mm, No approximation is used, $N_{rim}= 0.0146$ kg/year.

When the velocity in the y-direction is forced to be zero the rim zone becomes straight as shown in Figure 7-10. The rate of smectite transport downstream does not, however, differ more than 6 % between the cases. Considering that there are also errors in both solutions, as

can be seen by the wriggling rim zones in the figures, the approximation is deemed to be acceptable.

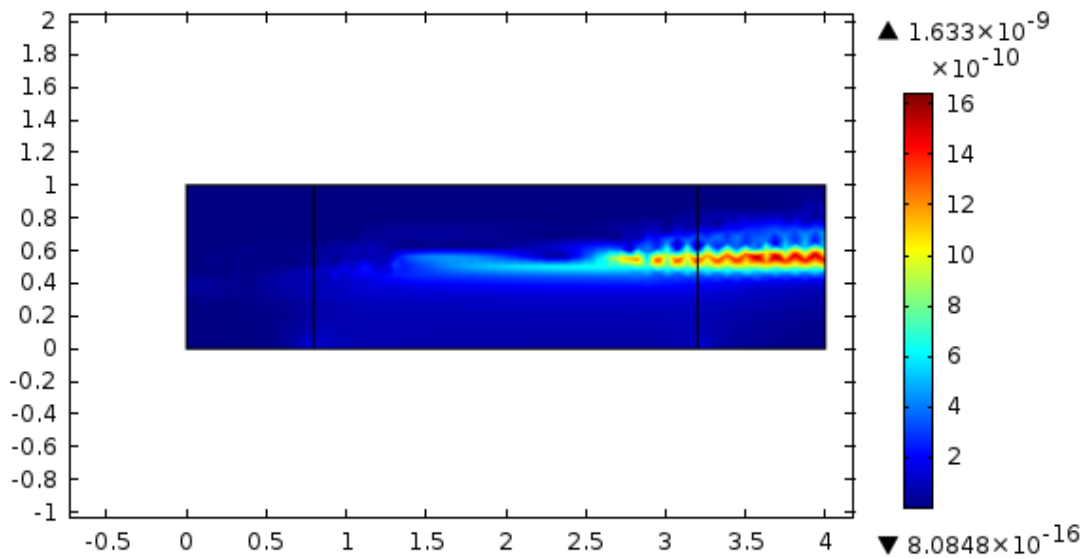


Figure 7-10. Flowrate in rim past a 2.4 m long flat border $u_o=32$ m/year, aperture=1 mm, Approximation is used, $N_{rim}=0.0138$ kg/year.

7.6 Comparison with earlier result

In Table 7.3 a comparison is made between the results obtained by the two-stage model described in Chapter 7 and the results in Moreno et al. (2009). The radius to the rim at SS in the two-stage model is considerably larger and the loss to the seeping water is smaller. The two-stage model results imply that the rate of loss from the deposition hole is dominated by the rate of intrusion into the fracture over a very long period of time even when the loss to seeping water may be smaller.

Table 7.3. Comparison the steady state loss N_{SS} between 2-stage model and earlier results (Moreno et al 2009) for three different water velocities for $c=0.1$ mM and $\phi_{cov} = 1.6$ (2.0).

Water velocity m/yr	N_{SS} g/ year two stage model	N_{SS} g/ year Moreno et al. (2009)	Radius to rim r_R m, two-stage model	Radius to rim r_R m, Moreno et al. (2009)
315	53.1 (59.8)	292	18.8 (13.2)	1.4
31.5	36.6 (39.4)	117	84.5 (58.4)	3.0
3.15	26.5 (28.4)	43	463 (302)	7.9

7.7 Some comments on the model and the results presented in this chapter.

The approximations in the rim model permits the use of a simple transform to reduce a two-dimensional partial differential diffusion problem to an ordinary differential boundary value

problem. It was shown in section 7.5 that the omission of the velocity component in the direction perpendicular to the rim gave errors that should be acceptable considering other uncertainties connected to the problem at hand. It was also found in chapter 5 that the error in using the steady state solution of concentration profile as a proxy for the instationary is on the order of less than a factor 2 during the instationary phase and decreases to zero at steady state.

8 Analytical approximations of the expansion of the smectite front

8.1 Introduction

It was found in the chapter 5 that the concentration profile in the expanding region was similar to that when there was no loss except at the rim where it dropped sharply.

To gain further insights and to obtain simpler equations, in this section a pseudo steady state (PSS) approach is used to simplify the rate of expansion of the gel/sol. It is assumed that shape the concentration profile does not change even when the sharp front moves further out with time and that the shape of the front is the same as when steady state is reached finally when the influx from the source becomes equal to the loss at the rim.

The equation we wish to solve is the diffusion equation for linearly and cylindrically radial expansion. This can be summarised in Equation (8.1) with $p=0$ for linear and $p=1$ for radial expansion for constant diffusivity.

$$\frac{\partial \phi}{\partial t} = \frac{D}{r^p} \frac{\partial}{\partial r} \left(r^p \frac{\partial \phi}{\partial r} \right) \quad (8.1)$$

The initial condition is that at time zero

$$\phi = 0, \text{ for all } r \quad (8.2)$$

The inner boundary condition is that ϕ is known at the source. It can be a function of time and may be influenced by the rate of loss due to influx into the fracture

$$\phi = \phi_i(t) \quad (8.3)$$

8.1.1 The case of constant concentration in the source

We expect that ϕ_i will not change very rapidly in the cases of interest for us. The other boundary condition is that at the rim where $\phi = \phi_R$ the smectite is lost at a rate equal to the equivalent flowrate times the concentration at the rim. For radial expansion Q_{eq} is expected to increase with the radius to the rim, see chapter 7. The gradient at the rim can be related to Q_{eq} as

$$-\left. \frac{d\phi}{dr} \right|_{r=r_R-} = \frac{Q_{eq}(r_R)\phi_R}{DA_R} \quad (8.4)$$

A_R is the cross section area of the fracture at r_R at which the seeping water carries away the smectite sol. The minus in r_{R-} indicates that the gradient is evaluated at the rim just inside of the rim. At the rim the volume fraction drops abruptly from ϕ_R to $\phi = 0$. We have explored several methods to incorporate this boundary condition into numerical schemes based on finite different, finite element methods and in the method of lines but have not succeeded to develop reliable solutions so far.

In the present analytical approximate model we make several simplifying assumptions in order to obtain a simple solution. One is that the diffusivity is constant in the whole range of smectite concentrations. Another is that ϕ_i is constant. A third is that the loss term determined by Q_{eq} is constant around the rim. In reality it changes with location but we use it to denote the entire loss around the whole rim. Later we will also the treat case where the rate of change in ϕ_i with time is small compared to other changes.

An analytical approximate method is developed and an estimate is made of the errors that can be expected. First the approach to the solution is presented and it is illustrated for linear

expansion. The linear case is simpler and better used to illustrate the idea than the radial expansion case. An error estimate is made by comparing the solution to the exact solution for a simple case when the concentration at the rim ϕ_R approaches zero and thus there is negligible loss at the rim. It is shown to give an error less than 13 %. In the same way a solution is presented for radial expansion where also the change of the smectite concentration in the source is accounted for due to the loss from the source. Some examples are used to illustrate the rate of expansion of the rim and the loss from the source over time.

8.1.2 Linear diffusion for PSS

As the distance to the rim increases, eventually expansion will stop when steady state is reached. The profile will stabilize at a distance $r_R = r_{RSS}$ where in-diffusion from the source equals the rate of loss at the rim. For the *linear* diffusion case the concentration profile is straight. A and Q_{eq} are constant for linear diffusion and the mass flux J into the fracture is

$$\frac{1}{\rho_s} J = D \frac{\phi_i - \phi_R}{r_{RSS}} = \frac{Q_{eq} \phi_R}{A} \quad (8.5)$$

giving the steady state distance

$$r_{RSS} = \frac{\phi_i - \phi_R}{\phi_R} \frac{DA}{Q_{eq}} \quad (8.6)$$

The concentration profile is straight up to r_R

$$\phi(r) = \phi_R + (\phi_i - \phi_R) \left(1 - \frac{r}{r_R}\right) \text{ for } r_i < r < r_R \quad (8.7)$$

This is illustrated in Figure 8-1 where the sharp front is seen to move without changing shape of the concentration profile, a straight line in this case. This is not correct because the profile will be concave as the front expands. However, when the loss at the rim is equal to the influx the front stops moving and the profile becomes straight. It will be shown later that the rate of influx into fracture calculated from the exact solution when ϕ_R approaches zero gives the same results.

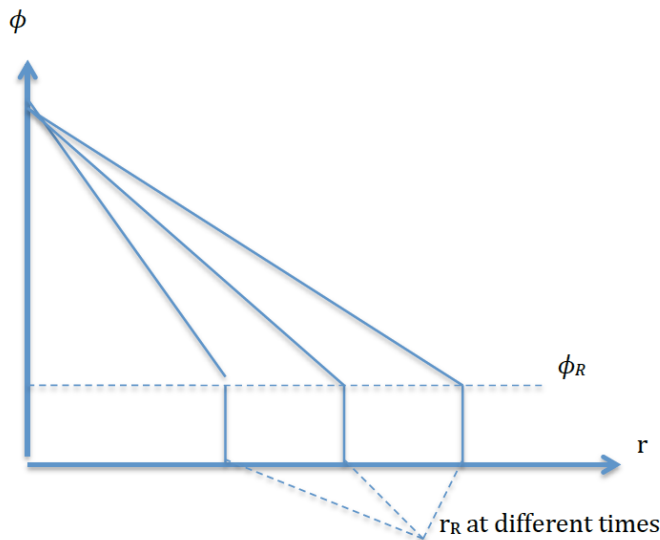


Figure 8-1. The sharp front moves to larger distances with time.

The smectite accumulates in the fracture as the front moves and a mass balance can be set up from which the rate of the movement can be determined. The smectite mass M_s in the fracture

changes with time assuming in this case that ϕ_i is constant. We return later to the case when ϕ_i slowly changes with time.

$$\frac{1}{\rho_s} \frac{dM_s}{dt} = -DA \left. \frac{d\phi}{dr} \right|_{r=r_i} - Q_{eq} \phi_R = DA \frac{\phi_i - \phi_R}{r_R} - Q_{eq} \phi_R \quad (8.8)$$

For linear diffusion A is constant and r_i can conveniently be set $r_i = 0$. M_s is obtained by integrating the profile.

$$\frac{1}{\rho_s} M_s = A \int_0^{r_R} \phi(r) dr = \int_0^{r_R} (\phi_R + (\phi_i - \phi_R)(1 - \frac{r}{r_R})) dr \quad (8.9)$$

$$\frac{1}{\rho_s} M_s = \frac{1}{2} (\phi_i + \phi_R) A r_R \quad (8.10)$$

M_s changes with time as

$$\frac{1}{\rho_s} \frac{dM_s}{dt} = \frac{1}{2} (\phi_i + \phi_R) A \frac{dr_R}{dt} \quad (8.11)$$

The gradient at the inlet is

$$\left. \frac{d\phi}{dr} \right|_{r=0} = - \frac{\phi_i - \phi_R}{r_R} \quad (8.12)$$

From (8.8), (8.10) and (8.11)

$$\frac{A \frac{dr_R}{dt} (\phi_i + \phi_R)}{2} = DA \frac{\phi_i - \phi_R}{r_R} - Q_{eq} \phi_R \quad (8.13)$$

which can be rearranged to

$$\frac{dr_R}{dt} = D \frac{\phi_i - \phi_R}{\frac{r_R(\phi_i + \phi_R)}{2}} - \frac{Q_{eq} \phi_R}{\frac{A(\phi_i + \phi_R)}{2}} = \frac{a}{r_R} - b \quad (8.14)$$

where

$$a = D \frac{\phi_i - \phi_R}{\frac{(\phi_i + \phi_R)}{2}} \quad (8.15)$$

and

$$b = \frac{Q_{eq} \phi_R}{\frac{A(\phi_i + \phi_R)}{2}} \quad (8.16)$$

For the initial condition $t = 0$, $r_R = 0$ the solution is

$$r_R(t) = \frac{a(1 + \text{ProductLog}\left[-e^{-1 - \frac{b^2 t}{a}}\right])}{b} \quad (8.17)$$

As an illustration for $a=1 \text{ m}^2/\text{yr}$ and $b=1 \text{ m}/\text{yr}$, $r_R(t)$ is plotted in Figure 8-2.

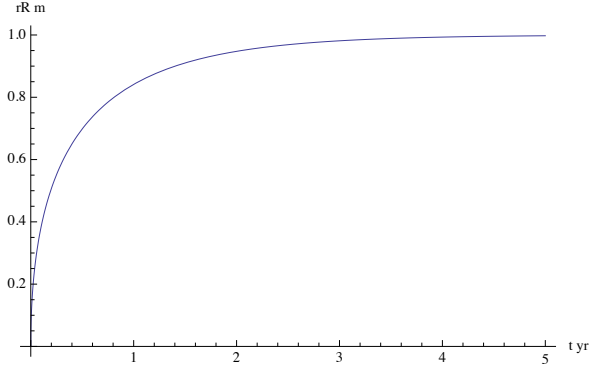


Figure 8-2. Distance r_R versus time.

When there is loss at the rim, $b > 0$, it is seen that r_R approaches a steady state value.

Below we explore a limiting case when $\phi_R \rightarrow 0$. Then $b \rightarrow 0$. For $b=0$, i.e. there is no loss at the rim the expansion has no limit. When $b = 0$ Equation (8.1) has an analytic solution (Carslaw and Jaeger 1959) and a comparison can be made of the rate of loss between the PSS solution and the exact solution. This comparison is made below. For the PSS solution for $b=0$ Equation (8.17) simplifies to

$$r_R(t) = \sqrt{2at} = 2\sqrt{Dt} \quad (8.18)$$

The flux J_{PSS} into the fracture as it evolves with time is

$$\frac{1}{\rho_s} J_{PSS} = \frac{\phi_i}{2} \sqrt{\frac{D}{t}} \quad (8.19)$$

The mass in the fracture M_{PSS} is

$$M_{PSS} = A\rho_s \int_0^t J_{PSS}(t') dt' = A\phi_i \sqrt{Dt} \quad (8.20)$$

The mass in the fracture increases with the square root of time.

Below is a comparison of the PSS solution with the exact solution for the limiting case when $\phi_{R-} \rightarrow 0$. The exact solution to Equation (8.1) for linear diffusion with no loss at the rim and constant D with boundary condition $\phi = \phi_i$ and the initial condition $\phi = 0$ and the outer boundary condition that at infinite distance $\phi = 0$ is, (Bird et al. 2002).

$$\phi = \phi_i \operatorname{Erfc}\left(\frac{r}{2\sqrt{Dt}}\right) \quad (8.21)$$

The gradient at the inlet is

$$\left. \frac{d\phi}{dr} \right|_{r=0} = -\phi_i \sqrt{\frac{1}{\pi Dt}} \quad (8.22)$$

The flux is

$$\frac{1}{\rho_s} J = \phi_i \sqrt{\frac{D}{\pi t}} \quad (8.23)$$

and the mass in the fracture M is

$$M = A\rho_s \int_0^t J(t') dt' = A\phi_i \frac{2}{\sqrt{\pi}} \sqrt{Dt} \quad (8.24)$$

It is seen that the PSS solution (8.20) underestimates the flux and the mass in the fracture by a factor $\frac{2}{\sqrt{\pi}}$, which is about 13% compared to (8.24) at all times when the loss at the rim can be neglected. When there is loss at the rim the distance to the rim will reach a steady state distance r_{RSS}

$$r_{RSS} = \frac{a}{b} = \frac{\phi_i - \phi_R}{\phi_R} \frac{DA}{Q_{eq}} \quad (8.25)$$

With time the concave profile straightens and when SS is reached the profile becomes linear. This implies that as long as $r \ll r_{RSS}$ the loss at the rim is small compared to the influx of mass in the fracture. When $r = r_{RSS}$ the PSS solution is correct because SS has been reached, the influx is equal to the loss at the rim and the gradient is constant. Thus using the PSS approximate solution will underestimate the loss from the source by 13 % for early times when $r < r_{RSS}$ and the will become increasingly accurate with time. We deem the discrepancy to be acceptable for the present purposes.

8.1.3 Radial diffusion for cylindrical coordinates

In the same way as for the linear case the steady state profile for cylindrical coordinates, (8.26), is used for the PSS approximation. The steady state profile is

$$\phi(r) = \phi_i - (\phi_i - \phi_R) \frac{\ln\left(\frac{r}{r_i}\right)}{\ln\left(\frac{r_R}{r_i}\right)} \quad \text{for } r_i < r < r_R \quad (8.26)$$

The gradient at the inlet at r_i is

$$\left. \frac{d\phi}{dr} \right|_{r=r_i} = - \frac{\phi_i - \phi_R}{r_i \ln\left(\frac{r_R}{r_i}\right)} \quad (8.27)$$

The smectite mass in the fracture between the inner and outer radii is

$$\frac{1}{\rho_s} M_s = 2\pi\delta_{fr} \int_{r_i}^{r_R} r\phi(r)dr \quad (8.28)$$

When ϕ_i is constant Equation (8.28) has the analytical solution

$$\frac{1}{\rho_s} M_s = 2\pi\delta_{fr} \left(\left(\frac{1}{2} (r_R^2 \phi_R - r_i^2 \phi_i) - \frac{(r_i^2 - r_R^2)}{4 \ln\left(\frac{r_R}{r_i}\right)} (\phi_i - \phi_R) \right) \right) \quad (8.29)$$

This expression can be used to determine the rate of movement of the rim in the same way as was done for the linear case, Equations (8.11) and following. The equations become lengthier and are not displayed here.

For the radial expansion an analytical solution for the rate of mass transport into the fracture for the PSS model could not be found as it was done for the linear expansion, Equation (8.20). However, a comparison between the exact solution of Equation (8.1) for radial diffusion (Carslaw and Jaeger 1959) and the numerical PSS solution of Equation (8.30) is shown in Figure 8-3 for the case when there is no loss at the rim $\phi_R = 0$ and ϕ_i is constant. The exact solution also in the radial case gives a 13 % larger inflow to the fracture than the PSS solution.

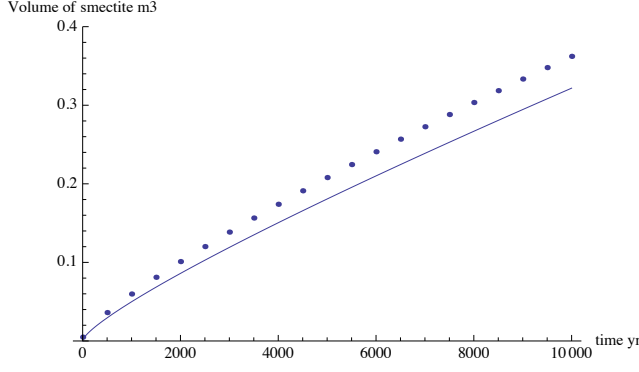


Figure 8-3. Comparison of smectite volume in fracture by exact solution, dots, and pSS solution.

When the source concentration ϕ_i is constant expansion to the steady state radius $r=r_{SS}$ will eventually be reached. It is obtained by solving Equations (8.27) and (8.30) for steady state. The solution is

$$r_{RSS} = \left(\frac{DQ \pi (\phi_i - \phi_R)}{\phi_R \text{ProductLog} \left(\pi \sqrt{\frac{DQ^2 (\phi_i - \phi_R)^2}{r_i \phi_R^2}} \right)} \right)^2 \quad (8.30)$$

$$DQ = \frac{D \delta_{fr}}{Q_{eq,ri}} \quad (8.31)$$

8.2 Including a changing source term concentration $\phi_i(t)$

We now turn to the rate of movement of the rim and also include a case when the mass in the source is depleted by the loss into the fracture and ϕ_i changes slowly with time. Then the above equations are not valid anymore. However, when the rate of change of ϕ_i is slow compared to the rate of advancement of the front an approximate solution can be derived, again invoking the PSS approximation. Conceptually this is done by solving the equation for the rate of mass intrusion in the fracture for $\phi_i(t=0)$ at time zero for a short time interval Δt . Then the loss in the source is calculated and $\phi_i(\Delta t)$ is determined at time Δt . Then another time step Δt is taken using $\phi_i(\Delta t)$ at the inlet for the new time step giving the results at $2\Delta t$. This is repeated until the desired time is reached. Computation wise the procedure can be done by integration as shown below.

The mass that accumulates in the fracture is the difference between what diffuses in and what is lost at the rim.

$$\frac{1}{\rho_s} \frac{dM_s}{dt} = -2\pi \delta_{fr} r_i D \left. \frac{d\phi}{dr} \right|_{r=r_i} - \phi_R Q_{eq} \quad (8.32)$$

Accounting for the change over time of ϕ_i the left hand side of (8.32) can be written

$$\frac{1}{\rho_s} \frac{dM_s}{dt} = \frac{1}{\rho_s} \left(\frac{dM_s}{dr_R} \frac{dr_R}{dt} + \frac{dM_s}{d\phi_i} \frac{d\phi_i}{dt} \right) \quad (8.33)$$

When the change of the ϕ_i in the source over time is determined by the rate of depletion of the mass in the source volume V_{source} by loss into the fracture

$$V_{source} \frac{d\phi_i}{dt} = 2\pi \delta_{fr} r_i D \left. \frac{d\phi}{dr} \right|_{r=r_i} \quad (8.34)$$

When the smectite expands radially outward from a source inside a cylinder Q_{eq} increases with the distance to the rim because the contact area between the seeping water and the gel/sol at the rim increases with the increasing circumference of the rim, see Chapter 7.

$$Q_{eq}^{r_R} = Q_{eq}^{r_i} \sqrt{r_R/r_i} \quad (8.35)$$

$Q_{eq}^{r_i}$ is the equivalent flowrate for radius $r = r_i$.

The differential equations (8.33) and (8.34) containing $\frac{dr_R}{dt}$ and $\frac{d\phi_i}{dt}$ can be integrated numerically to give the rate of change of radius to the rim, the mass in the fracture, the loss from the source and the loss at the rim as functions of time. The initial conditions are $r_R = r_o$ and $\phi_i = \phi_{i,o}$ at time zero.

8.3 Some illustrative examples

8.3.1 Cylindrical expansion

The data used in the examples are chosen to be representative of the conditions in a KBS-3 repository hole with bentonite and the range of expected groundwater salinities.

Figure 8-4 shows steady state radius r_{RSS} for $r_i=0.875$ as function of DQ for $\frac{\phi_R}{\phi_i} = 0.005, 0.01$ and 0.02 . It is seen that for high equivalent flowrates, small DQ 's, the steady state radius to the rim r_{RSS} approaches the source radius r_i .

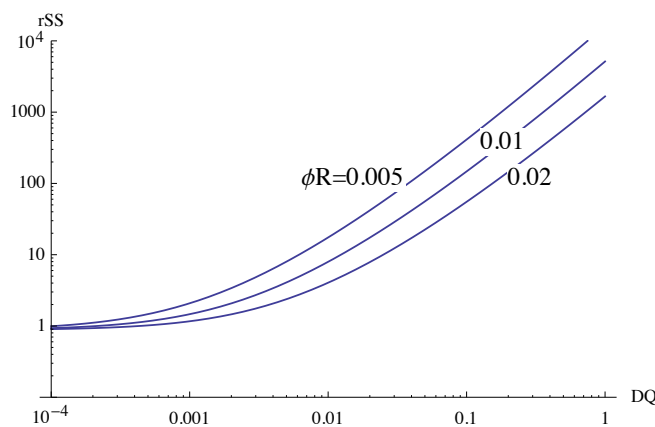


Figure 8-4. Steady state radius for $r_i=0.875$ m, as function of DQ for different ϕ_R .

In Chapter 7 we derived a method to calculate the loss at the rim for different chemical conditions expressed as the equivalent flowrate Q_{eq} . It was found that the larger the radius r_R becomes the larger Q_{eq} will be. This relation is shown in Equation (8.35). It is therefore convenient to relate Q_{eq} at the rim $Q_{eq}^{r_R}$ to $Q_{eq}^{r_i}$ at the inner radius r_i . Figure 8-5 shows the equivalent flowrate $Q_{eq}^{r_i}$ for a radius 0.875 m and aperture 1 mm as function of water velocity for three different monovalent ion concentrations, 0.1, 1 and 10 mM with the Q_{eq} -function taken from Table 7.1.

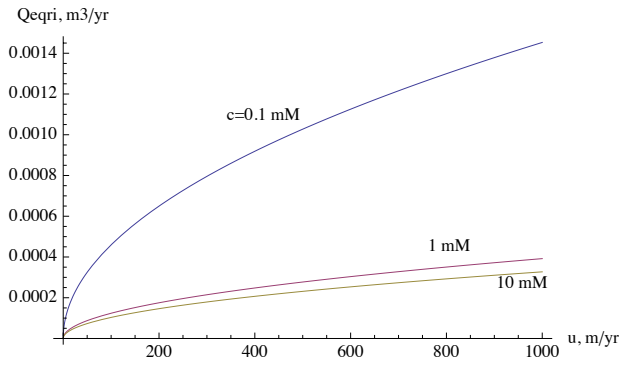


Figure 8-5. $Q_{eq}^{r_i}$ for radius $r_i = 0.875$ m as function of water velocity for three different monovalent ion concentrations, 0.1, 1 and 10 mM taken from Table 7.1.

The equivalent flowrate $Q_{eq}^{r_i}$ for radius $r_i = 0.875$ m is at most 0.0015 m^3/yr even in very dilute water and very high water velocities. For ion concentration 1 and 10 mM, $Q_{eq}^{r_i}$ is lower by about a factor three to four.

Figure 8-6 shows rate of expansion of the rim for $D = 10^{-9}$ m^2/s for different, $Q_{eq}^{r_i}$, for $\phi_i = 0.5$ and $\phi_R = 0.01$. ϕ_i is constant and the source is not depleted in this case.

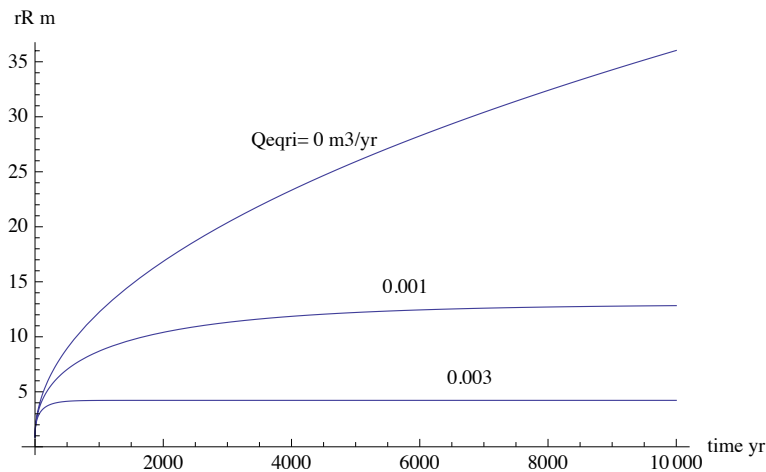


Figure 8-6. Rate of expansion of the radius r_R of the rim for $D = 10^{-9}$ m^2/s for different, $Q_{eq}^{r_i}$ and constant $\phi_i = 0.5$ and $\phi_R = 0.01$.

Figure 8-7 shows mass of smectite in the fracture for $D = 10^{-9}$ m^2/s for different, $Q_{eq}^{r_i}$ and constant source $\phi_i = 0.5$ and $\phi_R = 0.01$.

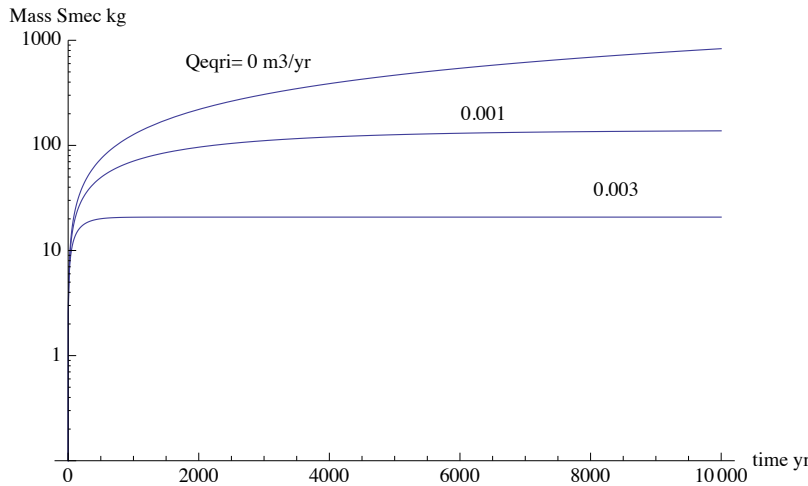


Figure 8-7. Mass of smectite in the fracture for $D=10^{-9} \text{ m}^2/\text{s}$ for different Q_{eq}^{ri} and constant $\phi_i = 0.5$ and $\phi_R = 0.01$.

In figures 8-6 and 8-7 it was assumed that there was an infinite mass of smectite in the source. In the next figures the source is taken to have a bentonite volume equal to the volume in a deposition hole, which is about 15 m^3 and the initial smectite volume fraction in the source is $\phi_{io} = 0.5$. It is further assumed that as there is loss of smectite in the deposition hole the smectite in the hole expands fully to even out the volume fraction in the deposition hole.

Figure 8-8 shows the mass of smectite mass that has been lost from the source over time for Q_{eq}^{ri} ranging from 0.3×10^{-3} to $10 \times 10^{-3} \text{ m}^3/\text{yr}$. For radial expansion the rate of loss decreases slowly with time and mass in the fracture increases nearly proportionally to time.

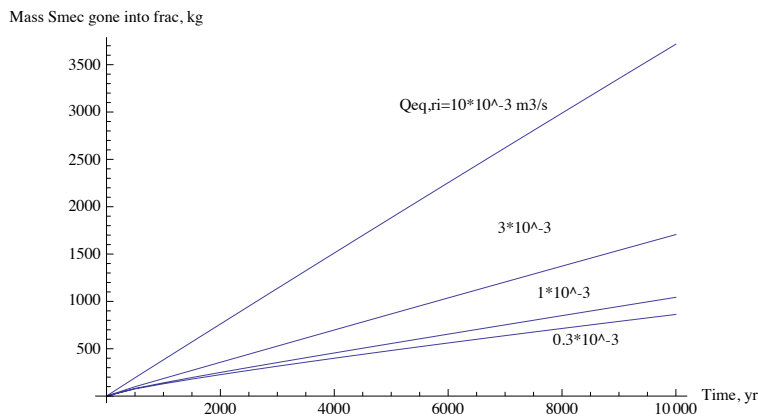


Figure 8-8. Mass of smectite that has been lost from the source over time for $Q_{eq}^{ri} = 0.3 \times 10^{-3}$ to $10 \times 10^{-3} \text{ m}^3/\text{yr}$.

For $Q_{eq} 3 \times 10^{-3} \text{ m}^3/\text{yr}$ about half the loss is to the seeping water at the rim and half by what still resides in the fracture. For Q_{eq} less than $0.3 \times 10^{-3} \text{ m}^3/\text{yr}$ practically all the loss resides in the fracture.

Should the equivalent flowrate be extremely high, $0.003 \text{ m}^3/\text{yr}$, see Figure 8-6, the mass loss is entirely dominated by that lost to the water. The largest expansion of the radius to the rim is

then slightly less than 4 m, the total mass lost is 1 700 kg and ϕ_i has dropped about 8 % to 0.46 after 10 000 years.

Figure 8-9 shows the radius to the rim as function of time for $Q_{eq} 1 \times 10^{-3}$ and $3 \times 10^{-3} \text{ m}^3/\text{yr}$. For the lower flowrate the distance to the rim increases to about 11.5 m at most after about 5000 years where after it slowly decreases again as the volume fraction in the source slowly drops. For the higher flowrate the maximum extent, just less than 4 m is reached after about 400 years.

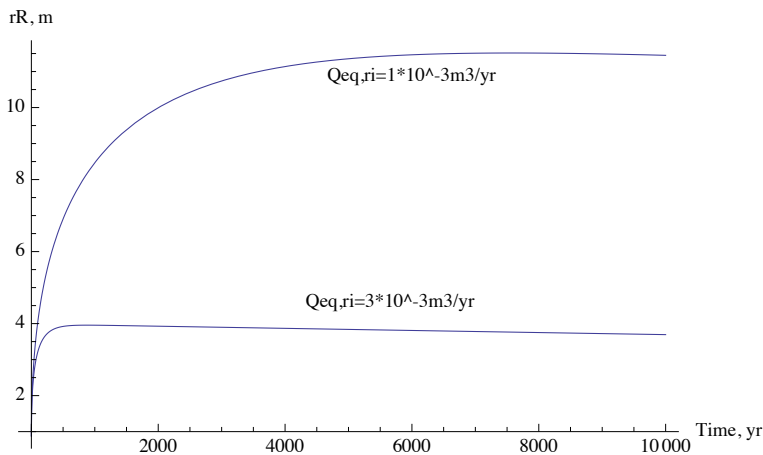


Figure 8-9. Radius to the rim as function of time for $Q_{eq}^r = 1 \times 10^{-3}$ and $3 \times 10^{-3} \text{ m}^3/\text{yr}$. Source is being depleted.

8.4 Some comments on the PSS model

The PSS model uses several assumptions and approximations. One is that the expanding gel does not flow for the hydraulic gradients expected until the volume fraction has dropped to low values in the range $\phi_R = 0.005$ to slightly more than 0.01. This is supported by experiments and by theoretical considerations described in Chapters 6 and 7. A further approximation is that radial *flow* velocity of gel in the rim zone can be neglected when modelling the processes in the rim zone. This was shown to give an error of about 6 % in a sample calculation described in section 7.6. The rim zone model is the most important component of the two-stage model described here because it accurately describes what happens in the rim zone, the region where our previous finite element modelling was found to give results, which were suspected to contain considerable errors. This led to considerable overestimates of the loss to the seeping water. At the same time the loss by accumulation in the fracture was hidden.

Another simplification is that the gel expansion can be modelled as a diffusion process with a constant diffusion coefficient. This is further supported by the sharp drop in the diffusion coefficient when the volume fraction decreases. The drop occurs at lower and lower volume fractions as the ion concentration decreases and is a fair approximation for ion concentrations below 1 mM. The sharp drop can be seen in Figure 3-1. Note that the figure used a double logarithmic scale.

A further approximation is that the gel expansion is modelled as being a pseudo state process and that the steady state profile for radial expansion always can be used to account for both the mass in the fracture and the gradient at the source. The error using this approximation was found to be about 13 % for the rate of intrusion and it decreases to zero as steady state of the expanding front is approached.

A simple error estimate of the PSS approximation for a slowly changing source concentration ϕ_i can be made in the following way. 1) Solve the equations for constant original ϕ_{i0} at time t . This gives mass loss for constant ϕ_{i0} . Solve Equations, which account for a changing ϕ_i (8.33) and (8.34) and find ϕ_i at the final time accounting for the changing ϕ_i by use of the PSS approximation. This gives $\phi_{i,end}$ at the end of the time considered. Then solve the equations for the just obtained lower $\phi_{i,end}$ for a constant source term. Compare the loss obtained by the PSS case with the mean of the two cases based on constant source concentration. If the PSS solution gives a value fairly close to the mean of the other solutions the error probably can be accepted.

The examples presented suggest that the loss to the seeping low ionic strength water is considerably smaller than in our previous modelling Moreno et al (2009). On the other hand it shows that there is no need for the approaching water to have very low salinity for a considerable loss of smectite to occur because the gel expands into the fracture even in waters that have much higher salinity. Then negligible loss to the seeping water will occur but more and more smectite will move into and accumulate in the fracture. This is not limited to the periods when low ionic strength water intrudes the repository. The expansion can in principle go on “forever” and start as soon as the repository has become resaturated with water.

It is acknowledged that there may be and probably are other sources of error than those, which have been identified and assessed. Nevertheless, the detailed analysis of the different processes and mechanisms that have been undertaken have shed light on areas that must be better explored if more accurate modelling is to be undertaken.

9 Discussion

9.1 General

The two-stage model has some advantages over the fully coupled model, which solves the equations for expansion of the gel and the flow in the rim simultaneously. The latter is in principle more correct but not always easy to implement correctly as the strong non-linearities give rise to very long computing times and computations sometimes fail. Problems were often encountered for low water velocities. Methods based on finite elements or similar approximations that discretise space have inherent difficulties in handling extremely sharp fronts and jumps in parameter values such as a change from zero velocity to a finite velocity. The two-stage model separates the processes in the rim with flow and diffusion from the region with the expanding gel where there is no flow of gel. A high-resolution technique can then be used to solve the conditions in the rim. The two relations are later re-coupled by matching them at the rim border. One additional advantage of the two-stage model is that it highlights how different mechanisms interact and helps to gain insights into the interaction of the different processes in the different regions.

The assumptions and approximations in the two-stage model have been subjected to a number of tests, which have shown that the errors introduced are not grave. The two-stage model predicts more than a factor 5 smaller loss to the seeping water for the highest water velocity. The bentonite is predicted to expand considerably further into the fracture by the two-stage model. The different tests performed show that the two-stage model gives the more correct results.

The examples presented show that the loss of smectite from a deposition hole with a nuclear waste canister of the KBS-3 design can be considerable over a 10 000 year period even when there is no or negligible loss to the seeping water at the rim. This is because of the continuous expansion of smectite into the fracture even when there is no loss at the rim. It was found that this expansion takes place even when ion concentrations in the pore water of the bentonite is much higher than that of dilute melt-water during an ice age, which has previously been considered a prerequisite to loose much smectite. The rate of loss of smectite with 0.1 mM and 10 mM, or even higher ion concentration during the expansion phase differs only by on the order of a few tens of % (Fig 5-8). In 10 000 years some 1000 kg of smectite would expand into a 1 mm aperture fracture also at the higher ionic strength and with no erosion at the rim. With erosion in the rim the rate of loss will be larger. The expansion into the fracture would start already when the bentonite and the rock fractures have become saturated with water after closing of the repository.

Some of the assumptions underlying the examples above may be exaggerated. 1 mm aperture fractures with a radius larger than 60 m in diameter, the size of fracture filled with smectite after 10 000 years, is not likely to exist or at least not be allowed to intersect a deposition hole. A network of 0.1 mm aperture fractures would be less unrealistic. A network will do as well as a single fracture for the clay intrusion. On the other hand, as the expansion is practically independent of water flow and not much influenced by the ionic strength of the pore water the intrusion into the fracture network will continue for longer times than that in the example, albeit slowing down gradually.

9.2 Implications for long term stability of buffer and impact on solute transport to and from canister

It should be borne in mind that there are a number of observation that show that there are other mechanisms than those described above that cause erosion of smectite. In Neretnieks et al. (2009) some experiments are described that show that gel/sol subject to gravity can sediment rapidly, hours to days, through narrow passages such as a fine net or a semi vertical fracture. The same phenomenon was described by Schatz et al. (2012) This process seems to be more rapid than what the models discussed above suggest.

Furthermore, the models above do not consider how the presence of the detritus material, always present in natural bentonites with 20 % or more, influences the expansion of the gel in natural fractures. Such fractures have variable aperture and it is likely that the detritus material, essentially very fine sand, will get stuck in the narrow passages in the fractures, gradually building up barriers with fine pores in which the smectite particles cannot wriggle though. Experiments have shown that one or a few mm thick layers of detritus stop the passage of smectite particles, Richards and Neretnieks (2009).

A different and positive aspect is that even a small intrusion distance, e.g. 1 m will considerably add to the resistance for solutes that migrate between the seeping water and the interior of the deposition hole. This can be seen from Equation (3-6) applied to a solute and recognising that the equivalent flowrate for a solute $Q_{eq,sol,diff}$ by diffusion through the smectite residing in the fracture is

$$Q_{eq,sol,diff} = \frac{N_{sol}}{c_{sol,out} - c_{sol,i}} = \frac{2\pi\delta_{frac}}{\ln(r_{out}/r_i)} D_{sol} \quad (9-1)$$

With the same aperture, 1 mm, as in previous examples and $D_{sol}=10^{-9}$ m²/s, a typical value for a small solute, $Q_{eq,sol,diff}=8.2\times 10^{-12}$ m³/s, which is 0.26 litres/year. A 10 m intrusion of gel gives $Q_{eq,sol,diff}=0.079$ litres/year. These values are much lower than the $Q_{eq,sol,flow}$ that would be able to carry the solutes by the seeping water in fractures with the higher fracture flowrates expected. The diffusion resistance in the gel in the fracture would dominate and considerably limit the solute transport to and from the canister to the very low values above. The intrusion of smectite into fractures can therefore be very beneficial to protect the canister from corrosive agent and would also considerably impede the escape of nuclides from a damaged canister.

10 Conclusions and outlook

The modelling described in this report suggests that if expansion of smectite clay into fractures were not impeded by the detritus material in bentonites considerable amounts of clay can intrude into the fracture and thus decrease the amount of buffer in a deposition hole if this is intersected by a large aperture (1 mm) fracture or a network of fractures with large apertures. Over a 10 000 year period some up to 1000 kg could be lost from the deposition hole just by the intrusion into the fracture. This happens at ionic concentrations up to at least 10 mM in the pore water and the process starts early. The intrusion depth could reach some 60 m after 10 000 years. The gel in the fractures will act as a very strong diffusion barrier for solutes migrating to and from the canister and have beneficial effects in both large and small fractures.

The potential effect of large amounts of detritus material in bentonite clay has not been investigated but is expected to slow down or even stop further smectite loss by forming filters in the variable aperture fractures as the particles increasingly become stuck in locations where the aperture is smaller than the particles and gradually fill also larger voids to form filters. Such filtering is also expected to hinder the loss of smectite by the observed but not understood rapid sedimentation of smectite aggregates. The authors suggest that the understanding of the migration and fate of the detritus material may be the most important process that may limit the loss of smectite from a deposition hole.

11 References

SKB reports can be freely downloaded from: <http://www.skb.se>

*Posiva reports can be freely downloaded from:
http://www.posiva.fi/en/databank/working_reports*

Bird, R.B., Stewart, W.E., Lightfoot, E.N., 2002. Transport Phenomena, second ed. John Wiley-Sons, Inc.

Birgersson M., Börgesson L., Hedström M., Karnland O., Nilsson U., 2009, Bentonite erosion. Final report, Swedish Nuclear Fuel and Waste management Co, Technical report, SKB TR-09-34

Chambré P L, Pigford T H, Fujita A, Kanki T, Kobayashi A, Lung H, Ting D, Sato Y, Zavoshy S J, 1982. Analytical performance models for geologic repositories. LBL-UCB-NE-4017, UC70. Earth Sciences Division, Lawrence Berkeley Laboratory and Department of Nuclear Engineering, University of California, Berkeley, California, 94720 USA. Report prepared for the U.S. Department of Energy.

Crank J., 1975, The mathematics of diffusion, Oxford science publications, 2nd ed.

Carslaw H.S., Jaeger J.C., 1959, Conduction of heat in solids, 2nd ed., Oxford Clarendon press

Liu, L., 2010. Permeability and expansibility of sodium bentonite in dilute solutions. Colloids Surf. A: Physicochem. Eng. Aspects 358 (1–3), 68–78.

Liu L., 2011, A model for the viscosity of dilute smectite gels, Physics and chemistry of the earth, 36, p 1792-1798

Liu L., 2013, Prediction of swelling pressures of different types of bentonite in dilute solutions, Colloids and Surfaces A: Physicochem. Eng. Aspects 434 (2013) 303– 318

Liu, L., Moreno, L., Neretnieks, I., 2009a. A Dynamic force balance model for colloidal expansion and its DLVO-based application. Langmuir 25 (2), 679–687.

Liu, L., Moreno, L., Neretnieks, I., 2009b. A novel approach to determine the critical coagulation concentration of a colloidal dispersion with plate-like particles. Langmuir 25 (2), 688–697.

Liu L., Neretnieks I., Moreno L., 2011, Permeability and expandability of natural bentonite MX-80 in distilled water. Physics and Chemistry of the Earth, 36, p 1783-1791

Moreno L., Neretnieks I., Liu L., 2010, modelling of bentonite erosion TR10-64.

Moreno L., Neretnieks I., Liu L., 2011, Erosion of sodium bentonite by flow and colloid diffusion, Physics and chemistry of the earth, 36, p 1600-1606

Neretnieks, I., Liu, L., Moreno, L., 2009. Mechanisms and Models for Bentonite Erosion. Swedish Nuclear Fuel and Waste management Co., Technical report, SKB TR-09-35

Neretnieks I., Liu L., Moreno, L., 2010, Mass transfer between waste canister and water seeping in rock fractures. Revisiting the Q-equivalent model, Swedish Nuclear Fuel and Waste management Co., Technical report, SKB TR-10-42

Richards T., Neretnieks I., 2010, Filtering of clay colloids in bentonite detritus material. Chem. Eng. Technol., 33, No 8, 1303-1310

Schatz, T., Kanerva, N., Martikainen, J., Sane, P., Olin, M., Seppälä, A and Koskinen, K., 2012, Buffer Erosion in Dilute Groundwater. Posiva Report 2012-44 (2012).

Deliverable 5.2 „Progress report of model validation and model development“

KIT-INE contribution

Summary

KIT-INE will focus on the effect of natural fracture geometry on bentonite erosion and bentonite colloid transport. In detail, the work concentrates on the following:

1) Bentonite erosion rates

3D computational fluid dynamics (CFD) simulations (using the finite volume code Ansys Fluent) on 2 natural single fractured drill cores from Äspö, Sweden will be conducted. Both cores are characterized by μ -computed tomography (μ CT) to obtain geometrical information on the fracture geometry and aperture distribution. The fracture geometry is used directly to generate a computational mesh for the 3D CFD simulations. Flow field calculations are varied as a function flow velocity to cover a range of natural occurring flow velocities in fractured ground water environments. Subsequently, the derived flow fields are used to calculate bentonite erosion rates using the approach presented in Moreno et al. (SKB, 2010).

2) Coupling of the KTH erosion model to the KIT-INE 3D CFD fracture models

The bentonite erosion model by Neretnieks et al. (SKB, 2009) is currently implemented in 2D in the finite element code COMSOL Multiphysics both by KTH and, in a slightly simplified way, by VTT. It is planned to couple the erosion model (first starting with the VTT model) to the 3D fracture models mentioned under 1). For this, the 3D fracture model needs to be implemented in COMSOL to be coupled to the available bentonite erosion model.

3) Bentonite colloid transport modelling

To examine the bentonite colloid transport, a flow cell with an artificial fracture in a granodiorite core from Grimsel, Switzerland is produced. This flow cell is used in experiments to study the bentonite colloid migration as a function of aperture and flow velocity under unfavorable colloid attachment conditions. Experimentally obtained breakthrough curves will be modeled using the Discrete Phase Model module within Ansys Fluent.

Status of work being performed by KIT-INE

Impact of fracture heterogeneity on bentonite erosion rates:

Introduction

So far, the influence of fracture geometry on bentonite erosion has only been paid little attention. Both experimental and numerical investigations focused on simplified parallel plate setups mainly due to e.g. lack of detailed digital data on 3D fracture geometry, computational limitations of extensive 3D models or the considerably higher technical burden in reproducing artificial rough fractures for experimental investigations. It is well known that heterogeneous flow fields evolve in natural fractures due to the complex geometry leading to flow features like channeling and/or stagnant flow areas (Neretnieks et al., 1982; Tsang et al., 1988). These fracture characteristics will impact the swelling and erosion behavior of the bentonite as well as the flow field. The variability of the flow velocities may cause the bentonite to swell and erode not homogeneously but as a function of the flow velocity distribution in the direct vicinity of the bentonite. Thus parts of the bentonite may be influenced by rather high velocities and in consequence are prone to significantly higher erosion rates than other parts in areas of e.g. low or even stagnant flow conditions. In model calculations on bentonite erosion (rates) using simplified geometries this issue is implicitly not accounted for. The aim of the work by KIT-INE within BELBaR work package 5 is to shed light on the influence of flow heterogeneity in natural fractures on the bentonite erosion and derive distributions (and the variability) of bentonite erosion rates as a function of flow rates covering a range of natural specific discharges representative of crystalline ground water environments.

1) Bentonite erosion rates

Two overcored natural single fractures which have been characterized by means of μ -computed tomography (μ CT) to obtain parameters like e.g. total porosity and aperture distribution are available at KIT-INE. Moreover, the μ CT data deliver detailed information on the natural fracture geometry. Figure 1 shows both drill cores as installed in the laboratory. Based on the digital μ CT information, 3D numerical meshes have been produced after segmentation of the μ CT to separate the void space (connected porosity = fracture) from the solid material (rock) data based on threshold segmentation. More information on the general segmentation and meshing procedure of the digital dataset to obtain the numerical grids is described in (Huber et al., 2012). A schematically flow chart of the procedure applied is depicted in Figure 2.



Figure 1: 2 single fractured drill cores from Äspö, Sweden. (Left) Core#8 (Right) Core#2.2. Note that Core#8 has a length of 13.05 cm and a diameter of ~5.05 cm whereas the spatial dimensions of Core#2.2 are ~4.2 cm in length and ~4.8 cm in diameter.

The most sophisticated model on bentonite erosion is presented by Neretnieks et al (SKB, 2009). Moreno et al. (SKB, 2010) used the model for both rectangular geometry and a more realistic cylindrical geometry of the deposition hole. A simplified equation based only on the parameters flow velocity and fracture aperture can be derived for both cases. The erosion rate $R_{Erosion}$ for the latter is given as (Eq. 1):

$$R_{Erosion} = A \cdot \delta \cdot v^{0.41}$$

where v is the flow velocity [m/yr], δ is the aperture [m] and the constant $A = 27.2$.

The work in hand aims in coupling this simplified approach of calculating bentonite erosion rates to the complex flow velocity distributions obtained by CFD simulations and the aperture distributions based on the μ CT characterization for both natural fractured drill cores. The following variations of the parameters aperture distributions and flow velocity distributions have been realized:

- Case A: Only the mean flow velocity and the mean aperture derived from the complete 3D datasets is used,
- Case B: The complete 3D flow velocity distribution and the mean aperture is used,
- Case C: The mean flow velocity and the complete 3D aperture distribution is used.

All three cases are realized for both drill cores available and for a range of specific discharges, namely, 0.315, 3.15, 31.5 and 315 m/yr (according to Moreno et al. (SKB, 2010)).

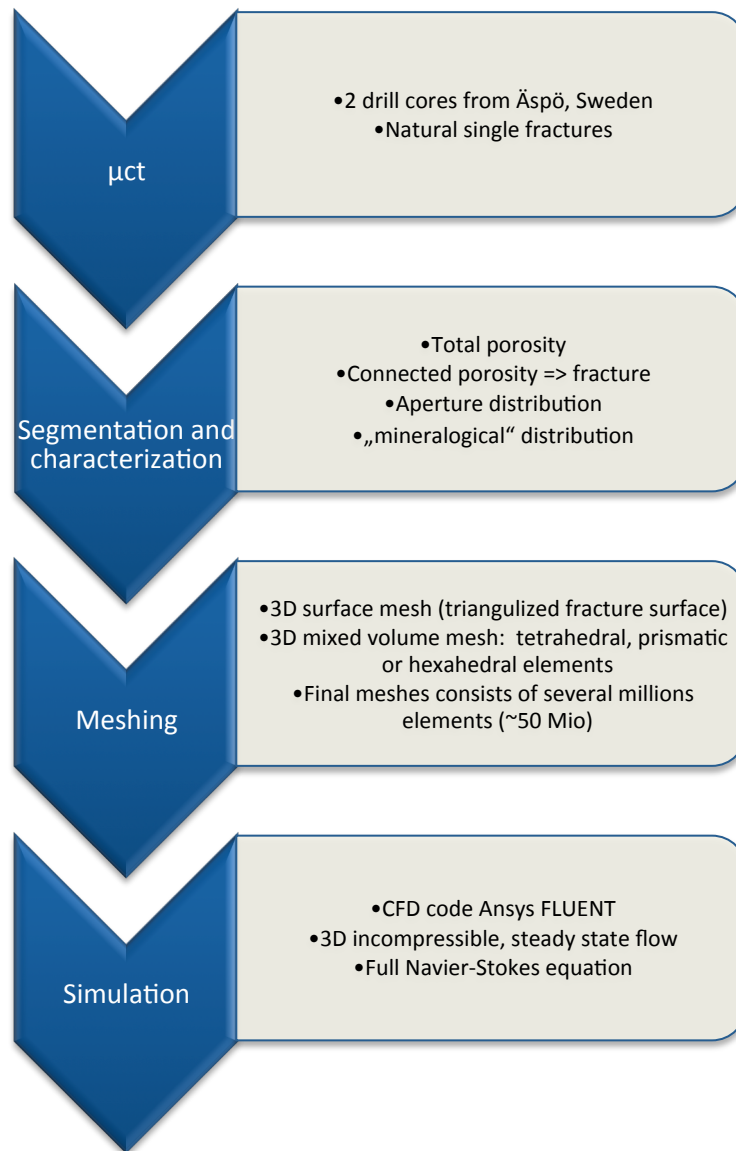


Figure 2: Flow chart of the modeling procedure.

Aperture distributions

Figure 3 shows a rendered visualization of the fracture surfaces colored by the apertures. It can be seen, that the apertures are heterogeneously distributed over the fracture as a consequence of the complex natural fracture geometry. Moreover, areas where both fracture surfaces touch each other (so called asperities) occur, resulting in aperture values of zero. On basis of the μ CT dataset of both cores, the aperture distributions were determined. For this, the mid-plane between the fracture surfaces was calculated automatically by the CAD and meshing software tools used (Mimics Innovation Suite, Materialise) and afterwards the distance from the mid-plane to the fracture surfaces was calculated yielding the aperture distribution. Since this calculation depends on the triangulation of the surface meshes, a very fine surface mesh (> 1 mio. Elements; the nodes were used to extract the apertures (~300k)) was used to guarantee a high resolution of aperture values. The resulting aperture distributions for both cores are shown in Figure 4.

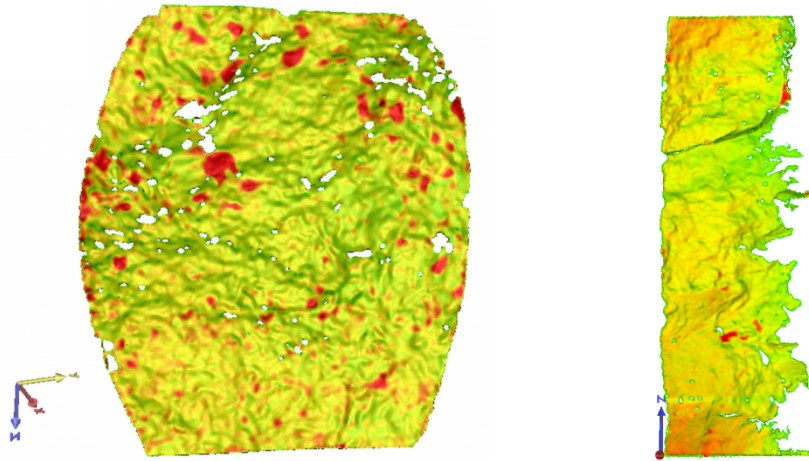


Figure 3: Rendered visualization of the fracture surface geometry for Core#2.2 (left) and Core#8 (right). Colors represent the apertures (green: low aperture, yellow: mean apertures and red: high apertures). Note that the color scales is different for both fractures. Quantitative information on the aperture distributions is given in Figure 4.

A distinct difference in both cores is noticed in terms of the absolute aperture values. Core#8 exhibits higher apertures than Core#2.2 with a maximum aperture of ~ 1.53 mm whereas Core#2.2 has a maximum aperture of only ~ 0.81 mm. The difference is furthermore documented in the mean aperture of both cores. While Core#8 has a mean aperture of ~ 0.45 mm, Core#2.2 only yields a value of only ~ 0.192 mm. Thus the fracture of Core#2.2 is narrower than the fracture of Core#8. Another difference concerns the distribution. While Core#2.2 nicely follows a log-normal aperture distribution, Core#8 does not (Figure 4). A log-normal distribution is often found in natural fractures (Adler and Thovert, 1999). The distribution of Core#8 is skewed to lower aperture values which is also visible in the higher variance compared to Core#2.2 This effect may likely be attributed to the heterogeneous right fracture side.

Velocity distributions

Figure 4 shows the velocity magnitude distributions for both cores (for different flow rates). The distribution shown for Core#2.2 serves only an illustrative purpose since the flow rate is much higher than the ones applied in this study to investigate erosion modelling. The velocity distribution shown for Core#8 corresponds to the mean flow rate of 3.15 m/yr. The shapes of the histograms both show a rather broad single peak with some minor shoulders for higher velocities. Since the aperture distribution of Core#2.2 is more homogeneous, the velocity distribution is also smoother and more regular. In contrast Core#8 shows a slightly more heterogeneous distribution.

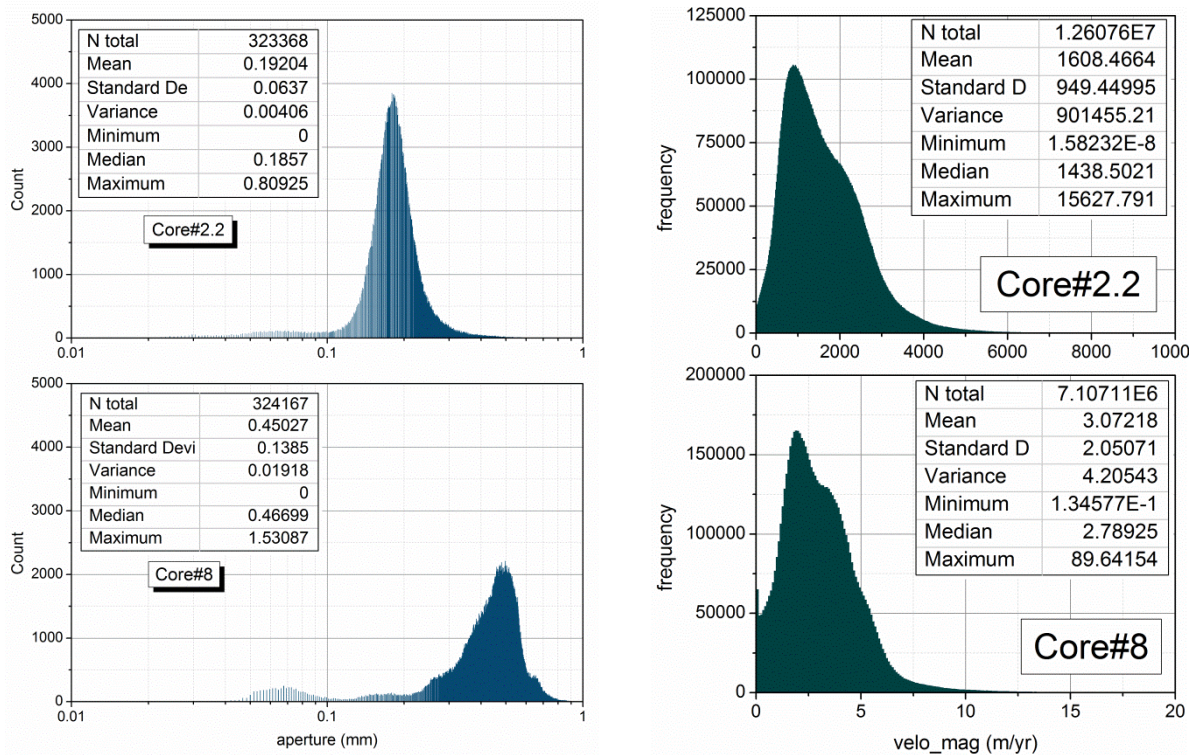


Figure 4: Aperture distributions for both cores. (Upper left) Core#2.2 (Lower left) Core#8. Velocity magnitude distributions for both cores. (Upper right) Core#2.2 (Lower right) Core#8. Note that the imposed flow rates are different for both cores.

Calculation of bentonite erosion rates

Results are presented only for one core (Core#8). The flow simulations for core#2.2 are in progress at the moment.

Case A

The mean aperture of Core#8 is 0.4503 mm as derived from the μ CT data. The mean erosion rates determined using the mean values for the aperture and the velocity for the respective specific discharges imposed are depicted in Figure 5 in comparison to the values given by Moreno et al. (SKB, 2010) for the cylindrical symmetry and an aperture of 1 mm. In general, our erosion rates calculated for Case A are always lower than the ones given by Moreno et al. (2010) which is expected due to the higher aperture of 1 mm used in the 2D simulations.

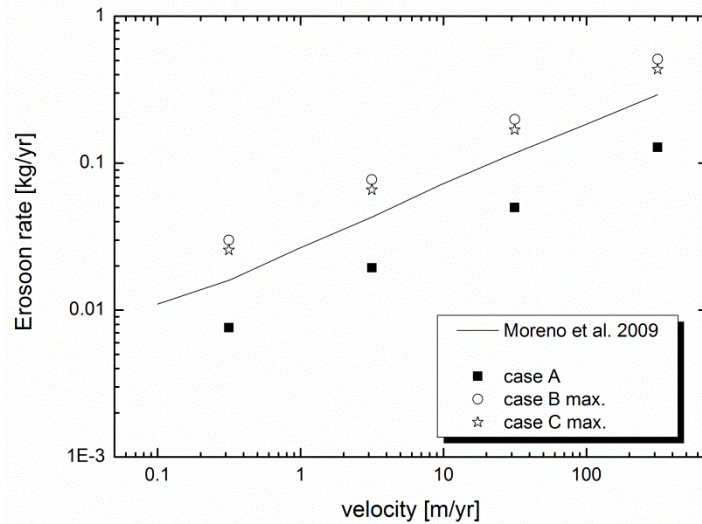
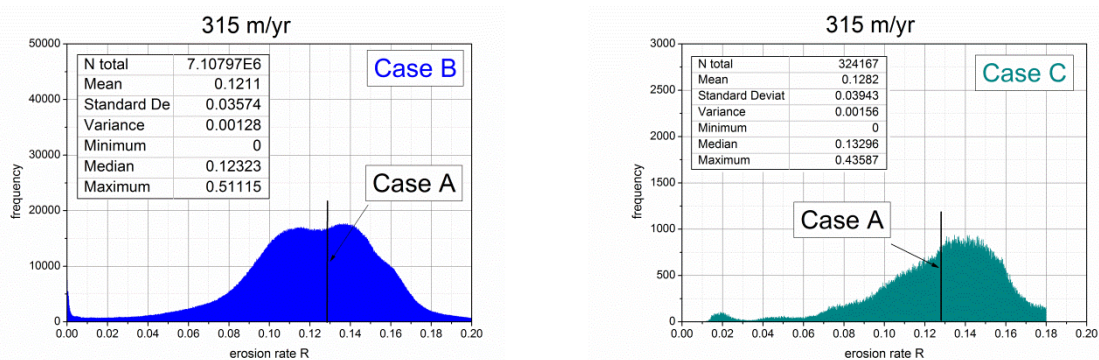


Figure 5: Comparison of bentonite erosion rates calculated in this study and the erosion rates for a 1 mm aperture given by Moreno et al. (2010).

Case B and C

Figure 6 depicts histograms for the erosion rates determined in this study for Case B and Case C, respectively for 4 different flow rates. Additionally inserted in the figures, statistics on the results are given. So far, only results for Core#8 are available. The simulations for Core#2.2 are processed at the moment. Due to the complex flow velocity distribution in the fracture the erosion rate distributions are also quite complex. Since either the 3D velocity or aperture distributions have been used in calculating the erosion rates in Case B and C, the shape of the histograms follow the shape of these distributions. In general, the results reflect the variability of erosion rates due to the fracture geometry. The maximum erosion rates for Case B and Case C are higher than the erosion rates given by Moreno et al. (2010). The minimum erosion rates are zero, due to both zero velocities in the flow field (no-slip boundary conditions at the fracture walls) and zero apertures in the aperture distribution.



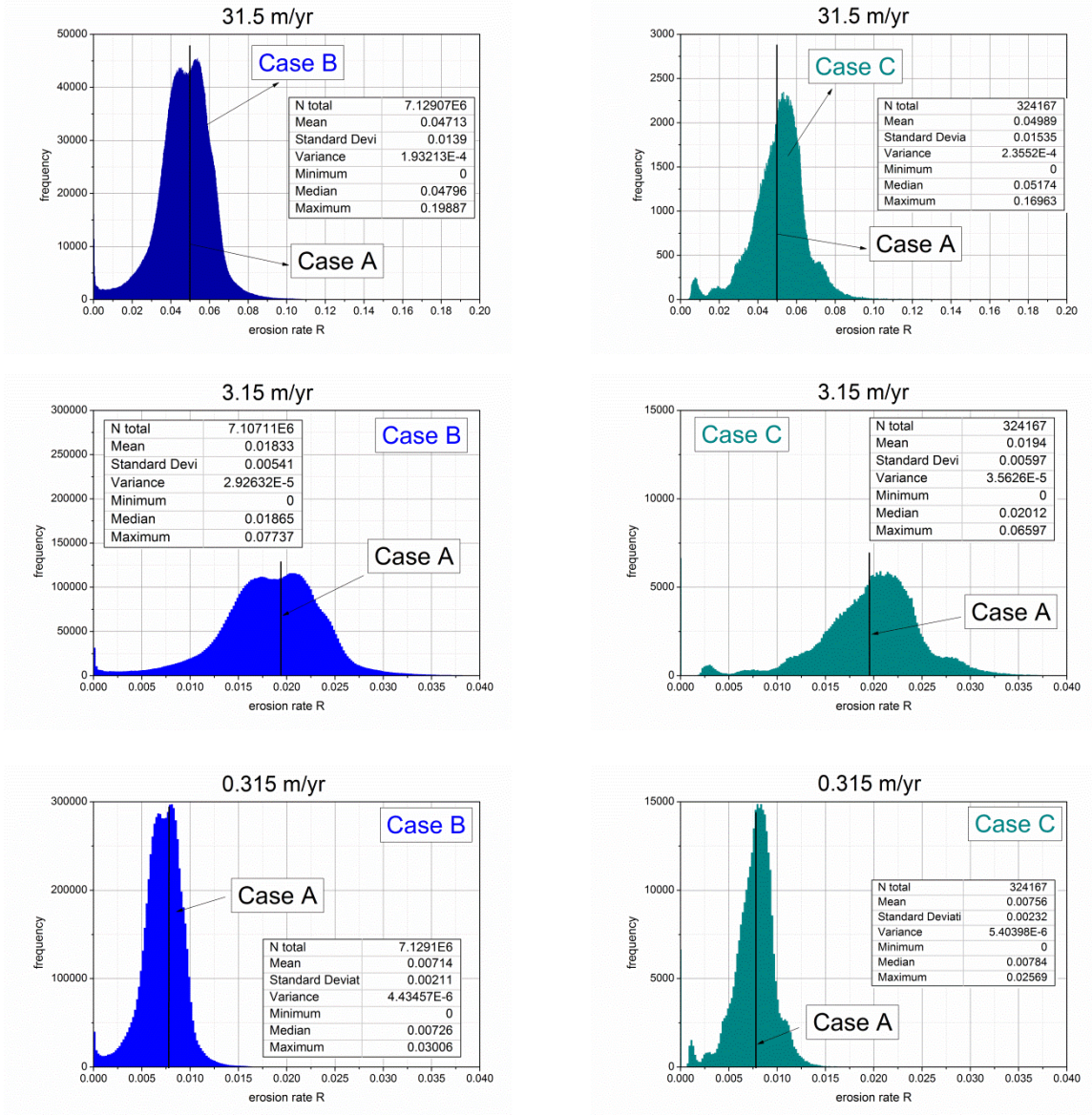


Figure 6: Histograms of erosion rates determined for cases B and C for 4 different flow rates. Note that scales may vary between different velocities. Total number of bins used in every histogram is 1000.

2) Coupling of the KTH erosion model to the KIT-INE 3D CFD fracture models

Neretnieks et al. (SKB, 2009) presented a model for bentonite swelling and erosion which is used and further developed within BELBaR by KTH and VTT. For solving the partial differential equations the model has been implemented in the finite element code COMSOL Multiphysics. Due to the complex mathematics underlying the model, the geometry of the model is simplified at the moment (assumption of a 2D parallel plate model for the treatment of fractures in the vicinity of the bentonite source). To study numerically the effect of fracture heterogeneity on the bentonite erosion, KIT-INE was planning to couple their available 3D natural single fracture flow models to the “KTH” erosion model. The approach foresees the emplacement of virtual clay plugs into the fracture in zones of different flow regimes e.g. high flow or stagnant flow areas. Figure 5 schematically depicts this idea.

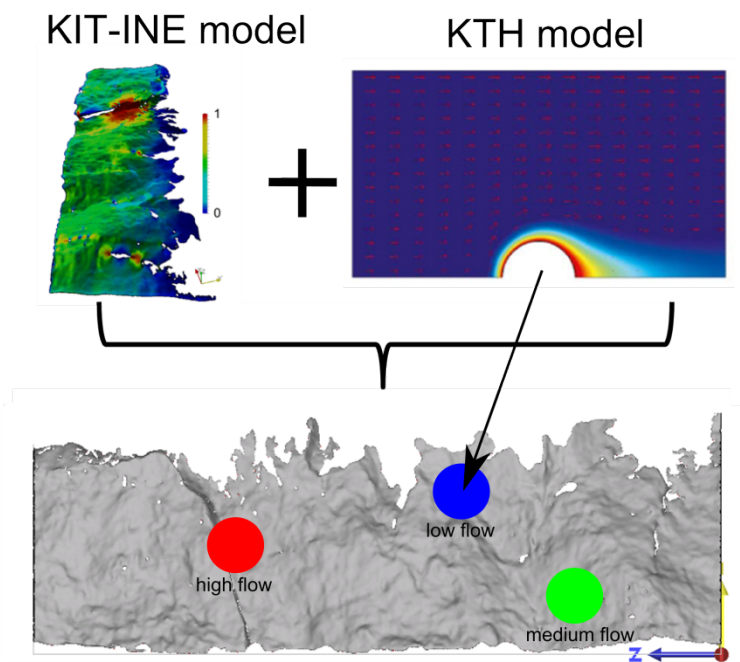


Figure 7: Schematic visualization of the coupling approach.

Therefore, the digital fracture datasets need to be transferred into COMSOL to be coupled to the erosion model. In a first step, this would require the computational meshes to be imported into COMSOL. First test revealed that it is in general possible to import (at least partially) the 3D fracture model into COMSOL and to apply boundary conditions directly to the mesh. This latter feature is finally possible in the actual version of COMSOL (> V4.3). Nevertheless, the size of the numerical mesh (3.7 GB in case of the 50 Mio. element model) poses computational problems in terms of memory handling when e.g. calculating steady state flow in 3D (Stokes equation) only. The erosion model demands transient flow calculation due to the transient interaction between flow and “solute” transport which increases e.g. the complexity of the flow and computational time drastically. The workstation used at the moment by KIT-INE (8 cores, 96 GB RAM) may not be sufficient to solve the 3D model. Tests with different numerical solvers (e.g. direct or iterative solvers) may circumvent these problems. Alternatively, the model may be run on the KIT high performance cluster HC3.

3) Bentonite colloid transport modelling

Bentonite colloid transport is addressed by KIT-INE within BELBaR both in experiments and modelling. For this, the development of a suitable artificial flow cell is in progress. A prototype-like flow cell has been produced and tested (Figure 8) for its feasibility. A natural Grimsel granodiorite matrix core with a diameter of ~4.8 cm has been cut perpendicular to the core length axis to obtain a smaller core with a length of ~5 cm. This core was again cut perpendicular to the length axis to obtain an upper part with a height of around 4 cm and a lower part of around 1 cm. In the upper part holes have been drilled parallel to the length axis approximately 1 cm from the outer rim of the core and ~3 cm distance from each other. These boreholes act as the inlet and outlet of the fracture flow cell. Peek tubing is placed within the inlet and outlet drill holes to prevent any sorption of colloids in this area. Both parts are assembled using Plexiglas rings into which both core parts can be emplaced and fixed with screws to close the cell. Between both parts of the core an O-ring is placed which seals the core to the outside facilitating the flow to take place in the cell. Moreover, the height of the O-ring defines the aperture. By using O-rings with different thicknesses the aperture can be easily varied. The aperture used in this study is 2.7 mm.

The experiments will be carried out using different specific discharges and apertures, respectively. Different bentonite colloid suspensions are foreseen to be used. It is planned for example, to directly couple the flow cell to a bentonite erosion experiment and examine the difference of these freshly eroded “in-situ”-colloids to bentonite colloids obtained by classical bentonite powder suspension and dialysis generation. Bentonite colloid breakthrough curves will be measured and the fracture surface is examined post-mortem to shed light on the spatial deposition pattern and behavior of the colloids.

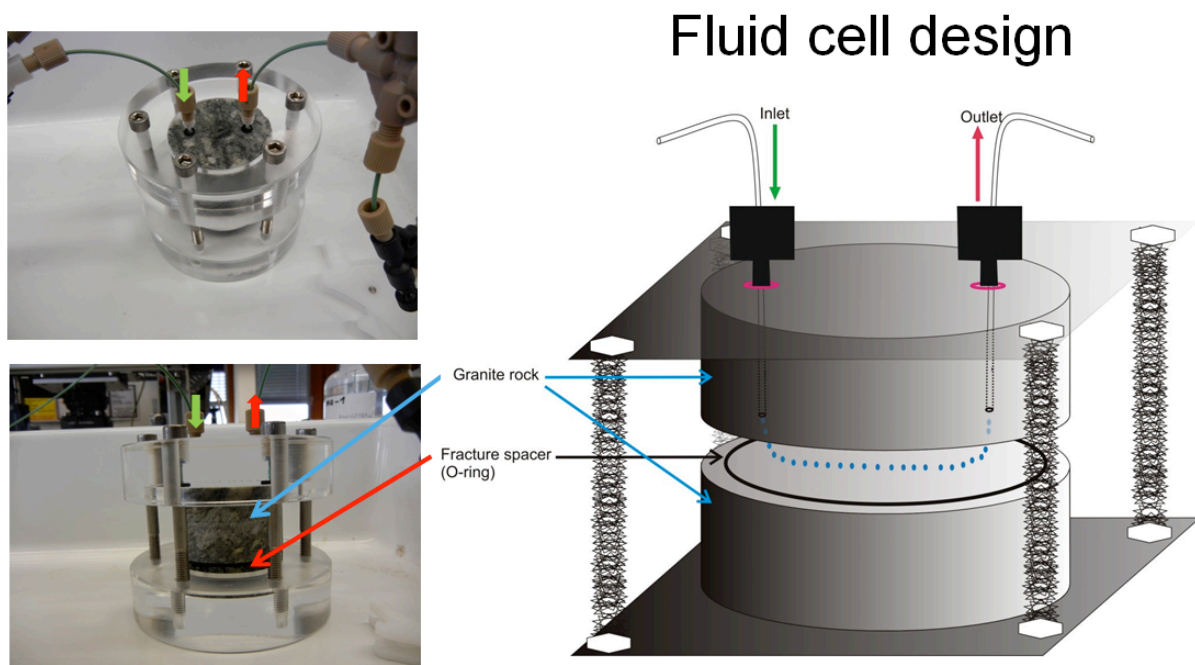


Figure 8: Design of the prototype fluid cell.

Regarding the modelling approach, a 3D model has been prepared of this flow cell prototype as a kind of feasibility study to gain experience in the approach planned (Figure 10). The

modelling will be carried out using the Discrete Phase Model within the CFD code Ansys Fluent which enables the calculation of the dynamics of multiphase flows (e.g. solids or air bubbles and fluid flow). It is based on the Euler-Lagrangian method, which will briefly outlined below. This approach only holds if the volume fraction of the dispersed phase is low ($< 10\%$). For a thorough description of the method and its implementation in the CFD code Fluent the reader is kindly referred to the literature (ANSYS, 2009). The approach used here first solves the Navier-Stokes equations for the fluid flow using the classical continuum approach and tracks the dispersed phase (particles) by a Lagrangian tracking scheme through the fluid field. Only the equations for the Lagrangian Particle Tracking are shown in the Appendix to this chapter whereas the reader is referred to the literature for the Navier-Stokes equations (ANSYS, 2009). The particles (colloids) in the simulations are supposed to exchange no mass or heat with the surrounding fluid and do not influence the flow field. Thus, it is possible to decouple the calculation of the stationary flow field and the transient particle transport. Moreover, no interaction between the particles itself are considered.

The following boundary conditions for the particles when contacting a wall have been applied to model a possible sorption/attachment of the bentonite particles to the fracture surface

- a) Perfect sorption, that is, every hit of a particle leads to irreversible attachment to the surface
- b) No sorption, that is, particles are reflected at the wall
- c) Different attachment probabilities (collision efficiencies α) will be applied to the fracture surface as function of the fracture surface mineralogy and/or bulk granodiorite mineralogy

Whereas point a) and b) represent extreme cases, the investigations will focus on case c) which is a much more realistic scenario. Although the geochemical experimental conditions planned should favor the stability of the colloids in solution (low ionic strength; pH 9.7; Grimsel ground water chemistry), due to the negative charge of both the bentonite colloids and the mineral surfaces of the granodiorite (references), charge heterogeneities and surface roughness (micro- and nano-roughness) for instance may lead to an attachment of the colloids on the fracture walls (Darbha et al., 2012). All the underlying physical and chemical processes leading to particle deposition and attachment are not straightforward to be incorporated mechanistically into the model, therefore we plan to use a simplified description of the attachment process by assigning experimentally derived attachment probabilities/collision efficiencies α (Grolimund et al., 2001) to the fracture surface. For this, the distribution of the minerals at the granodiorite fracture surface will be incorporated in a simplified way by threshold segmentation of a digital photography of the fracture surface. Figure 9 depicts this approach in an exemplified way. The result of the segmentation can be directly incorporated in the 3D model. These different mineral phases like quartz, feldspar or mafic minerals like e.g. biotite are known to exhibit different attachment affinities for the colloids which can be determined in the laboratory by the colloid probe technique using the atomic force microscopy. Including these information in the 3D model, breakthrough curves for the colloids will be simulated and compared to the experimental results.

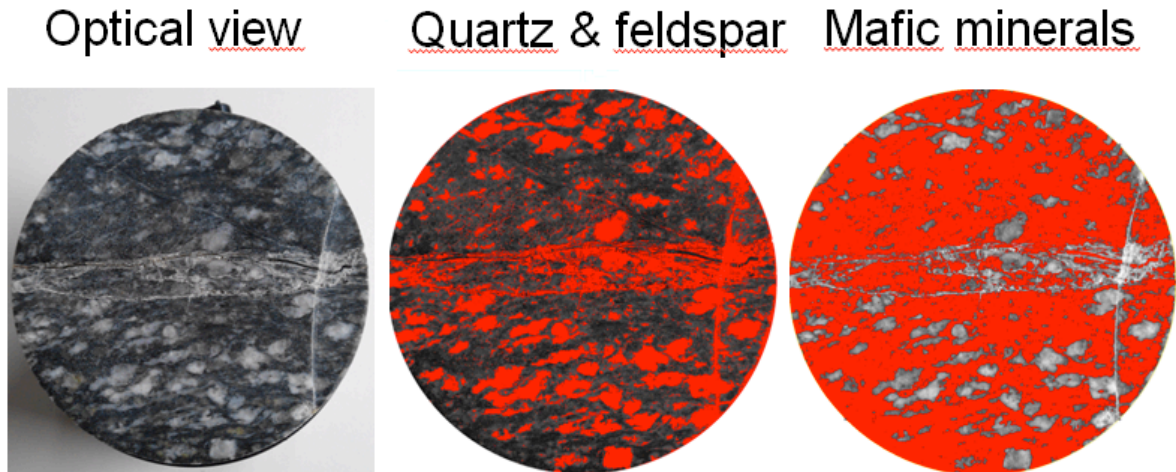


Figure 9: Result of a simple threshold segmentation (based on grey values) of the mineral distribution at a granodiorite surface.

Preliminary flow and particle transport simulations with the prototype fluid cell have been conducted. The fluid field is shown in Figure 10 representing the expected dipole-type flow distribution. The flow rate used was 6×10^{-7} kg/s yielding a mean flow velocity of 1.16×10^{-5} m/s. Note the highest flow velocities in the narrow inlet and outlet tubes and the lower flow velocities in the fracture. The flow velocities in the actual fracture are less. Reynolds numbers are below 0.08 representing laminar flow conditions. Given the mean flow velocity, a particle diffusion coefficient of 2.12×10^{-12} m²/s can be calculated by the Stokes-Einstein equation (Einstein, 1905). Using this diffusion coefficient, a particle Peclet number of ~ 1475 is determined. Using the 3D flow velocity distribution a mean Peclet number of 1302 with a standard deviation of 6300 is obtained. The Peclet number is given by the ratio of a characteristic length (here aperture) times a characteristic velocity (here mean velocity) divided by the diffusion coefficient (here the particle diffusion coefficient). Thus this dimensionless number yields a measure between the advective component and the diffusive component of the (particle) transport. Under the Peclet numbers given, the particle transport is mostly advection dominated.

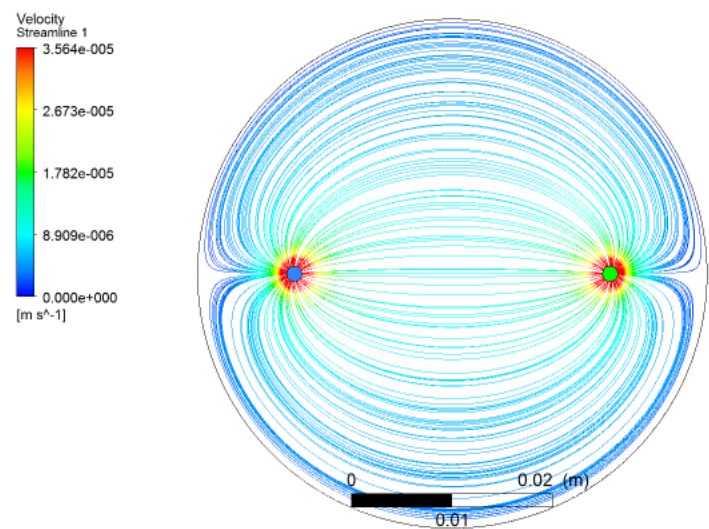


Figure 10: Velocity streamline plot of the flow field in the flow cell.

Figure 11 depicts an example of the Lagrangian particle tracking in the flow cell. Several snapshots visualize the transport of the colloids throughout the flow cell domain for different times. In total 100k particles with a diameter of 10 nm have been injected in this simulation. In the following simulations, the actual measured particle distributions will be used and not only a single sized. The particles are injected in a rather narrow distribution in the fracture by the inlet and progressively spread on their way to the outlet due to the flow field and the Brownian motion. While some particles exhibit a rather short residence time within in the flow cell and reach the outlet therefore quite fast, some particles are following very slow flow paths and are transported to the outer part of the low cell resulting in rather long residence time. This means, that simply due to the flow cell geometry and in consequence the evolving flow field (under the chosen flow rate) the particles exhibit a high dispersion within the flow cell resulting in a rather broad breakthrough curve with a pronounced late time arrival of some particles (tailing). The breakthrough curves are shown in Figure 13.

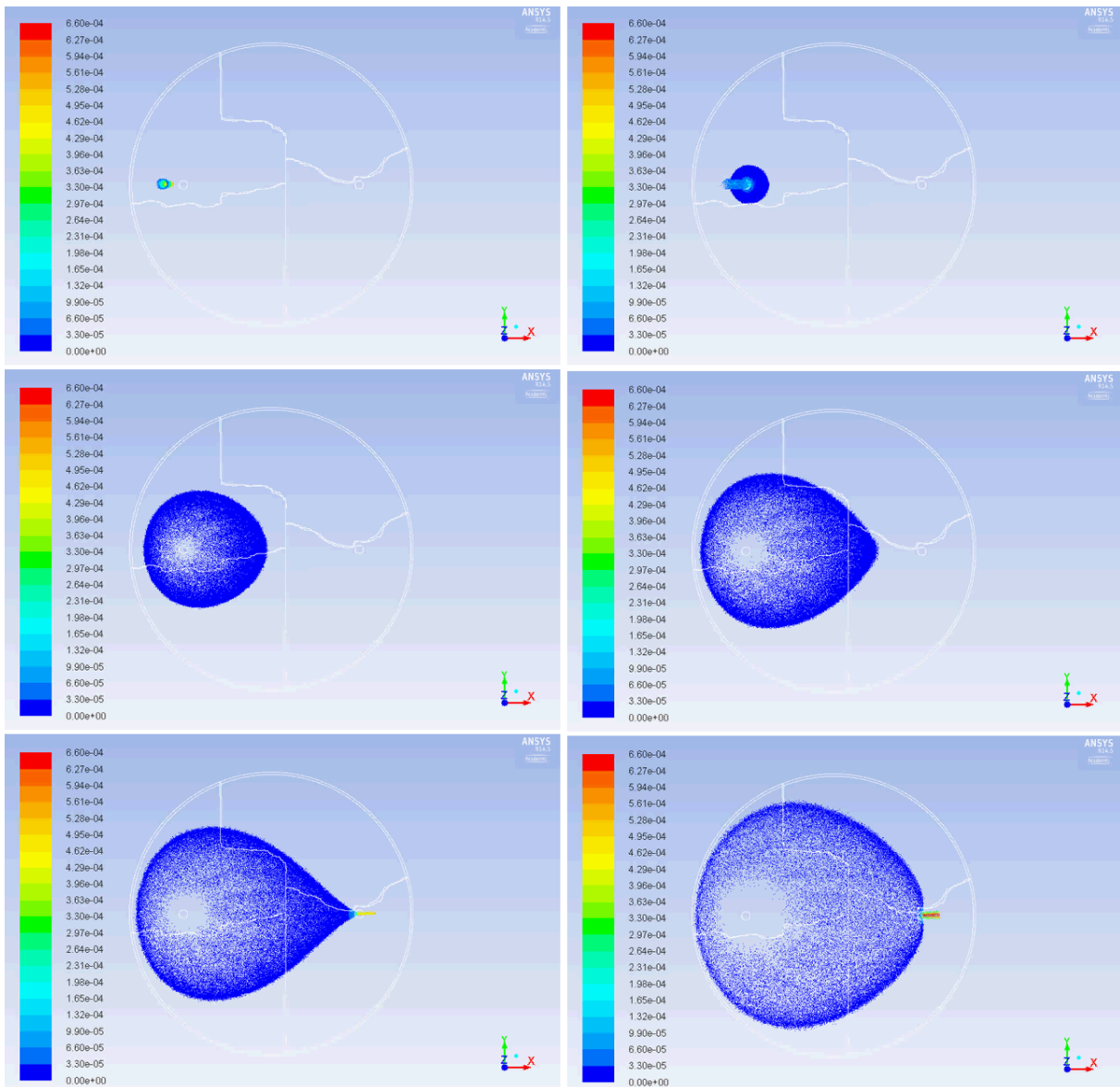


Figure 11: Snapshots of the particle transport in the fracture flow cell for different times.

When assuming a perfect sorption of the particles to the fracture surfaces, particles are trapped and immobilized immediately when touching a surface. In this case, the peak height of the breakthrough curve needs to decrease compared to the case in which no sorption is assumed since the number of particles decrease. This can be seen in Figure 13. A pattern of particles sorbed to the fracture surface is shown in Figure 13. Most of the particles are sorbed (i) to the lower fracture wall reflecting the influence of momentum and gravity on the particle transport and (i) more closely to the inlet. Due to lift forces and Brownian motion particles are also trapped at the upper fracture surface.

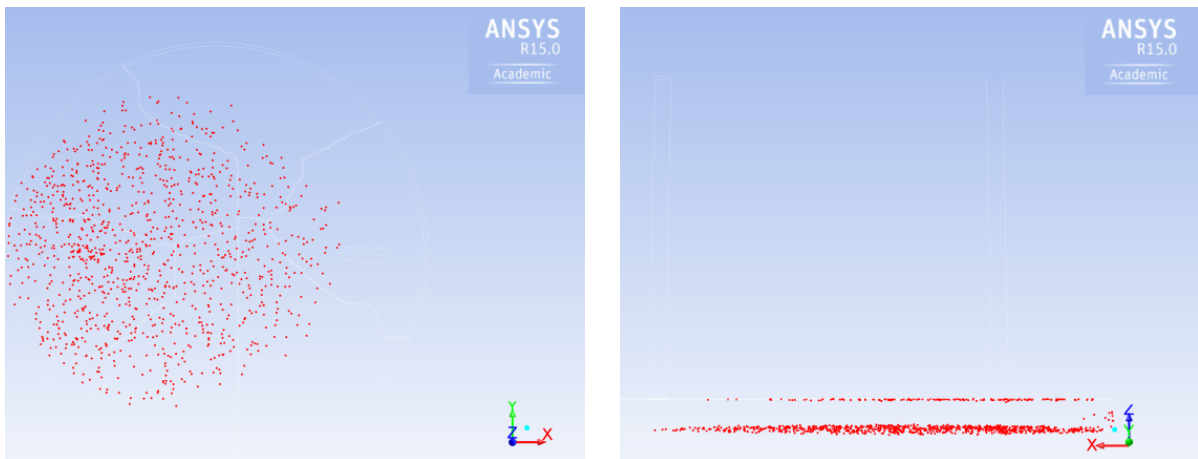


Figure 12: Distribution of deposited particles at the fracture surface (inlet on the left side of the cell; perfect sorption assumed) (Lower) Distribution of deposited particles (alternative view; inlet on the right side of the cell; perfect sorption assumed).

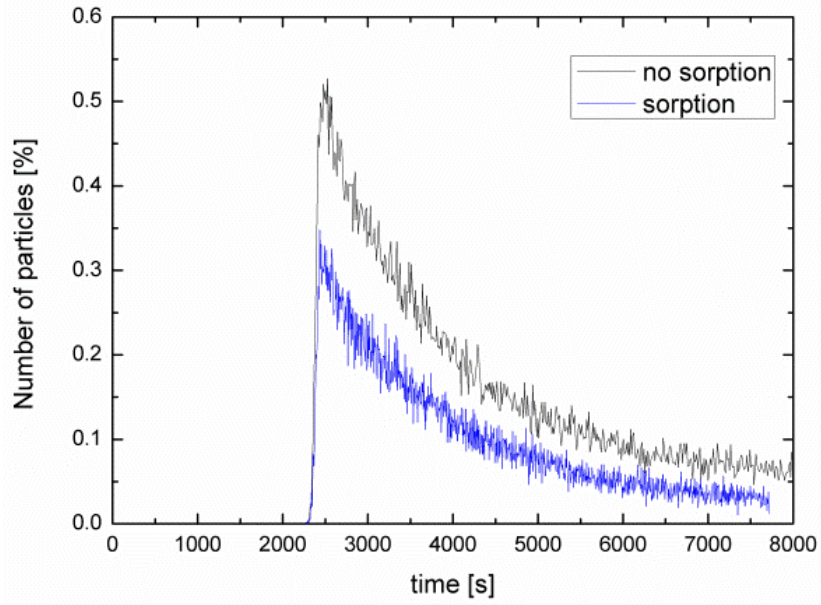


Figure 13: Particle breakthrough curves for both cases considered (no sorption and perfect sorption).

References

- Adler, P.M. and Thovert, J.-F. (1999) Fractures and fracture networks. Kluwer, Dordrecht [u.a.].
- ANSYS (2009) ANSYS FLUENT 12.1.4 User Guide.
- Darbha, G.K., Fischer, C., Luetzenkirchen, J. and Schäfer, T. (2012) Site-Specific Retention of Colloids at Rough Rock Surfaces. *Environmental Science & Technology* 46, 9378-9387.
- Einstein, A. (1905) Über die von der molekularkinetischen Theorie der Wärme geforderte Bewegung von in ruhenden Flüssigkeiten suspendierten Teilchen. *Annalen der Physik* 322, 549-560.
- Grolimund, D., Elimelech, M. and Borkovec, M. (2001) Aggregation and deposition kinetics of mobile colloidal particles in natural porous media. *Colloids and Surfaces A: Physicochemical and Engineering Aspects* 191, 179-188.
- Huber, F., Enzmann, F., Wenka, A., Bouby, M., Dentz, M. and Schäfer, T. (2012) Natural micro-scale heterogeneity induced solute and nanoparticle retardation in fractured crystalline rock. *Journal of Contaminant Hydrology* 133, 40-52.
- Neretnieks, I., Eriksen, T. and Tahtinen, P. (1982) TRACER MOVEMENT IN A SINGLE FISSURE IN GRANITIC ROCK - SOME EXPERIMENTAL RESULTS AND THEIR INTERPRETATION. *Water Resources Research* 18, 849-858.
- SKB (2009) Mechanisms and models for bentonite erosion. Svensk Kärnbränslehantering AB, Stockholm, Sweden.
- SKB (2010) Modelling of erosion of bentonite gel by gel/sol flow. Svensk Kärnbränslehantering AB, Stockholm, Sweden.
- Tsang, Y.W., Tsang, C.F., Neretnieks, I. and Moreno, L. (1988) Flow and Tracer Transport in Fractured Media - a Variable Aperture Channel Model and Its Properties. *Water Resources Research* 24, 2049-2060.

Appendix

Mathematical description of the Discrete Phase Model in ANSYS Fluent (ANSYS, 2009).

By integrating the force balance on the particle in a Lagrangian reference frame, the particle trajectory is obtained describing the particle inertia with the forces acting on the particle. It can be written (in x direction) as:

$$\frac{du_p}{dt} = F_D(\vec{u} - \vec{u}_p) + \frac{\vec{g}(\rho_p - \rho)}{\rho_p} + \vec{F}$$

Where \vec{F} is an additional acceleration term [force/unit particle mass), $F_D(\vec{u} - \vec{u}_p)$ is the drag force per unit particle mass and \vec{g} is the gravity. F_D is further given as :

$$F_D = \frac{18\mu C_D Re}{\rho_p d_p^2 24}$$

With \vec{u} is the velocity of the fluid phase, \vec{u}_p is the velocity of the particle, μ is the fluid molecular viscosity, ρ is the fluid density, ρ_p is the particle density and d_p is the particle diameter. In case of submicron particles, the Stokes law is supposed to be replaced by the Stokes-Cunningham drag law which is written as:

$$F_D = \frac{18\mu}{\rho_p d_p^2 C_c}$$

Re is called the Reynolds number and given as (Eq. XX):

$$Re \equiv \frac{\rho d_p |\vec{u}_p - \vec{u}|}{\mu}$$

One of the additional acceleration forces acting on the particles in our simulation is the Brownian motion/force of the particles which is important for submicron particles as our bentonite colloids. It is formulated as:

$$S_{n,j} = S_0 \delta_j$$

where δ_j is the Kronecker delta function. Furthermore

$$S_0 = \frac{216\nu k_B T}{\pi^2 \rho d_p^5 \left| \frac{\rho_p}{\rho} \right|^2 C_c}$$

where T is the absolute fluid temperature, ν is the kinematic viscosity, C_c is the Cunningham correction (for non-spherical particle shapes) and k_B is the Boltzmann constant.

Another additional force term included in the force balance equation determining the equation of motion of the particles is the Saffman lift force \vec{F} (which is lift of the particles due to shear) which is given as:

$$\vec{F} = \frac{2K\nu^{1/2}\rho d_j}{\rho_p d_p (d_{ik} d_{kl})^{1/4}} (\vec{v} - \vec{v}_p)$$

Where $K = 2.594$ and d_{ik} is the deformation tensor. This lift force is intended for small particle Reynolds numbers and recommended for submicron particles (ANSYS, 2009).

VTT Technical Research Centre of Finland

Authors:

Veli-Matti Pulkkanen

Markus Olin

12 VTT's bentonite erosion model development and testing

At VTT, the bentonite erosion modelling follows two approaches. The so-called baseline model by KTH (Neretnieks et al., 2009) is modified such that it can be solved numerically. The scalability of the model is tested by solving it in different sized geometrical setups with various flow velocities. Acknowledging the limitations of the purely theoretically argued baseline model, another model based on experimental findings is also being developed for the so-called slit erosion experiments carried out in Work Package 2 (WP2).

12.1 Scoping the effect of the water flow velocity and the geometrical setup of the baseline model by KTH on bentonite erosion

VTT's version of Neretnieks' glacial erosion model (Neretnieks et al., 2009) has been applied over a large parameter range. The modelled systems are given in Table 1. It should be remarked that the work is not completed yet, and therefore the uncertainties of the current results might be large.

In all examples the ionic strength of groundwater was set to 0.1 mM, and this salinity was applied over the whole system, meaning that no salt diffusion was included in the modelling. The radius (R) of the source term varied from 0.01 to 2.7 metres, and the groundwater flow velocity (v) from 0.6 to 6 000 m/a. The models were scaled so that the width (W) of the model (direction of groundwater flow) was two times the height (H) of the model, and the origin of the half circle shaped source was set to $W/2.5$ i.e. there was bit more space downstream than upstream. The W value was iterated such that the montmorillonite swelled up to about half of the H , a distance which was assumed to give enough space for the free water to flow such that the flow velocity is not affected too much. In Table 1, the simulation time (t_{end}) is shown and W values are given as multiples of R . Both the W and R are iterated gradually towards most optimal values.

The total montmorillonite flux at the source term and flux density (per length unit of source line) are given in Table 1. The stopping distance (or the maximum swelling distance perpendicular to the water flow) of the expanding montmorillonite (L) is also shown in Table 1, and it is measured as the point where montmorillonite profile starts to descend; this point is actually quite clearly seen. The montmorillonite volume fraction (φ_{stop}) is also given at that stopping point, like the width of stopping zone in the direction of the flow (from φ_{stop} to practically a zero volume fraction).

The total erosion flux graphs at the source edge are drawn in Figure 1. The graph shows that the highest velocity case behaves a bit differently compared to other velocities, and this observation will be studied in the future. However, other fluxes are quite similar meaning that neither system size nor velocity has large effect on the erosion flux.

The example cases need typically one or two days computation time in Dell T3500 Workstation of 24 GB of memory, which allows mesh of about 300 000 elements.

Table 1. The preliminary results from the modified baseline model (BESW).

R (m)	v (m/a)	W	t_{end} (s)	flux ($\mu\text{g/s}$)	flux density ($\mu\text{g/s/m}$)	L (m)	φ_{stop}	width of stop zone (mm)
0.01	6000	30	$1.0 \cdot 10^6$	5.8	184	0.0162	0.0055	0.4
0.02	6000	21	$1.0 \cdot 10^6$	8.1	129	0.0202	0.007	1.0
0.05	6000	13	$1.0 \cdot 10^7$	12.6	80	0.0346	0.007	1.5
0.10	6000	9	$1.0 \cdot 10^8$	20.5	65	0.03		
0.3	6000		$5.0 \cdot 10^8$	34.4	36	0.05		
0.9	6000		$2.0 \cdot 10^8$	55.0	19	0.1		
2.7	6000		$3.0 \cdot 10^6$	98.5	12			
0.01	600		$1.00 \cdot 10^7$	2.1	66	0.130		
0.02	600		$3.16 \cdot 10^7$	2.8	44	0.138		
0.05	600		$5.62 \cdot 10^7$	3.9	25	0.250	0.0050	02.5
0.10	600		$1.00 \cdot 10^8$	5.3	17	0.299	0.0050	1.0
0.30	600		$1.00 \cdot 10^8$	8.9	9	0.419	0.0050	1.5
0.90	600		$1.00 \cdot 10^8$	15.2	5	0.737	0.0053	3.0
2.70	600		$1.00 \cdot 10^8$	28.2	3	0.999	0.0065	4.5
0.01	60							
0.02	60		$1.78 \cdot 10^7$	2.0	33	0.259	0.0062	0.9
0.05	60	60	$1.78 \cdot 10^7$	2.7	17	0.37	0.0055	8.0
0.10	60	30	$5.62 \cdot 10^7$	3.1	10	0.605	0.005	8.0
0.30	60		$1.00 \cdot 10^8$	4.8	5	0.801	0.0055	14
0.90	60	14	$3.16 \cdot 10^8$	7.0	2	1.282	0.0057	31
2.70	60	8	$5.62 \cdot 10^8$	12.1	1	2.025	0.0047	23
0.01	6							
0.02	6	64	$1.00 \cdot 10^7$	2.1	33	0.357	0.0047	4
0.05	6	40	$3.16 \cdot 10^7$	2.4	15	0.642	0.0047	6
0.10	6	30	$5.62 \cdot 10^7$	2.9	9	0.876	0.0042	35
0.30	6	20	$1.00 \cdot 10^8$	4.4	5	1.204	0.0052	140
0.90	6	18	$3.16 \cdot 10^8$	6.1	2	7.5		
2.70	6	20	$1.00 \cdot 10^9$	8.8	1	14.6	0.0052	260
0.01	0.6							
0.02	0.6							
0.05	0.6							
0.10	0.6	40	$1.78 \cdot 10^8$	2.3	7	1.6		

0.30	0.6	28	$3.16 \cdot 10^8$	3.2	3	2.17	0.0047	18
0.90	0.6	14	$1.73 \cdot 10^9$	3.7	1	5		
2.70	0.6	8	$5.62 \cdot 10^8$	10.9	1	3.24	0.005	45

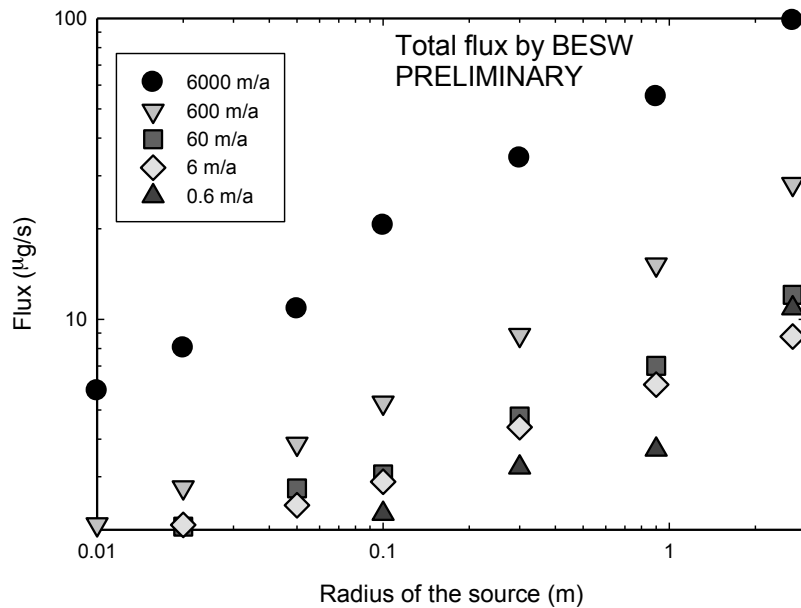


Figure 1. The total erosion flux of montmorillonite as function of radius of the source and groundwater velocity.

12.2 Model development for the slit erosion experiments

The first erosion experiments in a narrow slit (aperture < 1mm) between two parallel, flat plexiglass plates conducted in Work Package 2 (by B+Tech, Claytech and KIT) can be divided modelling-wise roughly to two stages. First, bentonite in a cylinder (cut by the slit) wets and simultaneously swells into the slit. Secondly, the swollen solid bentonite (or bentonite gel) loses its structural integrity due to the dilute water (or simply due to the low cohesion of the recently wet, swollen bentonite) and is carried away by the flowing water.

The model development has been begun with the wetting-swelling problem. A consistent coupling of the mechanics, the wetting hydraulics and the water chemistry of bentonite is the key for building a model that can be used to describe the behaviour of bentonite from the wetting-swelling stage to erosion by dilute water. In KTH's baseline model, the mechanical behaviour of bentonite while swelling has been described as 'diffusive' process which does not have any mechanical component to stop swelling (e.g. the friction of the fracture walls) and thus would make the bentonite swell even without contact to dilute water. Therefore, if the initial state for erosion was predicted by the model, it would be inconsistent with the currently used initial states of the erosion simulations. A common modelling approach to the wetting-swelling problem is to apply the existing hydro-mechanical clay models such as the Barcelona basic model (BBM, or the extended version of it including large deformations) for bentonite. The complicated and physically not so evident couplings of this type of models make the inclusion of the chemical effect on the mechanical behaviour somewhat difficult. Aiming to model the erosion (and also swelling) of bentonite by dilute water makes this a serious downside. It also seems that there is no evidence in literature that bentonite would behave (or, on the other hand, would not behave) according to these models. As a consequence of the limitation of the current models, a step back has had to be taken in the model development.

Although it is commonly accepted that the most of the water in compacted bentonite is attached to nanometre scale surfaces, the water activity (or water chemical potential), the difference of which drives the most of the water flow in bentonite, are often converted from the units of energy per mole to values of pressure, or suction (energy per volume). The suction values are then used in van Genuchten type of wetting models and in BBM type of mechanical models, even though the suction is now not a measure of capillary action but some molecular level behaviour. In the model development here, it is proposed that the activity of the water (obtained experimentally from sorption isotherms assuming equilibrium between sorbed water and the water vapour) is used directly. The resulting equation for water movement is a diffusion equation (somewhat similar to e.g. the one in Kröhn (2010) but with a different physical interpretation). Due to the swelling structure of montmorillonite on nanometre-level, the same activity of water (energy/moles) can be thought to provide also the swelling stress of bentonite (energy/total volume = energy/moles times moles/total volume). Besides this hydro-mechanical coupling, the chemical composition of the water in bentonite can be coupled to the hydraulics and mechanics by similar means. Restricting currently on the somewhat solid bentonite, the approach for the coupling seems promising but the work on the final form of the coupling and the gathering of experimental evidence to support it is still on-going. If the coupling turns out feasible, it should be extendable also to loose bentonite by extending only the mechanical model (from an elasto-plastic model to a suitable loose bentonite model).

A restriction on developing a coupled model is the available data. Although a number of experiments for example on swelling pressure or on water sorption have been carried out, often one (or more) parameter (e.g. the relative humidity, the concentration of a chemical species, or the mechanical parameters) is not measured and, therefore, confirming the exact form of the coupling becomes difficult. Also, there exists some data on mechanical parameters for bentonite (e.g. Eloranta (2012) and Pintado et. al (2013)), but systematic experimental work on the parameters in different densities, saturations, and chemical environments seems to be missing. Without such data, the uncertainties in the model parameters and the model itself (e.g. the elasto-plastic model) remain high. Testing the diffusion approach for the water movement and the mechanical model suggested in Eloranta (2012) has been carried out in a couple of experimental setups (e.g. the experiments by University of Jyväskylä in WP2) utilizing the modelling tools developed earlier in Finnish Research Programme on Nuclear Waste Management (KYT).

The development of the model for the structural breakdown and the final erosion of bentonite in dilute water is pending on experiments. Evidence of the breakdown mechanism provided by experiments in WP2 (the microstructural changes when bentonite swells to an eroding mass) and WP3 (the sizes of the eroding particles) is needed for the basis of the model.

Eloranta, A., 2012. Experimental Methods for Measuring Elasto-plastic Parameters of Bentonite Clay. M.Sc. Thesis. University of Jyväskylä.

Kröhn, K.-P., 2010. Simulating non-isothermal water uptake of compacted bentonite without coupling of hydraulics to mechanics. *Applied Clay Science*, 47, pp 28–35

Neretnieks, I., Liu, L., Moreno, L., 2009. Mechanisms and Models for Bentonite Erosion. Swedish Nuclear

Fuel and Waste management Co., Swedish Nuclear Fuel and Waste management Co., SKB TR-09-35

Pintado, X., Mamanul, H. Md., Martikainen, J., 2013. Thermo-Hydro-Mechanical Tests of Buffer Material. Posiva Oy, POSIVA 2012-49